Fundamental Interactions in Gasoline Compression Ignition Engines with Fuel Stratification

by

Benjamin Matthew Wolk

A dissertation submitted in partial satisfaction of the

requirements for the degree of

Doctor of Philosophy

in

Engineering – Mechanical Engineering

in the

Graduate Division

of the

University of California, Berkeley

Committee in charge:

Professor Jyh-Yuan Chen, Chair
Professor Robert Dibble
Professor Stuart Bale

Fall 2014

Fundamental Interactions in Gasoline Compression Ignition Engines with Fuel Stratification

Abstract

Fundamental Interactions in Gasoline Compression Ignition Engines with Fuel Stratification

by

Benjamin Matthew Wolk

Doctor of Philosophy in Engineering – Mechanical Engineering

University of California, Berkeley

Professor Jyh-Yuan Chen, Chair

Transportation accounted for 28% of the total U.S. energy demand in 2011, with 93% of U.S. transportation energy coming from petroleum. The large impact of the transportation sector on global climate change necessitates more-efficient, cleaner-burning internal combustion engine operating strategies. One such strategy that has received substantial research attention in the last decade is Homogeneous Charge Compression Ignition (HCCI). Although the efficiency and emissions benefits of HCCI are well established, practical limits on the operating range of HCCI engines have inhibited their application in consumer vehicles. One such limit is at high load, where the pressure rise rate in the combustion chamber becomes excessively large.

Fuel stratification is a potential strategy for reducing the maximum pressure rise rate in HCCI engines. The aim is to introduce reactivity gradients through fuel stratification to promote sequential auto-ignition rather than a bulk-ignition, as in the homogeneous case. A gasoline-fueled compression ignition engine with fuel stratification is termed a Gasoline Compression Ignition (GCI) engine. Although a reasonable amount of experimental research has been performed for fuel stratification in GCI engines, a clear understanding of how the fundamental in-cylinder processes of fuel spray evaporation, mixing, and heat release contribute to the observed phenomena is lacking. Of particular interest is gasoline's pressure sensitive low-temperature chemistry and how it impacts the sequential auto-ignition of the stratified charge.

In order to computationally study GCI with fuel stratification using three-dimensional computational fluid dynamics (CFD) and chemical kinetics, two reduced mechanisms have been developed. The reduced mechanisms were developed from a large, detailed mechanism with about 1400 species for a 4-component gasoline surrogate. The two versions of the reduced mechanism developed in this work are: (1) a 96-species version and (2) a 98-species version including nitric oxide formation reactions. Development of reduced mechanisms is necessary because the detailed mechanism is computationally prohibitive in three-dimensional CFD and chemical kinetics simulations.

Simulations of Partial Fuel Stratification (PFS), a GCI strategy, have been performed using CONVERGE with the 96-species reduced mechanism developed in this work for a 4-component gasoline surrogate. Comparison is made to experimental data from the Sandia HCCI/GCI engine at a compression ratio 14:1 at intake pressures of 1 bar and 2 bar. Analysis of the heat release and temperature in the different equivalence ratio (ϕ) regions reveals that sequential auto-ignition of the stratified charge occurs in order of increasing ϕ for 1 bar intake pressure and in order of decreasing ϕ for 2 bar intake pressure. Increased low- and intermediate-temperature heat release with increasing ϕ at 2 bar intake pressure compensates for decreased temperatures in higher-ϕ regions due to evaporative cooling from the liquid fuel spray and decreased compression heating from lower values of the ratio of specific heats. The presence of low- and intermediate-temperature heat release at 2 bar intake pressure alters the temperature distribution of the mixture stratification before hot-ignition, promoting the desired sequential auto-ignition. At 1 bar intake pressure, the sequential auto-ignition occurs in the reverse order compared to 2 bar intake pressure and too fast for useful reduction of the maximum pressure rise rate compared to HCCI. Additionally, the premixed portion of the charge auto-ignites before the highest-ϕ regions. Conversely, at 2 bar intake pressure, the premixed portion of the charge auto-ignites last, after the higher-ϕ regions. More importantly, the sequential auto-ignition occurs over a longer time period for 2 bar intake pressure than at 1 bar intake pressure such that a sizable reduction in the maximum pressure rise rate compared to HCCI can be achieved.

To my family and friends

Thank you for your love and support.

Contents

List of Figures

List of Tables

Acknowledgments

I would like to acknowledge my advisors, lab mates, family, and friends who supported me throughout this journey and who have helped me grow as an individual and a professional.

I would like to thank my advisor, Professor J.Y. Chen, who was always available to provide guidance and troubleshoot any problem. He taught me an exceptional amount about combustion, chemical mechanisms, and simulation codes. I would also like to thank Professor Robert Dibble, who taught me about combustion and academia, as well as many other life lessons. I would also like to acknowledge John Dec of Sandia National Laboratories for his collaboration on this work and many insightful discussions.

I would also like to thank my lab mates, current and former, for their insight, collaboration, and willingness to help troubleshoot problems. I would specifically like to thank Anthony DeFilippo for his friendship and for mentoring me through my first years as a graduate student. I would also like to thank Greg Chin for his guidance in setting up the computational grid used in this work.

To my soon-to-be wife, P.J., thank you for your continued love and support each day and throughout my academic career. You are always there to inspire and ground me. To my parents, Brad and Laura, you inspire me to do the best that I can in all my endeavors and I appreciate your unconditional love and support. To my grandparents - Ron, Eileen, Janice, and Ed - thank you for your wisdom, guidance, and love. To my brother, Zack, thank you for always supporting me. To Duke, you're a constant (large, loud, and drooling) reminder to enjoy every day.

I would also like to acknowledge the various sources of funding I was fortunate to have during my time in graduate school, including the John and Janet McMurty Fellowship and Anselmo Macchi Fellowship. The Department of Energy, King Abdullah University of Science and Technology, and Department of Mechanical Engineering are also acknowledged for their generous funding support.

Chapter 1

Introduction

1.1 Structure of this dissertation

This dissertation explores the fundamental physical processes governing gasoline compression ignition (GCI) engine operation using a commercial computational fluid dynamics (CFD) and chemical kinetics code and a novel reduced chemical kinetic mechanism.

In this chapter, an overview of the dissertation, motivation, and background on the status of current research is presented. In Chapter 2, heat release from hydrocarbon fuels is discussed, including the various phases of heat release and the molecular and/or chemical processes contributing to this heat release. In Chapter 3, the fundamentals of chemical kinetics are reviewed. Additionally, the drawbacks of large, detailed chemical kinetic mechanisms are illustrated. The development of smaller, skeletal and reduced mechanisms is also discussed, including software and flame codes used in this work. In Chapter 4, two reduced mechanisms are developed and validated. The mechanisms are optimized for use in computer models of GCI engines for a four-component gasoline fuel surrogate. In Chapter 5, the CFD code used in this work is discussed, including the main governing equations. The specific model constructed for this work of the Sandia HCCI/GCI engine is highlighted. In Chapters 6 and 7, simulation results are presented and compared to experiments. Detailed analyses of simulation results are performed to gain insight into the interactions of the fundamental in-cylinder processes. In Chapter 8, concluding remarks are made about the developments in and findings of the current work. In the Appendix, supplemental details about the reduced mechanism and instructions on implementing the reduced mechanism into the CFD code are presented.

1.2 Dissertation contributions

This dissertation aims to advance the understanding of GCI through numerical modeling based on previously conducted experiments. The results of the numerical model are analyzed

in detail to elucidate the interactions of the fundamental physical processes. Contributions to the overall body of science include:

- Development of two reduced chemical kinetic mechanisms for a four-component gasoline surrogate, optimized for three-dimensional CFD of GCI engines
- Explanation of the fundamental difference in behavior of GCI at different intake pressures based on the interaction of in-cylinder processes

1.3 Motivation

Climate change is a serious issue currently facing the global community (Chapman, 2007; Gaffney and Marley, 2009; Garrett, 1992; Gurney *et al.*, 2009; Houghton, 2005; IEA, 2013a; Quadrelli and Peterson, 2007) with CO_2 emissions rising exponentially since 1870 (IEA, 2013a). Fossil fuel combustion from two main sectors accounted for nearly two-thirds of global anthropogenic greenhouse gas (GHG) emissions in 2011: the electricity and heat generation sector (42%) and the transport sector (22%) (IEA, 2013a). Emissions growth in the transport sector is driven by emissions from the road sector, which have increased by 52% since 1990 and accounted for about three quarters of transport emissions in 2011 (IEA, 2013a). Global demand for transport is unlikely to decrease in the near future; the World Energy Outlook (WEO) predicts that transport fuel demand will grow by nearly 40% by 2035 (IEA, 2013b).

Improving the energy efficiency and reducing the carbon intensity (e.g. burning natural gas instead of coal) of both the electricity/heat generation and transport sectors could significantly diminish their contribution to global climate change (Quadrelli and Peterson, 2007). In order to limit carbon dioxide emissions from internal combustion (IC) engines by improving their energy efficiency, policy makers in the United States have legislated a fleetwide-average 163 grams of CO_2 per mile by model year 2025, which is equivalent to 54.5 miles per gallon (EPA and NHTSA, 2012). To reach these fuel economy targets, next-generation low-temperature compression ignition (CI) combustion modes that reduce exhaust emissions and improve thermal efficiency are currently being explored.

1.4 Engine operating strategies

The majority of modern automotive engines use a four-stroke cycle: (1) intake of fresh gases, (2) compression of fresh gases, (3) expansion of burned gases, (4) exhaust of burned gases. Combustion takes place when the piston is near the end of compression, or top dead center (TDC), between (2) and (3). Most production automotive engines can be classified into either gasoline spark ignition (SI) engines or diesel CI engines. Next-generation engine operating strategies that do not conform to the traditional SI or diesel engine molds are currently under development to meet the fuel economy targets of the near future. The basics of SI

and diesel engines are reviewed below followed by a discussion of the next-generation engine operating strategy that is the focus of the present work.

Spark-ignition

Spark ignited engines are generally characterized by a well-mixed fuel-air charge (created by port fuel injection) at the stoichiometric fuel-air ratio. Combustion is initiated using a spark, which initiates a flame kernel that propagates through the mixture consuming fuel and releasing heat. Stoichiometric fuel-air ratios permit improved engine operating stability and reduced cycle-to-cycle variations as the flame is more easily initiated and the flame propagates more quickly compared to more dilute fuel-air mixtures.

The thermal efficiency of an SI engine is strongly dependent on the compression ratio (CR) of the engine, the ratio of the maximum in-cylinder volume before compression to the minimum in-cylinder volume after compression. A premixed SI engine is ideally an Otto cycle, with thermal efficiency $\eta_{th} = 1 - \left(1/\mathrm{CR}^{\gamma-1}\right)$, where $\gamma = c_p/c_v$ is the ratio of specific heats. Real SI engines depart from the ideal Otto cycle in several ways, including that the heat released from combustion does not occur at constant volume. Increasing the CR of an SI engine is desirable, but these engines are limited by a phenomena known as engine knock. Engine knock is characterized by auto-ignition of the unburned gases ahead of the flame front as a result of the compression heating from the expanding burned gas. Engine knock leads to a rapid pressure rise and pressure waves that can damage the engine. Increased octane number fuels are more resistant to engine knock and are used in high-CR engines.

Because the fuel-air ratio is fixed at stoichiometric, the power output of SI engines is controlled by the amount of intake air provided to the cylinder. The intake air mass can be decreased by throttling the air flow into the cylinder, at the expense of increased pumping work, or increased by increasing the intake pressure using a turbocharger or supercharger.

Emissions from SI engines include oxides of nitrogen (NO_x), carbon monoxide (CO), and unburnt hydrocarbons (UHC). SI engines emit high levels of NO_x due to the high flame temperatures from stoichiometric combustion (NO_x is formed through the thermal route when the temperature exceeds about 1800 K). CO and UHC are emitted in SI engines because unburnt fuel-air mixture is trapped in the cold crevice regions (e.g. between the piston and piston rings) during the compression stoke and released during the exhaust stroke, when the temperature is too cold for complete oxidation to occur. Fortunately, SI engines have low emission of particulate matter (PM).

In SI engines, after-treatment of the exhaust is needed to reduce the oxides of nitrogen (NO_x), carbon monoxide (CO), and unburnt hydrocarbons (UHC). Exhaust after treatment is normally accomplished using a three-way catalyst that: (1) reduces NO_x to nitrogen and oxygen, (2) oxidizes CO to CO_2 and H_2O, and (3) oxidizes unburnt hydrocarbons to CO_2 and H_2O. The three-way catalyst works best for fuel-air ratios near stoichiometric, with the oxidation of UHC and CO favored when there is excess O_2 and the reduction of NO_x favored when there is negligible O_2.

An emerging strategy to improve SI engine efficiency is to use direct-injection (DI) of the fuel as opposed to port fuel injection. In DI SI engines, air is inhaled into the cylinder and the fuel is sprayed directly into the cylinder during the intake or compression strokes (early enough for evaporation and mixing to occur before the time of spark). By using DI, the fuel can be kept away from the crevices (reducing the emission of CO and UHC) and cylinder walls (reducing heat losses). Additionally, the cooling effect of evaporation decreases the in-cylinder temperature such that a higher CR can be used without experiencing engine knock (Zhao *et al.*, 1999).

Conventional diesel

In conventional diesel engines, air is inhaled during the compression stroke and fuel is injected near TDC. The fuel spray atomizes, evaporates, mixes, and auto-ignites rapidly. The heat release is dominated by the speed of evaporation and mixing rather than that of flame propagation as in SI engines. The amount of fuel injected controls power output in diesel engines as opposed to the amount of air in SI engines. Because of the direct injection of fuel and the rapid combustion of fuel upon mixing with air, diesel engines are operated un-throttled and at much higher CR than SI engines. Un-throttled operation, higher CR, and globally fuel-lean mixtures lead to improved efficiency of diesel engines relative to SI engines. The thermal efficiency of the ideal Diesel cycle is given in Eq. 1.1, where r_c is called the cutoff ratio and defined as the ratio of the in-cylinder volumes before and after the combustion process. It is worth noting that the Otto cycle (SI) has a higher efficiency than the diesel cycle at the same CR ($r_c = 1$ for Otto, $r_c > 1$ for Diesel), but SI engines are limited in CR by engine knock.

$$\eta_{th} = 1 - \frac{1}{\mathrm{CR}^{\gamma-1}} \left(\frac{r_c^{\gamma} - 1}{\gamma(r_c - 1)} \right) \tag{1.1}$$

Diesel engines are generally operated with excess air (globally) compared to stoichiometric, so UHC and CO emissions are lower compared to SI engines. Additionally, only air is present during the intake and early compression strokes, so only air (and not fuel) enters the crevices. However, high flame temperatures occur due to combustion occurring at the stoichiometric contour in the evaporating fuel spray, leading to high NO_x emissions. At high loads, PM and soot are also emitted. Due to the global excess air, the three-way catalyst cannot be used for exhaust after treatment. Selective catalytic reduction (SCR) can be used to reduce NO_x through reaction with ammonia or urea to produce nitrogen and water, although this has the added complication of carrying SCR fluid (also called Diesel Exhaust Fluid or DEF) on the vehicle. PM and soot are trapped using a particulate filter, which has to be periodically re-charged by oxidizing the accumulated soot by introducing excess fuel in the exhaust. UHC and CO can be oxidized in the exhaust using an oxidation catalyst.

While conventional diesel engines offer desirable high efficiencies, refineries can only shift their gasoline-diesel balance slightly. For this reason, gasoline-fueled engines will remain

important in global transportation markets and research is currently being conducted to develop next-generation gasoline-fueled engine operating strategies.

Advanced low-temperature combustion (LTC)

Next-generation engine operating strategies aim to increase efficiency in gasoline-fueled engines by moving away from traditional SI towards higher-CR, premixed or partially-premixed, compression-ignition (CI) operation. These engines will operate dilute, keeping peak temperatures low (ideally below 1800 K) to mitigate NO_x formation. If the dilution is accomplished with excess air, such that there is excess O_2 in the exhaust, three-way catalysts cannot be used. As such, the aim is to achieve engine-out NO_x and PM emissions that are below the regulated limits such that no exhaust after treatment is required (except for possibly an oxidation catalyst). Lower peak temperatures also reduce heat losses to the piston and cylinder walls, increasing efficiency.

The advanced low-temperature combustion (LTC) engine operating modes receiving substantial research attention include Homogeneous Charge Compression Ignition (HCCI), Spark-Assisted Compression Ignition (SACI), Stratified Charge Compression Ignition (SCCI), and Reactivity Controlled Compression Ignition (RCCI). Both HCCI and SACI use homogeneous fuel-air mixtures and rely on fuel auto-ignition characteristics for combustion phasing, although SACI has the advantage of spark ignition to influence the start of combustion (SOC). In SACI, both flame propagation and subsequent auto-ignition are responsible for consumption of the fuel (SACI can be naively thought of as controlled engine knock).

For both HCCI and SACI at high loads, extremely rapid combustion can occur leading to knock (pressure oscillations) and, ultimately, engine damage. HCCI and SACI must use lean fuel-air mixtures or high levels of exhaust gas recirculation (EGR) to lower the heat release rate (HRR) such that the maximum pressure rise rate (PRR_{max}) is acceptable (e.g. $PRR_{max} < 7$ bar/crank angle degree) (Lu *et al.*, 2011). Although homogeneous fuel mixtures are targeted in HCCI combustion, thermal stratification has been shown to play an important role in dictating HRR and PRR_{max} (Dec and Hwang, 2009; Dec *et al.*, 2006; Dec, 2009). In-cylinder zones with the same mixture composition and different temperatures will auto-ignite at different times, which can have the net effect of smoothing out the heat release profile. Fuel stratification, as in SCCI, has also been shown to influence HRR and PRR_{max} (Dahl and Denbratt, 2011; Dec *et al.*, 2011; Ma *et al.*, 2008; Yang *et al.*, 2011, 2012).

Partial Fuel Stratification (PFS) is a SCCI strategy that aims to reduce PRR_{max} by using fuel stratification to prolong combustion (Dahl and Denbratt, 2011; Dec *et al.*, 2011; Ma *et al.*, 2008; Yang *et al.*, 2011, 2012) and enable engine operation at high load conditions. PFS is accomplished by mixing the majority of the fuel with intake air and direct-injecting (DI) the rest (up to about 20% of the fuel mass) during the compression stroke. The goal of preparing a stratified mixture is to promote sequential auto-ignition that reduces PRR_{max}. RCCI is similar to SCCI in that gradients in reactivity are introduced to promote sequential auto-ignition, however, RCCI uses two or more fuels of varying reactivity introduced in separate injection events (Kokjohn *et al.*, 2011). The fuel auto-ignition chemistry is critical

in SCCI and the behavior of PFS depends on how the auto-ignition characteristics of the fuel (or fuel-blend) change with equivalence ratio (ϕ) and if the fuel exhibits single- or multi-stage ignition (Yang *et al.*, 2011). PFS or SCCI for gasoline-fueled engines will also be referred to as gasoline compression ignition (GCI).

Background on GCI/PFS

The ϕ-sensitivity of a fuel describes how its auto-ignition characteristics change with ϕ (the equivalence ratio or normalized fuel-air ratio, defined in Eq. 3.2) and is an indicator of how a fuel will respond to stratification (Dec *et al.*, 2011; Yang *et al.*, 2011, 2012). A fuel is considered ϕ-sensitive if increasing ϕ advances the HCCI combustion phasing. For gasoline at ambient intake pressure, increasing ϕ delays the hot-ignition (thermal-runaway) timing because the reduced ratio of specific heats ($\gamma = c_p/c_v$) decreases the compressed-gas temperature. Thus, gasoline is not ϕ-sensitive at ambient intake pressure. Conversely, PRF73 (a mixture of 73% iso-octane and 27% n-heptane by liquid volume) is ϕ-sensitive at ambient intake pressure; increasing ϕ advances the hot-ignition timing because the heat released from pre-ignition reactions increases with ϕ and compensates for the reduced γ. Interestingly, gasoline becomes ϕ-sensitive at sufficiently boosted intake pressure because the pre-ignition reactions become more active at increased pressure and are more prominent for larger ϕ. PFS is expected to result in sequential ignition for ϕ-sensitive fuels for which the heat released from pre-ignition reactions increases with ϕ.

PFS has been shown to reduce PRR_{max} for ϕ-sensitive fuels, including PRF73, gasoline at boosted intake pressures, and a low-octane gasoline-like petroleum distillate (Dahl and Denbratt, 2011; Dec *et al.*, 2011; Ma *et al.*, 2008; Yang *et al.*, 2011, 2012). A span of the fraction of the total fuel mass direct-injected at a constant injection timing was performed with gasoline at intake pressures of 1 bar and 2 bar in Dec *et al.* (2011). It was shown that gasoline did not respond to the stratification (no reduction in PRR_{max}) at 1 bar intake pressure at any of the DI fractions investigated. However, at 2 bar intake pressure, gasoline responded to the stratification with increased reduction in PRR_{max} with increasing DI fraction. These observations are consistent with the notion of ϕ-sensitivity described above. A span of direct-injection timing at a constant DI fraction was also performed in Dec *et al.* (2011) for gasoline at an intake pressure of 2 bar, showing that delayed DI timing (increased stratification) reduces PRR_{max}. The combustion phasing is important in dictating PRR_{max}, so it was held constant in Dec *et al.* (2011) by varying the EGR level while keeping the intake temperature constant. Although experimental observations indicate that a fuel with increased pre-ignition heat release with increasing ϕ (a ϕ-sensitive fuel) will respond favorably to stratification, how the pre-ignition heat release interacts with the other in-cylinder processes is not yet fully understood.

In addition to experimental investigations, computer simulations have been performed for stratified-charge engine operation (Abraham, 2011; Zheng *et al.*, 2010). In Abraham (2011), the effects of swirl, injection pressure, injector hole-size, number of injector holes, injection timing, and piston geometry on mixture stratification of non-reacting iso-octane/air mixtures

were investigated. Injection timing was found to be the most important factor influencing mixture stratification with the other factors having secondary, although distinct, effects. In Zheng *et al.* (2010), fully coupled multi-dimensional computational fluid dynamics (CFD) and chemical kinetics simulations of n-heptane/air mixture stratification and combustion were conducted using a 42-species reduced mechanism (Zheng and Yao, 2009) for a naturally aspirated engine. Evaporative cooling from the fuel injection decreased the temperature of the richer regions, such that only the lean premixed charge unaffected by the spray released heat at low temperatures ($\sim$ 780 K). After the low temperature reactions, the in-cylinder temperature was almost uniform and hot ignition occurred first in the richer regions. Changes in the emission of CO, NO_x, and UHC with stratification are also discussed in Zheng *et al.* (2010). Additional computational research is required to more fully understand the observations in Dec *et al.* (2011).

In a review of CI engines, Dec (2009) notes that CI engine modeling requires improved chemical-kinetic models that more accurately predict low temperature heat release (LTHR), pressure-boost effects, and the behavior of realistic fuels. Accurate prediction of LTHR is important because LTHR influences the chemistry leading up to hot ignition (Hwang *et al.*, 2008). Additionally, the higher temperature rise rate prior to hot ignition resulting from LTHR reduces the influence of random fluctuations in the charge temperature on the hot ignition timing (Sjöberg and Dec, 2007a). However, Sjöberg and Dec (2007b) note that LTHR propensity decreases with RPM as the actual time spent in the appropriate temperature range is reduced at higher engine speeds. Accurately predicting the effects of pressure-boost is important because the LTHR characteristics of a fuel can change with pressure (e.g. gasoline).

This dissertation develops a chemical kinetic mechanism for gasoline and a 3D CFD model of the engine used in Dec *et al.* (2011). The chemical kinetic mechanism and 3D CFD model are used to simulate selected cases from the DI fraction and DI timing spans to more fully understand how pre-ignition heat release interacts with the stratified mixture leading to reductions in PRR_{max} at 2 bar intake pressure, but not at 1 bar intake pressure.

Chapter 2

Heat release from hydrocarbon fuels

In gasoline compression ignition (GCI) engines, the fuel chemistry plays the dominant role in dictating combustion characteristics. This is different from both spark-ignition (SI) and conventional diesel combustion engines where flame propagation and mixing/vaporization are dominant, respectively. Mixing and vaporization are also important in GCI, having a direct influence on the mixture preparation and only an indirect influence on ignition (through the mixture preparation). The influence on ignition is indirect because the fuel evaporates and mixes well before ignition, whereas in conventional diesel combustion, the fuel burns rapidly upon mixing with sufficient oxidizer.

The heat release from hydrocarbon fuels can be broadly characterized by the temperature range during which the heat release occurs. These ranges and the approximate temperatures at which they occur are: (1) low-temperature heat release (LTHR) for $T < 850$ K, (2) intermediate-temperature heat release (ITHR) for 850 K $< T <$ 1000 K (3) hydrogen peroxide decomposition for $T > 1000$ K , and (4) hot-ignition for $T > 1200$ K. Although hydrocarbon fuels vary in their extent of reaction and/or heat release within these temperature ranges, the types of reactions that occur within a given temperature range are fairly similar between hydrocarbon fuels (Westbrook, 2000).

Hydrocarbon fuels can also be broadly characterized into single-stage or dual-stage ignition fuels. For single-stage ignition fuels, such as iso-octane and ethanol, the combustion heat release is observed in a single main event. For dual stage ignition fuels, such as n-heptane and dimethyl ether (DME), the main combustion event is preceded by a smaller (albeit substantial) heat release event. A heat release profile from Sjöberg and Dec (2007a) for iso-octane and PRF80 (a mixture of 80% iso-octane and 20% n-heptane by liquid volume) is shown in Fig. 2.1. It can be seen in Fig. 2.1 that only a single peak is evident near 372 CAD for iso-octane (top dead center is 360 CAD) while a small peak is observed well before the main peak for PRF80 (small peak near 345 CAD and main peak near 372 CAD). The early heat release for PRF80 is caused by partial oxidation of the fuel that increases the in-cylinder temperature before hot-ignition. As a result, a lower intake temperature is required for PRF80 to ignite at the same crank angle as iso-octane.

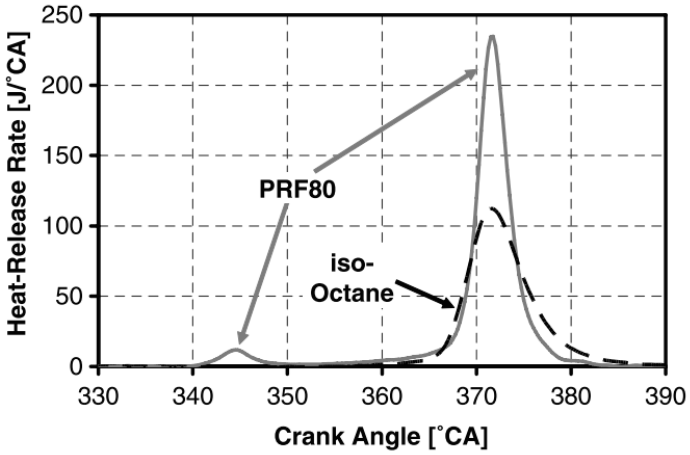

Figure 2.1: Heat release profiles of iso-octane and PRF80 from Sjöberg and Dec (2007a) showing single-stage and dual-stage ignition respectively.

2.1 Low-temperature heat release (LTHR)

The oxidation pathways of a hydrocarbon fuel are illustrated in Fig. 2.2. The first step in hydrocarbon oxidation is hydrogen abstraction from the fuel (RH), resulting in an alkyl radical ($\dot{R}$). Hydrogen abstraction begins to occur when the temperature exceeds about 550 K (Westbrook, 2000). At high temperatures, the fuel radical $\dot{R}$ decomposes through β-scission into an olefin (contains at least one carbon-carbon double bond) and smaller alkyl radical ($\dot{R}'$).

At lower temperatures, however, O_2 attaches to the alkyl radical, resulting in an alkylperoxy radical ($RO_2\cdot$). The addition of O_2 occurs through the reaction $\dot{R}+O_2+M \leftrightarrow RO_2\cdot+M$, where M is a third body. The third-body M can be any species, although species may have different collision efficiencies. The formation of $RO_2\cdot$ plays a key role in LTHR. This reaction favors $RO_2\cdot$ at lower temperatures (determined by the equilibrium constant) and at higher pressures. The forward reaction is favored at higher pressures because the forward rate of the three-body reaction scales as P^3 while the reverse two-body reaction scales as P^2.

Next, the $RO_2\cdot$ radicals isomerize to produce $QOOH$ radicals, which can undergo chain propagating steps (to the right of $\cdot QOOH$) or an O_2 addition (downward from $\cdot QOOH$). The isomerization involves the transfer of an H atom to the O_2 site, creating an OOH group. The isomerization is strongly dependent on the size and structure of the original fuel molecule and the site where the O_2 group is located (Pollard, 1977). Branched fuel molecule structures, such as isooctane, hinder the isomerization process, inhibiting LTHR.

The $\cdot O_2QOOH$ can isomerize further, and this isomerized product decomposes into a relatively stable ketohydroperoxide species and one OH radical (Westbrook, 2000). The ketohydroperoxide finally decomposes into several parts around 800 K, at least two of which are radicals, releasing heat. These radicals then promote hydrogen abstraction from the

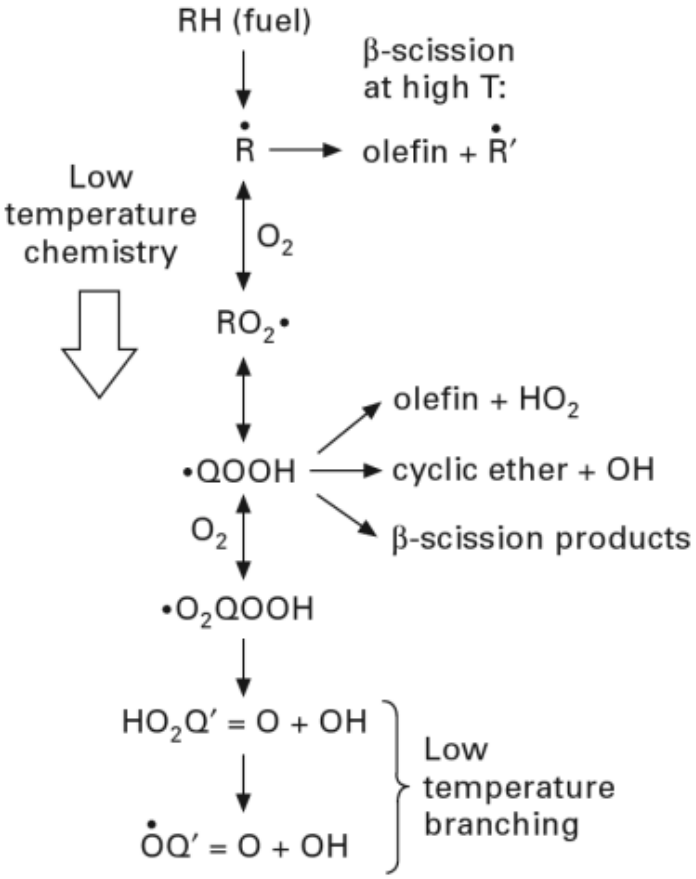

Figure 2.2: Diagram illustrating the different oxidation pathways for a hydrocarbon fuel (from Westbrook *et al.* (2007)).

fuel and the process continues until the unreacted fuel (RH) is depleted or until the the temperature increases to a point where the O_2 addition steps favor dissociation. This shift towards dissociation occurs at a temperature of about 850 K, the temperature limit of LTHR.

2.2 Intermediate- and high-temperature heat release

Above about 850 K, O_2 combines with hydrogen radicals via the reaction $H + O_2 + M \leftrightarrow HO_2 + M$ (Westbrook *et al.*, 2007). The resulting HO_2 can then abstract hydrogen from the fuel (RH), leading to an alkyl radical and hydrogen peroxide (H_2O_2). Hydrogen peroxide is relatively stable and accumulates until the temperature reaches about 1000 K. Above about 1000 K, the hydrogen peroxide decomposes into two OH radicals through the reaction $H_2O_2 + M \rightarrow OH + OH + M$. The decomposition of the accumulated hydrogen peroxide rapidly releases a significant amount of OH radicals that attack the fuel (or fuel fragments),

leading to rapid heat release. As the temperature increases, the H_2O_2 decomposition occurs at an increasing rate, finally resulting in hot-ignition through the chain branching step $H + O_2 \rightarrow H + OH$ at temperatures above about 1200 K. The hydrogen peroxide decomposition and chain branching reactions are elementary reactions shared by all hydrocarbon fuels, so the intermediate and hot-ignition temperatures are relatively independent of fuel type (Saxena and Bedoya, 2013).

2.3 Fuel effects

The structure of a hydrocarbon fuel dictates the fuel molecule's tendency towards hydrogen abstraction and internal isomerization. The relative ease of hydrogen abstraction and isomerization dictate the fuel's propensity to exhibit low-temperature heat release and dual stage ignition. The types of carbon-hydrogen bonds present on the fuel molecule play a major role in determining these trends.

Carbon-hydrogen bonds on a fuel molecule can be classified into: (1) primary bonds, (2) secondary bonds, and (3) tertiary bonds. Primary bonds are the strongest of the three bond types and are characterized by a carbon atom bonded to only one other carbon atom with three hydrogen atoms bonded to the remaining sites. Primary bonds are characteristic of the carbons on the ends of a fuel molecule chain. Secondary bonds are characteristic of the interior carbons in a fuel molecule chain with the carbon atom being bonded to two neighboring carbon atoms and the remaining sites bonded to two hydrogen atoms. Secondary bonds are weaker than primary bonds. Lastly, tertiary bonds are when the carbon atom is bonded to three carbon atoms an only a single hydrogen atom.

The relative strengths of the carbon-hydrogen bonds indicate that fuels with an increased number of secondary bonds, such as straight-chained (normal) alkanes, will exhibit a higher propensity to release heat at low temperatures. This is because hydrogen is more readily abstracted from secondary carbons and the isomerization can more easily occur by transferring a hydrogen atom from a secondary carbon compared to a primary carbon (Buda *et al.*, 2005). The isomerization also occurs more easily in long straight chain molecules because of the long chain length and flexibility of the molecule (Aceves *et al.*, 2007). For these reasons, n-heptane exhibits a high propensity for low-temperature heat release. In contrast, iso-octane exhibits very little low temperature heat release because its branched structure results in an increased number of primary bonds (Buda *et al.*, 2005).

2.4 Summary

In this chapter, the fundamental pathways of hydrocarbon oxidation are discussed. Emphasis is placed on distinct phases of heat release and the characteristics of these phases. Fuel effects are also discussed.

Chapter 3

Chemical kinetic mechanisms

The reaction of a generic hydrocarbon fuel with air in stoichiometric proportions can described globally by Eq. 3.1. The major combustion products are CO_2 and H_2O with N_2 acting as an inert. The amount of CO_2 produced per fuel molecule burned is proportional to the fuel carbon number (α).

$$C_\alpha H_\beta O_\gamma + \left(\alpha + \frac{\beta}{4} - \frac{\gamma}{2}\right)(O_2 + 3.76N_2) \rightarrow \alpha CO_2 + \frac{\beta}{2}H_2O + \left(\alpha + \frac{\beta}{4} - \frac{\gamma}{2}\right)N_2 \qquad (3.1)$$

The proportions of fuel and oxidizer in a reacting system may not be stoichiometric. The proportions of fuel and oxidizer are often defined in terms of the equivalence ratio (ϕ) described by Eq. 3.2, where m indicates mass and n indicates number. If there is excess fuel, $\phi > 1$. If there is excess oxidizer, $\phi < 1$. For systems that use an oxidizer other than air, m_{air} or n_{air} in Eq. 3.2 should be replaced with m_{O_2} or n_{O_2}, respectively. In some applications, the inverse of ϕ is used, termed the normalized air-fuel ratio and denoted as λ.

$$\phi = \frac{m_{fuel}/m_{air}}{(m_{fuel}/m_{air})_{stoich.}} = \frac{n_{fuel}/n_{air}}{(n_{fuel}/n_{air})_{stoich.}} = \frac{1}{\lambda} \qquad (3.2)$$

The global reaction described by Eq. 3.1 is an over-simplification of what occurs in a real system. In reality, there are intermediate reaction steps to get from fuel and oxidizer to combustion products. These intermediate steps are elementary reactions, which can be thought of as reactions that actually (or very near actually) occur. An example elementary reaction is the reaction $H + O_2 \leftrightarrow OH + O$. This chain-branching reaction is one of the most important reactions in combustion because two radicals are produced (OH, O) from one (H). Chain-branching reactions rapidly increase the radical pool, leading to the explosive nature of combustion. To describe a global reaction, such as Eq. 3.1, a set of elementary reactions are needed, with the size of the elementary reaction set generally depending on the size of the fuel molecule considered.

3.1 Elementary reaction rates

A general bi-molecular elementary reaction can be written as Eq 3.3, which is permitted to occur in both the forward and reverse directions. Here, a, b, c, and d are the stoichiometric coefficients for species A, B, C, and D. The reaction rate constant in the forward direction is k_f and the reaction rate constant in the reverse direction is k_b. As such, the net rate of change in the concentration of species A can be written as Eq. 3.4. Generally, the reaction rates k are Arrhenius as described by Eq. 3.5, where A_0 is the pre-exponential factor, E_a is the activation energy, and R_u is the ideal gas constant. The ratio E_a/R_u has units of temperature an is termed the activation temperature (T_a). The pre-exponential factor A_0 expresses the frequency at which the reactant molecules collide, while $\exp(-T_a/T)$ expresses the likelihood that a collision leads to reaction. This probability of reaction depends on the activation energy E_a which can be viewed as the energy barrier that must be overcome for the reaction to take place. The term T^b represents an additional temperature dependence of the collision frequency that has a weaker effect on the reaction rate than the exponential factor. Often, only the forward rate k_f is specified, but the reverse rate can be calculated using the equilibrium constant $K_c = k_f/k_b$ which is a function of the thermodynamic state and thermodynamic properties of the reaction species.

$$aA + bB \underset{k_b}{\overset{k_f}{\rightleftarrows}} cC + dD \tag{3.3}$$

$$\frac{d[A]}{dt} = k_f[A]^a[B]^b - k_b[C]^c[D]^d \tag{3.4}$$

$$k = A_0 T^b \exp\left(\frac{-E_a}{R_u T}\right) = A_0 T^b \exp\left(\frac{-T_a}{T}\right) \tag{3.5}$$

3.2 Detailed chemical mechanisms

Real fuels are complex mixtures of hundreds of hydrocarbon compounds including linear and branched paraffins, naphthenes, olefins and aromatics (Mehl *et al.*, 2011b). Fortunately, real fuel behavior can often be adequately reproduced by simpler fuel surrogates containing a limited number of pure components. For certain pure fuel components, or mixtures of these pure fuel components, detailed chemical mechanisms have been constructed containing a descriptive set of elementary reactions. Often, chemical mechanisms for more complex fuels can be created using a hierarchal structure (Westbrook and Dryer, 1984) by using sub-mechanisms for simpler molecules. As such, the size of the chemical mechanism generally increases with the size of the fuel molecule. The increase is largely due to the increased number of intermediate species and their isomers.

The size of selected mechanisms from Lawrence Livermore National Laboratory (LLNL) are summarized in Table 3.1. It can be seen in Table 3.1 that the number of species and

Table 3.1: Size of selected detailed chemical mechanisms from LLNL

Fuel name	Formula	Species	Reactions	Ref.
Hydrogen	H_2	10	21	O'Connaire *et al.* (2004)
Ethanol	C_2H_5OH	57	383	Marinov (1999)
Butanol	C_4H_9OH	430	2336	Sarathy *et al.* (2012)
n-Heptane	nC_7H_{16}	654	2827	Mehl *et al.* (2011b)
iso-Octane	iC_8H_{18}	874	3796	Mehl *et al.* (2009)
PRFs	$nC_7H16 + iC_8H_{18}$	1034	4236	Curran (2002)

reactions increases drastically with the number of carbons in the fuel. Additionally, the last entry in the table for Primary Reference Fuels (PRFs), mixtures of iso-octane and n-heptane, is larger than the iso-octane mechanism but smaller than the direct combination of the iso-octane and n-heptane mechanisms. This is because the iso-octane mechanism shares many sub-mechanisms with the n-heptane mechanism.

While the hydrogen and ethanol mechanisms in Table 3.1 are of a reasonable size to be used in three-dimensional CFD and chemical kinetics simulations, the larger molecule fuel mechanisms can be prohibitively large depending on the number of grid points in the simulation. For this reason, there is great interest in reducing the size of these mechanisms while maintaining sufficient species and reaction steps to adequately reproduce relevant physical phenomena (e.g. ignition delay time, flame speed). Two levels of reduced mechanisms, the skeletal mechanism and the reduced mechanism, will be discussed in the following sections.

3.3 Reduced chemical mechanisms

When using a detailed chemical kinetic mechanism in a computation is prohibitive, smaller mechanisms that retain important features of the detailed mechanism are desired. The first level of reduction that removes species and the reactions associated with those species results in what is termed a *skeletal* mechanism. The "skeletal" mechanism has had information removed from the mechanism, so it is like a "skeleton" of the detailed mechanism. The next level of reduction employs the Quasi-Steady State Assumption (QSSA) to further simplify the mechanism, but retains the information about the QSS species. The resulting mechanism after invoking QSSA is termed a *reduced* mechanism. Details about these reduction processes are discussed below.

Reduction to skeletal mechanism

The idea behind the skeletal mechanism is simple: eliminate unimportant species and reactions while maintaining the relevant fundamental predictions of the detailed mechanism. There are numerous methods used to develop skeletal mechanisms, including: (1) directed

relation graph (DRG) (Lu and Law, 2005), (2) computational singular perturbation (CSP) (Lam and Goussis, 1994), and (3) sensitivity analysis (Tomlin *et al.*, 1994).

The DRG method uses a graphical representation of species relationships to identify important/unimportant groups of species. DRG specifically aims to address issues of species coupling within the mechanism (Lu and Law, 2005). That is, if there is strong coupling between certain species, removing one of the species would necessitate removal of all species in the group. Alternatively, if a certain species must be included in the mechanism, species that it is strongly coupled to must also be retained. A coupling threshold is specified by the user in the DRG method and groups of species that have below-threshold relations to the desired species (e.g. fuel components, combustion products) are removed. Variants on the DRG method also exist, including DRG error propagation (DRGEP) (Pepiotdesjardins and Pitsch, 2008), among others.

The CSP method identifies the fast and slow modes of the system by analyzing the eigenvalues of the Jacobian matrix. Species that have very fast time scales can be effectively removed from the system or have their influence included through an assumption such as QSSA or partial equilibrium (Tomlin *et al.*, 1994).

The sensitivity analysis method analyzes the normalized first order sensitivity coefficient described by Eq. 3.6 using the detailed mechanism at a specified flame condition. Here, y is a flame parameter or feature of interest (e.g. ignition delay time, flame speed, mole fraction of species of interest, etc.) and α_i is the pre-exponential factor A_0 of reaction i. In other words, Eq. 3.6 describes how the parameter of interest depends on the reaction rate of each reaction (with a normalization factor). This allows the reactions to be ranked in order of importance by the magnitude of the sensitivity coefficient. Only reactions with normalized sensitivities above a threshold value will be included in the skeletal mechanism.

By construction, the sensitivity coefficient identifies the rate limiting steps in the chemical mechanism. For a set of reactions that occur in sequence, the sensitivity coefficient will be largest for the slowest reaction step. Conversely, for a set of reactions that occur in parallel, the sensitivity coefficient will be largest for the fastest reaction step. In this latter scenario, the sensitivity coefficient may not be adequate to identify all the unimportant steps. That is, the fastest reaction step may also have a fast reverse rate leading to a small net contribution to the production or destruction of the species in the reaction step.

$$\frac{(\alpha_i/y)(\partial y/\partial \alpha_i)}{\max_i |(\alpha_i/y)(\partial y/\partial \alpha_i)|} = \frac{\partial(\log y)/\partial(\log \alpha_i)}{\max_i |\partial(\log y)/\partial(\log \alpha_i)|} \tag{3.6}$$

The normalized production/destruction rates can be used to address this shortcoming, as described by Eqs. 3.7 and 3.8, respectively (Chang, 1995). Here, $\nu_{k,i}$ is the stoichiometric coefficient of the k-th species in the i-th reaction and ω_i is the rate of reaction progress for the i-th reaction step. The normalized production/destruction rate of a species for a given reaction may be large even if the sensitivity coefficient is small. This situation may occur for parallel reaction steps. Thus, using sensitivity information alone could omit some important reaction steps.

$$\bar{C}^{p}_{k,i} = \frac{\max(\nu_{k,i}, 0) q_i}{\sum_i \max(\nu_{k,i}, 0)\omega_i} \tag{3.7}$$

$$\bar{C}^{d}_{k,i} = \frac{\max(\nu_{k,i}, 0) q_i}{\sum_i \min(\nu_{k,i}, 0)\omega_i} \tag{3.8}$$

The following procedure outlines the development of a skeletal mechanism using the sensitivity analysis method:

1. Select reaction steps with normalized sensitivity coefficients larger than a specified threshold.
2. Examine the remaining reaction steps and include reactions with normalized production/destruction rates above a specified threshold.
3. Include all necessary species given the selected reaction steps.
4. Repeat (2) and (3) until no new species are added to the preliminary set.
5. Verify that the newly developed skeletal mechanism preserves the flame features of interest.

The selection of reaction steps is done at a specified condition, and the reaction steps chosen may change with the flame condition. Therefore, the developed mechanism is only valid at the intended conditions. However, if a more robust skeletal mechanism is required (i.e. a wide range of conditions are of interest), the selection of reaction steps can be performed at more than one flame condition and the cumulative reaction steps included in the skeletal mechanism. The size of the skeletal mechanism will generally increase as a wider range of conditions are targeted.

Reduction to reduced mechanism with QSS assumption

If the parent detailed mechanism is sufficiently large, it may not be possible to create a sufficiently small skeletal mechanism that is suitable for three-dimensional CFD simulations. If this is the case, further reduction can be accomplished by identifying species that are candidates for QSSA. For a homogeneous system, the QSSA states that the rate of change of the concentration of species k is zero, but not that the concentration itself is zero. This is expressed in Eq. 3.9, where $[C_k]$ is the concentration of species k, $\nu_{k,i}$ is the stoichiometric reaction coefficient of the k-th species in the i-th reaction and ω_i is the reaction rate of the i-th reaction.

$$\frac{d[C_k]}{dt} = 0 = \sum_i \nu_{k,i}\omega_i \tag{3.9}$$

If the consumption rate of an intermediate species is fast compared to its production rate, the species is a good candidate for the QSSA. One set of reactions where this is the case is the thermal NO reactions (Zeldovich mechanism):

$$N_2 + O \rightarrow NO + N \qquad k_1 = 1.8 \cdot 10^{14} \exp\left(-38,370/T\right) \tag{3.10}$$

$$N + O_2 \rightarrow NO + O \qquad k_2 = 1.8 \cdot 10^{10} \exp\left(-4,680/T\right) \tag{3.11}$$

The reaction described in Eq 3.10 has a much higher activation temperature than the reaction described in Eq. 3.11. As such, the reaction 3.10 is much slower at a given temperature relevant to combustion than the reaction 3.11. Because N is produced in reaction 3.10 and consumed in reaction 3.11, N is a good candidate for QSSA. Applying the QSSA to N gives:

$$\frac{d[N]}{dt} = k_1[N_2][O] - k_2[N][O_2] \approx 0 \rightarrow [N] \simeq \frac{k_1[N_2][O]}{k_2[O_2]} \tag{3.12}$$

Using Eq. 3.12 to simplify the NO production rate yields Eq. 3.13, which is no longer dependent on $[N]$. At high temperatures, the partial equilibrium assumption could be used to rewrite $[O]$ in terms on $[O_2]$ such that the NO production rate can be estimated using only the concentrations of major species, but that will not be discussed further here.

$$\frac{d[NO]}{dt} = k_1[N_2][O] + k_2[N][O_2] \simeq 2k_1[N_2][O] \tag{3.13}$$

This example illustrates how the QSSA can be applied, but is only for two reactions and no reverse rates. Because the detailed mechanisms considered in this work have many species and reactions, a computer program is used to identify QSSA species and construct the relations for their QSSA concentrations.

3.4 Computer Assisted Reduction Mechanism (CARM)

The Computer Assisted Reduction Mechanism (CARM) (Chen, 2001) is a computer code that automates the process of mechanism reduction. CARM uses CHEMKIN (Kee *et al.*, 1996) libraries and flame codes to evaluate choices during mechanism reduction. The program flow of CARM is illustrated in Fig. 3.1. First, the detailed mechanism is given to the CHEMKIN interpreter creating a binary link file that has species, reaction, and thermodynamic information. CHEMKIN flame or reactor code results are then computed at conditions of interest using the detailed mechanism, the output of which is a Save file that will be used for comparison when evaluating choices made for the skeletal/reduced mechanism. The CHEMKIN flame or reactor code is also used to compute the normalized sensitivity coefficients and normalized production/destruction rates. The typical reactor code used with

CARM is known as SENKIN (homogeneous, zero-dimensional, adiabatic) and the typical flame code is PREMIX (steady, one-dimensional, adiabatic). These codes will be described further in the next section.

Once the normalized sensitivity coefficients and production/destruction rates are available, the first round of species elimination takes place resulting in a skeletal mechanism. This skeletal mechanism is then compiled with the thermodynamic data into a link file which is used in the same reactor/flame code at the conditions of interest. If the results of the flame code agree with the detailed mechanism within a specified tolerance for the parameters and/or flame features of interest, then further reduction can be attempted using the current version of the skeletal mechanism. If the flame code results are not satisfactory, then the elimination of species must be attempted again using the previous version of the skeletal mechanism.

Determining the sensitivity coefficients generally requires running each condition of interest (i.e. temperature, pressure, composition, etc.) twice for each reaction in the chemical mechanism. The derivative in Eq. 3.6 is approximated numerically by increasing the pre-exponential factor A_0 by 50% for one run and decreasing A_0 by 50% for the other run. For large mechanisms, generating the sensitivity information is computationally expensive. For example, if we consider the n-heptane mechanism from LLNL (Mehl *et al.*, 2011b) with 2827 reaction steps and 654 reactions, it would require $2 \cdot 2827 = 5654$ computations to generate sensitivity coefficients at one condition. After the sensitivity coefficients are generated, species/reaction removal is informed by this information. The validation tests must then be carried out for all target conditions after each species removal. Sensitivity information may need to be re-computed after a certain number of species/reactions have been removed, or at more than one condition.

Alternatively, a brute force approach known as the Targeted Search Algorithm (TSA) (Tham *et al.*, 2008) can be adopted. In this approach, the species are ordered by their maximum concentration at the conditions of interest and the species are removed one by one starting with the species of lowest concentration, as these species are good candidates for removal. Reactions associated with the removed species are also removed. After each species/reaction removal, testing of the new mechanism at the target conditions is done to verify if the removal of the species is warranted. In this approach, the number of computations is the product of the number of species and the number of target conditions. For the n-heptane mechanism from LLNL (Mehl *et al.*, 2011b) at a single target condition, the number of computations would be 654. The number of computations for the TSA approach at one target condition is about an order of magnitude less than the number of computations required to generate sensitivity information at one target condition. In short, the TSA approach can be a computationally efficient way to develop a skeletal mechanism from a detailed mechanism. Additionally, it is computationally efficient to remove as many unimportant species using DRG as possible while remaining within specified error bounds before generating sensitivity information or undertaking the TSA approach. The DRG-TSA combination is the reduction method used in this work.

When no further reduction can be achieved for the skeletal mechanism, the QSSA is

employed by CARM to create the reduced mechanism. QSSA species are selected based on their concentration levels in conjunction with a rate-of-production analysis. After selection of the QSS species, a set of independent elementary reaction steps is chosen to eliminate the QSS species in order to permit systematic construction of the reduced mechanism. Algebraic expressions for the QSS species are obtained in terms of the concentrations of the major species such that the QSS species can be solved for numerically, as they are non-linearly coupled. The detailed algebraic procedures are formulated in terms of matrix operations (Chen, 1988). The resulting iteration of the reduced mechanism is a CKWYP subroutine that replaces the inherent subroutine in the CHEMKIN library. The CKWYP subroutine returns the molar production rates for each species given the pressure, temperature, and species mass fractions. Modifications to the CKWYP subroutine are needed because the global reaction rates are expressed in terms of the elementary reaction rates which may be functions of the QSSA species concentrations. This modified subroutine is written automatically by CARM for each iteration of the reduced mechanism. The iteration process is similar to that used for developing the skeletal mechanism.

3.5 CHEMKIN

CHEMKIN (Kee *et al.*, 1996) is a FORTRAN based software package used for the computation of chemical equilibrium, zero-dimensional transient chemical kinetics, and one-dimensional steady state flames. CHEMKIN is structured with two main components: (1) an interpreter that builds a binary link file with the species, reaction, and thermodynamic data from text based inputs and (2) a library of gas-phase subroutines that return information about elements, species, reactions, equations of state, thermodynamic properties, and/or chemical production rates. The structure of the CHEMKIN package is shown in Fig. 3.2. The interpreter and gas-phase subroutine library are common to the application codes that solve the types of problems mentioned above. Two of the commonly used application codes are SENKIN, which computes the time-dependent chemical state of a zero-dimensional reacting system, and PREMIX, which computes the steady solution to a freely-propagating or burner-stabilized one-dimensional laminar flame.

SENKIN

SENKIN computes the time-dependent chemical state of a zero-dimensional gas-phase adiabatic reacting system at constant pressure or constant volume. The governing equations of the system are the conservation of mass and energy. The conservation of mass for a closed system is described by Eq. 3.14 where m_k is the mass of species k.

$$\frac{dm}{dt} = \frac{d\left(\sum_k m_k\right)}{dt} = 0 \tag{3.14}$$

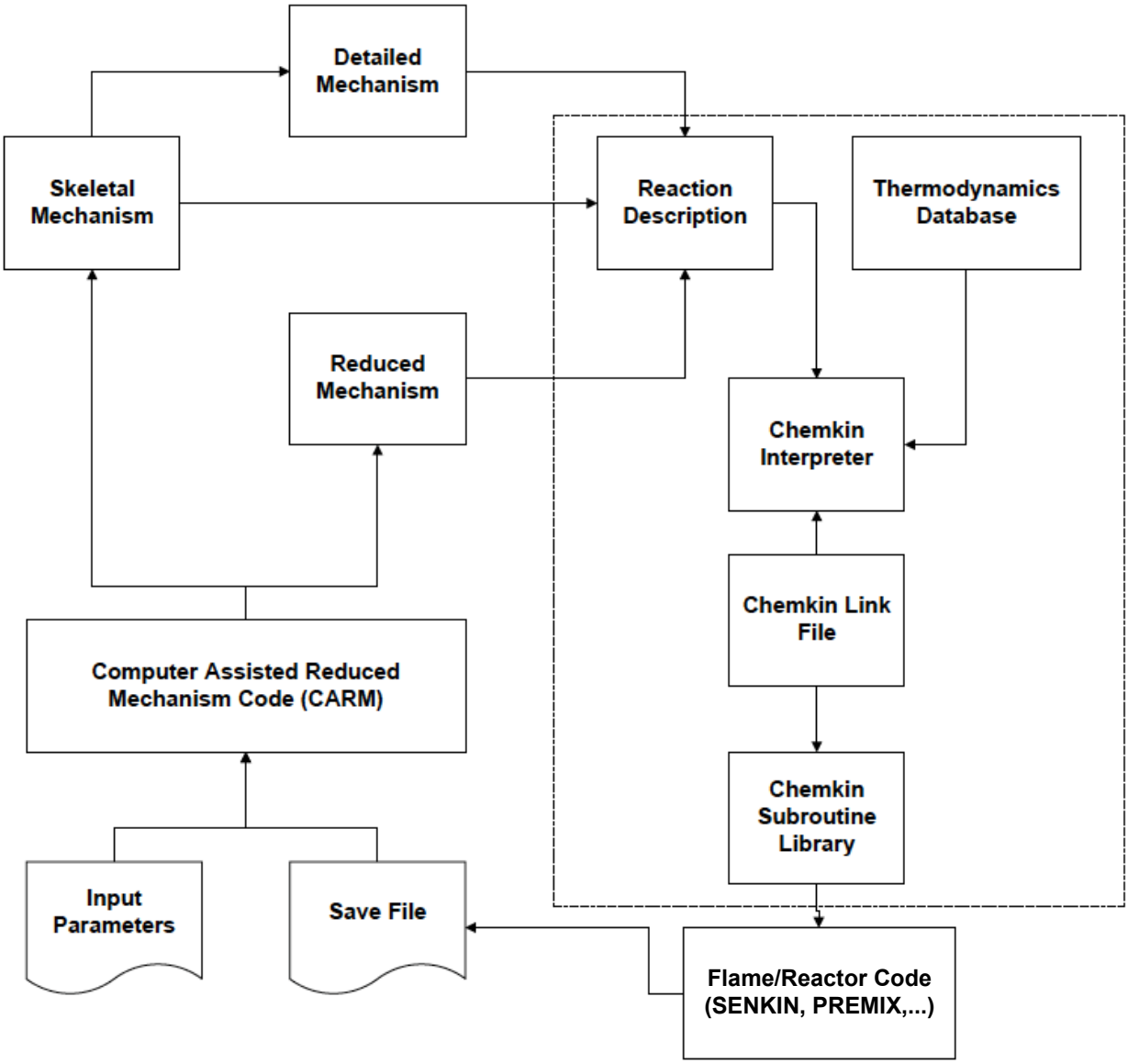

Figure 3.1: Flowchart of the CARM program which utilizes CHEMKIN flame codes to develop reduced mechanisms (modified from Chien (2010)).

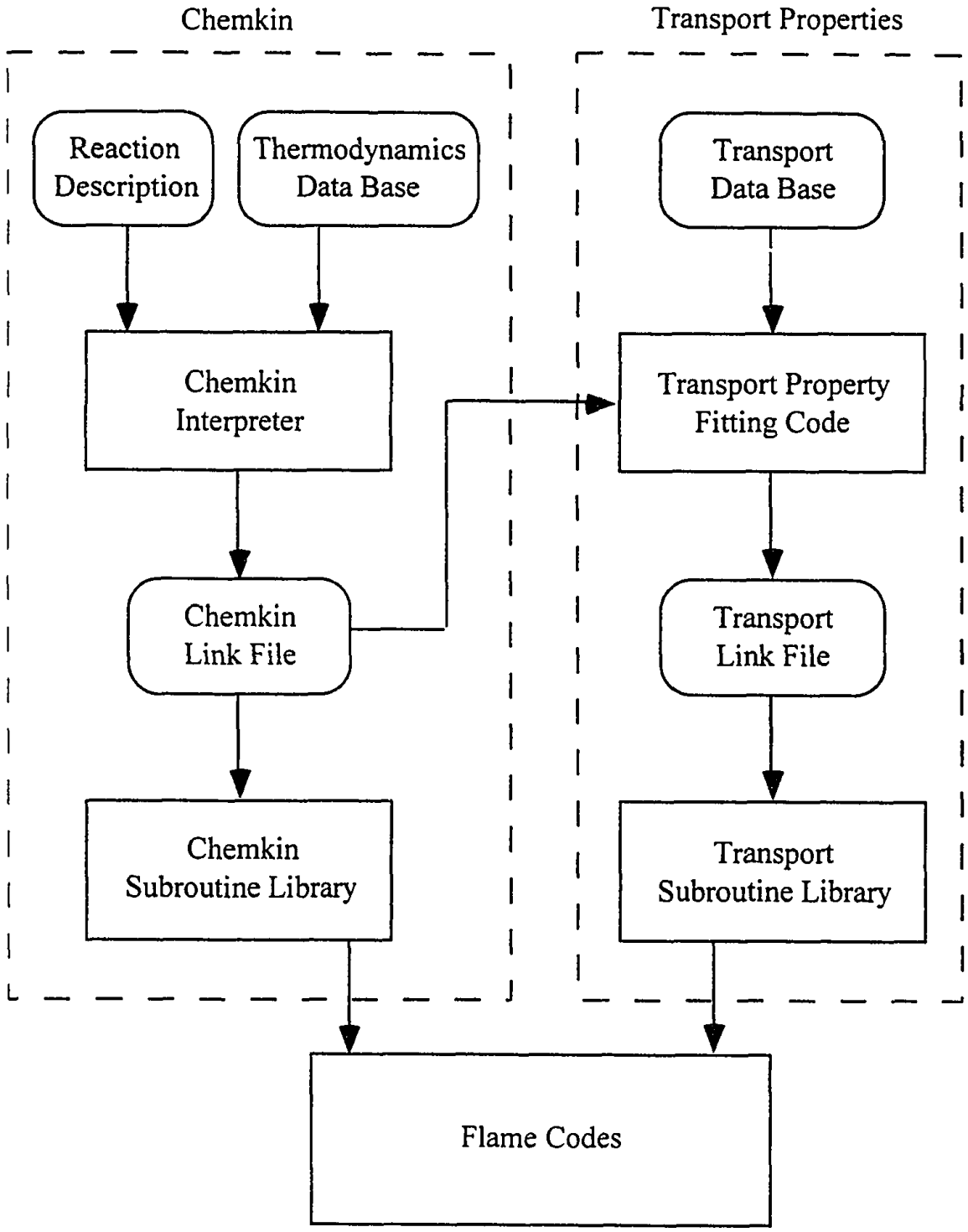

Figure 3.2: Flowchart of the CHEMKIN and Transport packages. The CHEMKIN package has an interpreter and gas-phase subroutine library and the Transport package has a transport property fitting code and transport subroutine library. The outputs of the CHEMKIN and Transport packages are common to each flame code (reprinted from Chang (1995)).

The rate of change of each species can be expressed using mass fractions since the total mass is constant, as in Eq. 3.15. Here, $Y_k = m_k/m$ is the mass fraction of species k, ν is the specific volume, $\dot{\omega}_k$ is the production rate of species k, and W_k is the molecular weight of species k.

$$\frac{dY_k}{dt} = \nu \dot{\omega}_k W_k \tag{3.15}$$

For a specified constant volume system, the energy equation can be written as Eq. 3.16, where c_v is the constant volume specific heat, T is the temperature, and u_k is the specific internal energy of species k. The pressure is calculated using the ideal gas law.

$$c_v \frac{dT}{dt} + \nu \sum_k u_k \dot{\omega}_k W_k = 0 \tag{3.16}$$

For a specified constant pressure system, the energy equation can be written as Eq. 3.17, where c_p is the constant pressure specific heat and h_k is the specific enthalpy of species k. In each case, the mixture specific heat is calculated using a mass-weighted average of the species specific heats.

$$c_p \frac{dT}{dt} + \nu \sum_k h_k \dot{\omega}_k W_k = 0 \tag{3.17}$$

SENKIN is generally used to calculate the *ignition delay time*, which is often defined for a homogeneous reacting mixture as the time delay from the start of the simulation to a specified temperature rise (usually 400 K). The ignition delay time is a characteristic parameter that indicates how readily a fuel will auto-ignite at a given condition and is important for CI engine concepts. In this work, SENKIN is run only in the constant pressure mode.

PREMIX

PREMIX computes the structure of a steady, one-dimensional, isobaric, freely-propagating or burner-stabilized flame. In this work, only the freely-propagating flame option is considered. The mass flow rate given in Eq. 3.18 is a computed eigenvalue such that the flame is stationary. In Eq. 3.18, ρ is the density, u is the velocity, and A is the cross-sectional area of the stream tube encompassing the flame.

$$\dot{m} = \rho u A \tag{3.18}$$

The conservation of species can be written as Eq. 3.19, where Y_k is the mass fraction of species k, $\dot{\omega}_k$ is the production rate of species k, W_k is the molecular weight of species k, and V_k is the diffusion velocity of species k. One approximation for the diffusion velocity is Eq. 3.20 which holds if all but one of the species are assumed to be in trace quantities (species N is abundant) (Law, 2006). That is, the interaction of any species k is dominated by its interaction with species N. This assumption is reasonable for combustion in air because

of the abundance of nitrogen (N_2). In Eq. 3.20, $D_{k,N}$ is the binary diffusion coefficient of species k in species N.

$$\dot{m}\frac{dY_k}{dx} + \frac{d}{dx}\left(\rho A Y_k V_k\right) - A\dot{\omega}_k W_k = 0 \tag{3.19}$$

$$V_k \simeq -D_{k,N}\nabla \ln Y_k = -D_{k,N}\frac{\nabla Y_k}{Y_k} \tag{3.20}$$

The conservation of energy can be written as Eq. 3.21, where T is the temperature, c_p is the mixture constant pressure specific heat, λ is the thermal conductivity, and $c_{p,k}$ is the constant pressure specific heat of species k.

$$\dot{m}\frac{dT}{dx} - \frac{1}{c_p}\frac{d}{dx}\left(\lambda A\frac{dT}{dx}\right) + \frac{A}{c_p}\sum_k \dot{\omega}_k W_k h_k + \frac{A}{c_p}\sum_k \rho c_{p,k} Y_k V_k \frac{dT}{dx} = 0 \tag{3.21}$$

It is apparent in Eqs. 3.19 and 3.21 that transport properties are required (e.g. binary diffusion coefficients, thermal conductivity). CHEMKIN has a transport property package that is used to evaluate viscosities, thermal conductivities, mass diffusion coefficients, and thermal diffusion coefficients. Similar to the main CHEMKIN package, the transport package has two main components: (1) transport properties fitting code and (2) a gas-phase transport subroutine library. As illustrated in Fig. 3.2, the transport properties fitting code reads thermodynamic data from the binary link file and information from the transport database to compute the transport link file, which contains polynomial fits to the temperature dependent pure species viscosities and binary diffusion coefficients. The transport subroutine library has functions that return pure species properties, mixture-average properties, or multi-component properties. The transport properties package is needed for the one-dimensional flame codes that utilize CHEMKIN.

In this work, PREMIX is used primarily to compute the laminar, un-stretched, planar flame speed. The flame speed is an important parameter in spark-ignited engines because a flame propagates through the charge, consuming the fuel. The speed at which the flame propagates dictates the fuel consumption rate and, therefore, the heat release rate.

3.6 Summary

In this chapter, the basics of chemical kinetics are briefly reviewed. The difficulty of using detailed chemical kinetic mechanisms for large molecules, such as conventional transportation fuels, is highlighted and the development of smaller skeletal and reduced mechanisms from large detailed mechanism using CARM is discussed. The chemical kinetics software package CHEMKIN and two common flame codes are also discussed.

Chapter 4

Reduced mechanism

A 96-species reduced mechanism for a 4-component gasoline surrogate has been developed from a 305-species skeletal mechanism given in Mehl *et al.* (2011a) using the Computer Assisted Reduction Mechanism (CARM) algorithm (Chen, 2001). The 96-species reduced mechanism is comprised of 92 reactions and 209 quasi-steady-state (QSS) species. The 305-species skeletal mechanism includes 1491 reaction steps and was derived from a detailed mechanism (Mehl *et al.*, 2011b) from LLNL with 1389 species and 5935 reaction steps.

4.1 Development

In the CARM algorithm, QSS species are identified by evaluating their concentration levels and with the help of a rate-of-production analysis. After selection of the QSS species, a set of independent elementary reaction steps is chosen to eliminate the QSS species in order to permit systematic construction of the reduced mechanism. Algebraic expressions for the QSS species are obtained in terms of the concentrations of the major species such that the QSS species can be solved for numerically, as they are non-linearly coupled. CARM evaluates choices made for mechanism reduction by comparing CHEMKIN (Kee *et al.*, 1996) flame code (e.g. SENKIN, PREMIX, etc.) results using the newly developed reduced mechanism to those of the detailed mechanism at target conditions of interest. If the choice of QSS species leads to agreement of flame code results between the newly reduced and detailed mechanisms, the mechanism is saved and further refinement can be attempted in the subsequent iteration (Tham *et al.*, 2008). Conversely, if there is not agreement between the newly developed reduced mechanism and the detailed one, the choice of QSS species is attempted again using the previous successful iteration of the reduced mechanism. This process continues until no further reduction can be achieved. The criteria used in the current study are 10% (rel.) and 0.1 μs (abs.) for auto-ignition delay time and 30 K (abs.) for adiabatic flame temperature. The adiabatic flame temperature is given a tolerance because it influences flame speed, pollutant formation, and heat transfer, in addition to other flame attributes.

The current mechanism was reduced using the target conditions for auto-ignition delay

Table 4.1: CARM target conditions

Condition	ϕ	T [K]	P [bar]	t_{ign} [ms]	T_{ad} [K]
1	0.2	750	10	534.5	1253
2	0.2	750	80	46.90	1247
3	0.3	800	40	23.20	1525
4	0.6	800	10	74.40	2122
5	0.6	1100	10	1.710	2364
6	0.6	750	60	6.730	2083
7	0.6	1000	60	0.990	2296
8	1.0	800	10	40.46	2617
9	1.0	750	60	4.020	2652
10	2.0	1100	10	1.350	2326
11	2.0	700	20	12.40	1974
12	2.0	800	40	2.150	2060

time (t_{ign}) and adiabatic flame temperature (T_{ad}) presented in Table 4.1 for the 4-component gasoline surrogate from Mehl *et al.* (2011a) in air. The target conditions span lean to rich mixtures at pressures and temperatures characteristic of boosted CI engine operation. Flame speed target conditions were not considered for the current mechanism reduction, however, flame speed was considered for the development of the skeletal mechanism. Further refinement of the reduced mechanism could incorporate flame speed targets, although the size of the mechanism would likely increase. Consideration of flame speed target conditions could be important for mechanisms used in simulations of SACI and SI engine operation where flame propagation is important. Additionally, NO_x reactions were not included in the detailed mechanism and are therefore absent from the reduced mechanism (these reactions will be included in a refined version of the reduced mechanism presented later in this chapter).

The reduced mechanism non-QSSA species are presented in Table 4.2. The reduced mechanism effective reactions (given the QSSA species) are presented in Table A.1.

4.2 Validation

Auto-ignition delay time

The reduced mechanism has been validated for auto-ignition by comparing SENKIN simulations with the reduced mechanism to SENKIN simulations with the detailed mechanism and experimental shock tube data (Gauthier *et al.*, 2004). Table 4.3 summarizes the current gasoline surrogate from Mehl *et al.* (2011a) and the gasoline and gasoline surrogates used in Gauthier *et al.* (2004). Figures 4.1 and 4.2 compare t_{ign} from simulations and experiments for $\phi = 1.0$ (0% EGR) and $\phi = 0.5$ (0% EGR), respectively, at 20 atm and 55 atm. Figures 4.3 and 4.4 compare t_{ign} from simulations and experiments for $\phi = 2.0$ (0% EGR) and

Table 4.2: Reduced mechanism species (non-QSSA)

IC8H18	O2	N2	CO2
H2O	NC7H16	C5H10-2	C6H5CH3
H	H2	O	OH
HO2	H2O2	CO	CH2O
CH3OH	CH3O2H	CH3O2	CH4
CH3	C2H6	C2H5	C2H4
CH3CHO	CH2CO	CH3COCH3	CH3COCH2O2H
C2H3CHO	C2H5CHO	C3H6	C3KET13
CH3CHCO	C4H6	PC4H9O2	C4H8OOH1-3O2
NC4KET13	C2H5COCH2	NC3H7CHO	TC4H9
IC4H8	TC4H9O2	TC4H9O2H	IC3H7CHO
IC3H5CHO	IC3H6CO	IC4H7OOH	C5H81-3
O2C5H10OH-2	C7H14-3	C7H15O2-1	C7H15O2-2
C7H15O2-3	C7H15O2-4	C7H14OOH1-3O2	C7H14OOH2-4O2
C7H14OOH3-2O2	C7H14OOH3-4O2	C7H14OOH3-5O2	C7H14OOH4-2O2
NC7KET24	NC7KET35	NC7KET42	BC5H10
CH3CHCHO	YC7H14	ACC6H10	NEOC5H11O2
NEOC5H10OOH-O2	C4H7CHO2-2	IC8H16	JC8H16
AC8H17O2	BC8H17O2	CC8H17O2	DC8H17O2
IC8ETERAB	IC8ETERAC	IC8ETERBD	AC8H16OOH-BO2
BC8H16OOH-CO2	DC8H16OOH-BO2	IC3H7COC3H6-T	TC4H9COC2H4S
C6H5CH2J	HOC6H4CH3	C6H5OH	CYPDONE
C6H5CH2OH	C6H5CHO	O2C6H4CH3	C5H92O2-4
C5H91O2-3	CY3C5H8O	CH2	C2H2

$\phi = 0.5$ (20% EGR), respectively, at 20 atm and 55 atm. Overall, there is good agreement between the t_{ign} calculated using SENKIN with the reduced mechanism to that calculated with the detailed mechanism and experimental data. In general, the reduced mechanism predicts slightly shorter t_{ign} than the detailed mechanism at high temperatures ($T \gtrsim 900$ K) and low temperatures ($T \lesssim 700$ K). Compared to the detailed mechanism, the negative temperature coefficient (NTC) range is well captured using the reduced mechanism. The NTC range is the range of the ignition delay plot where increasing temperature (moving to the left on the $1000/T$ axis) increases ignition delay times as the mixture is less reactive. The NTC phenomena is a result of of the increased production of HO_2, which abstracts hydrogen from the fuel to create the metastable H_2O_2 (Law, 2006). It is not until H_2O_2 decomposes into two OH radicals at sufficiently high temperatures that the fuel oxidation accelerates again.

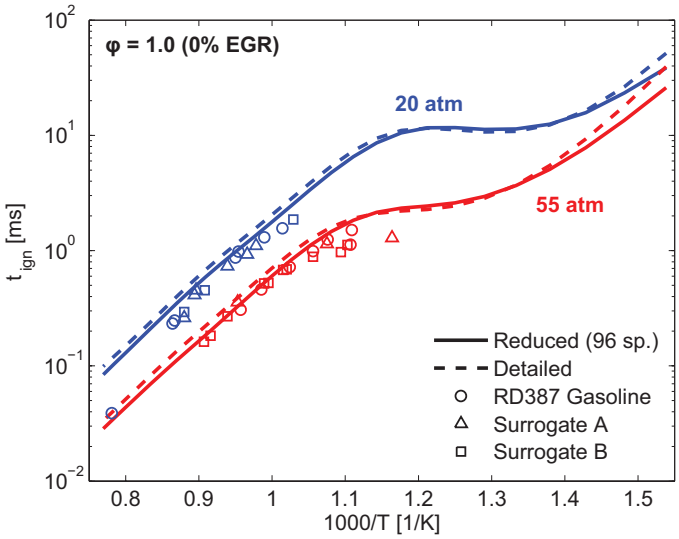

Figure 4.1: Auto-ignition delay times for $\phi = 1.0$, 0% EGR from simulations (lines) and experiments (symbols) at 20 atm and 55 atm. The reduced mechanism shows good agreement with the detailed mechanism and experimental data.

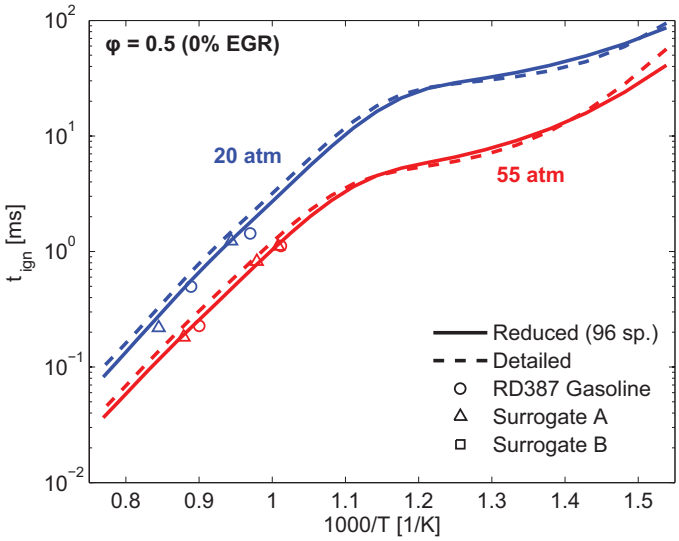

Figure 4.2: Auto-ignition delay times for $\phi = 0.5$, 0% EGR from simulations (lines) and experiments (symbols) at 20 atm and 55 atm. The reduced mechanism shows good agreement with the detailed mechanism and experimental data.

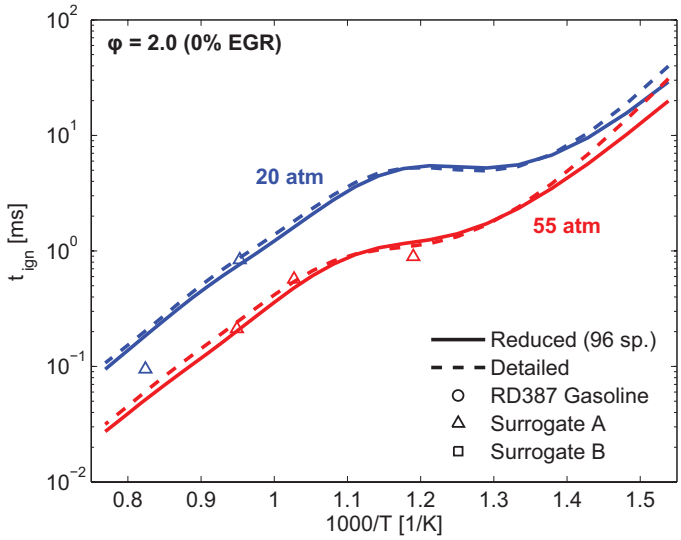

Figure 4.3: Auto-ignition delay times for $\phi = 2.0$, 0% EGR from simulations (lines) and experiments (symbols) at 20 atm and 55 atm. The reduced mechanism shows good agreement with the detailed mechanism and experimental data.

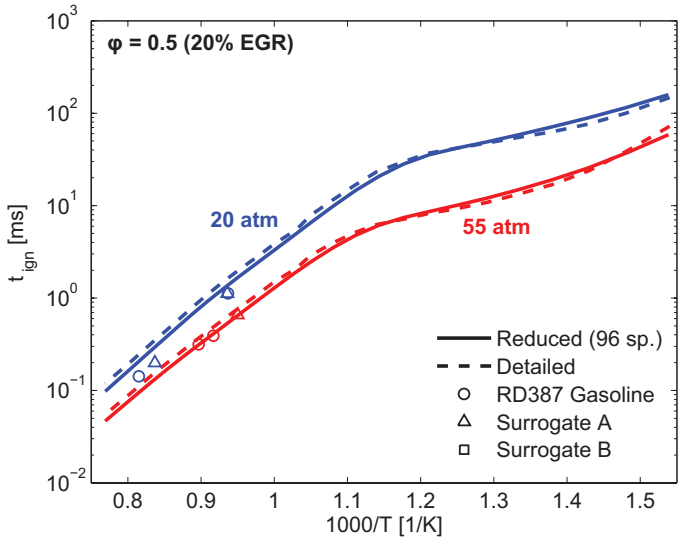

Figure 4.4: Auto-ignition delay times for $\phi = 0.5$, 20% EGR from simulations (lines) and experiments (symbols) at 20 atm and 55 atm. The reduced mechanism shows good agreement with the detailed mechanism and experimental data.

Table 4.3: Composition (liq. vol. %) of gasoline and gasoline surrogates

Fuel	iC_8H_{18}	nC_7H_{16}	$C_6H_5CH_3$	C_5H_{10}–2
Current Surrogate	57%	16%	23%	4%
Surrogate A	63%	17%	20%	0%
Surrogate B	69%	17%	14%	0%
RD387 Gasoline	Many components; (RON+MON)/2 = 87			

Laminar flame speed

Although the reduced mechanism was not developed using target conditions for laminar flame speed, it is useful to evaluate how the reduced mechanism performs for laminar flame speed calculations. Laminar flame speeds of gasoline surrogate/air mixtures calculated using CHEMKIN with the reduced mechanism are compared to laminar flame speeds calculated using the detailed mechanism (results from Mehl *et al.* (2011a)) at 373 K and 10-25 atm in Fig. 4.5. These conditions were chosen because they correspond to experimental data from Jerzembeck and Peters (2009) that was used to validate the detailed mechanism. There is good agreement between the reduced and detailed mechanisms near stoichiometric conditions, with the reduced mechanism slightly over predicting the laminar flame speed. For $\phi \lesssim 0.85$, the reduced mechanism under-predicts the laminar flame speed compared to the detailed mechanism with increasing difference between the reduced and detailed mechanism as ϕ becomes smaller.

The reduced mechanism was also validated for laminar flame speeds at a pressure of 1 bar and temperatures of 323 K, 348 K, and 373 K at a range of ϕ. The computed laminar flame speed with the reduced mechanism is compared to that of the detailed mechanism (data from Mehl *et al.* (2011a)) in Fig. 4.6. It can be seen in Fig. 4.6 that the reduced mechanism consistently over-predicts the laminar flame speed compared to the detailed mechanism at these conditions. The reduced mechanism predicts about a 15% higher laminar flame speed than the detailed mechanism near $\phi = 1.1$, with better agreement between the reduced and detailed mechanisms as ϕ moves away from $\phi = 1.1$.

The computed laminar flame speeds using the reduced mechanism at a pressure of 1 bar, temperatures of 323 K, 348 K, and 373 K, and a range of ϕ are plotted against experimental laminar flame speed values from Tian *et al.* (2010) in Fig. 4.7. At the lowest temperature in Fig. 4.7 of 323 K, the reduced mechanism over-predicts the laminar flame speed compared to the experiment. However, at temperatures of 348 K and 373 K, the reduced mechanism agrees well with the experiment at the limited number of experimental data points available.

Because temperatures near TDC for the GCI/PFS cases considered in this work are much hotter than 373 K and the pressure near TDC can be in excess of 60 bar for boosted intake pressure, laminar flame speeds of gasoline surrogate/air mixtures at temperatures and pressures characteristic of near-TDC in-cylinder conditions computed with the reduced and skeletal mechanisms are presented in Fig. 4.8. The reduced mechanism generally predicts laminar flame speeds within $\sim 10\%$ of the skeletal mechanism, over-predicting for $\phi \gtrsim 0.5$ and

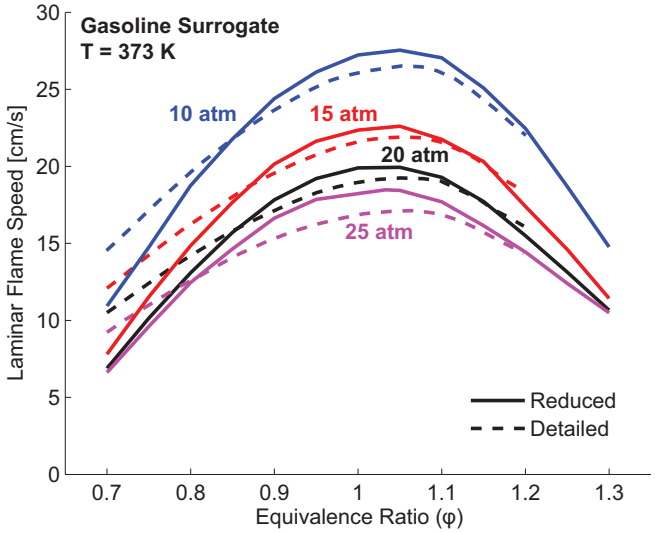

Figure 4.5: Simulated laminar flame speeds of gasoline surrogate/air mixtures at 373 K and 10-25 atm for the reduced and detailed (data from Mehl *et al.* (2011a)) mechanisms. There is good agreement between the reduced and detailed mechanisms near stoichiometric conditions, with the reduced mechanism under-predicting the laminar flame speed compared to the detailed mechanism for $\phi \lesssim 0.85$.

under-predicting for $\phi \lesssim 0.5$. The inaccuracy of predicted flame propagation speeds is not critical for the current work, however, as the sequential auto-ignition of different in-cylinder regions occurs much faster than flame propagation could account for.

4.3 Computational speedup

As a simple illustration of the computational speedup provided by the reduced mechanism, consider a SENKIN calculation for $\phi = 1.0$, $T = 1000$ K, $P = 20$ atm, and 0% EGR. Using a single processor, the detailed mechanism requires about 9 minutes 44 seconds, the skeletal mechanism requires about 27 seconds, and the reduced mechanism requires about 3.6 seconds. The reduced mechanism provides about 160x speedup compared to the detailed mechanism and about 7.5x speedup compared to the skeletal mechanism. The computational time for this problem scales approximately as the square of the number of species, as shown in Fig. 4.9. The computational speedup provided by the reduced mechanism is important for use in coupled CFD and chemical kinetics codes for large scale simulations, such as IC engine combustion.

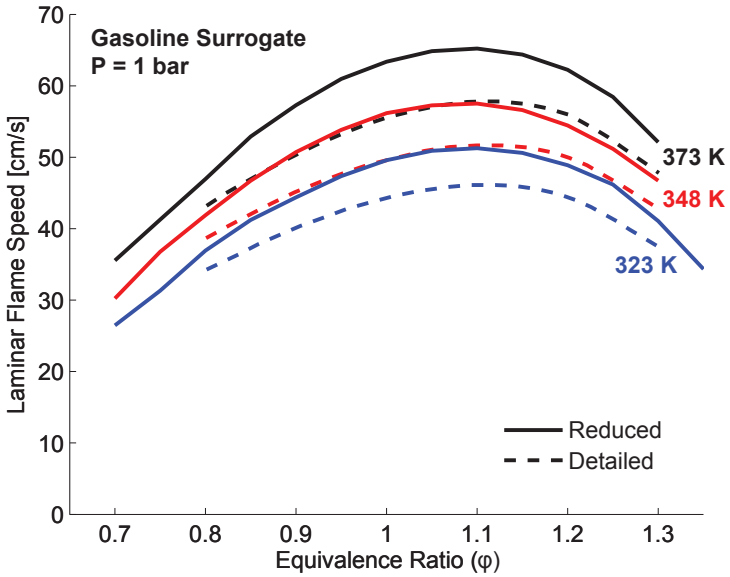

Figure 4.6: Simulated laminar flame speeds of gasoline surrogate/air mixtures at 1 bar and various temperatures for the reduced and detailed (data from Mehl *et al.* (2011a)) mechanisms. The reduced mechanism consistently over-predicts laminar flame speeds compared to the detailed mechanism at these conditions.

4.4 Including NO_x production

Oxides of nitrogen (NO_x) are an important pollutant to consider when developing an engine operating strategy. NO_x is formed though the thermal mechanism when temperatures exceed about 1800 K. Thus, including the production of NO_x in the reduced mechanism will be useful in certain situations. To accomplish this, the NO_x reactions in Table 4.4 are included in the skeletal mechanism (Mehl *et al.*, 2011a), increasing the number of species to 309 (addition of N, NO, NO_2, and N_2O) and the number of reaction steps to 1503. The reduced mechanism is then re-developed using the same targets as the original reduced mechanism (Table 4.1). Some reactions involve a third-body (M) that can be any species in the system. Some species are more efficient at enabling a specific reaction as a third-body, so collision efficiencies are often specified for select species. The physical concentration is multiplied by the collision efficiency (the default collision efficiency is 1.0) to get an effective concentration to use when determining the total concentration $[M]$. After adding the NO_x reactions to the skeletal mechanism, the resulting reduced mechanism has 98-species, adding NO and NO_2 to the original 96-species.

The 98-species reduced mechanism (including NO_x reactions) has been validated for auto-ignition by comparing SENKIN simulations with the reduced mechanism to SENKIN simulations with the detailed mechanism and experimental shock tube data (Gauthier *et al.*, 2004). Figures 4.10 and 4.11 compare t_{ign} from simulations and experiments for $\phi = 1.0$

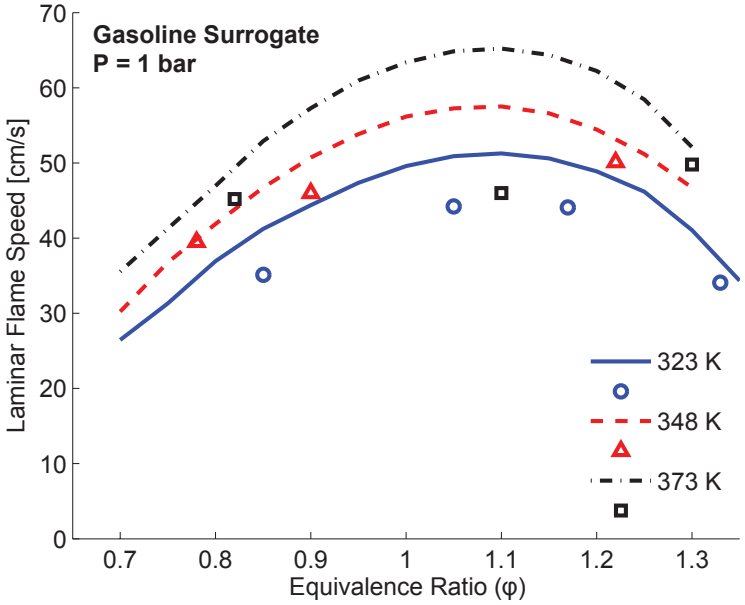

Figure 4.7: Simulated laminar flame speeds of gasoline surrogate/air mixtures at 1 bar and various temperatures for the reduced mechanism compared to experimental measurements from Tian *et al.* (2010). The reduced mechanism over-predicts the laminar flame speed compared to experiments at 323 K, but shows better agreement at 348 K and 373 K.

(0% EGR) and $\phi = 0.5$ (0% EGR), respectively, at 20 atm and 55 atm. Figures 4.12 and 4.13 compare t_{ign} from simulations and experiments for $\phi = 2.0$ (0% EGR) and $\phi = 0.5$ (20% EGR), respectively, at 20 atm and 55 atm. Overall, there is good agreement between the t_{ign} calculated using SENKIN with the 98-species reduced mechanism to that calculated with the detailed mechanism and experimental data. In general, the reduced mechanism predicts very similar t_{ign} than the detailed mechanism at high temperatures ($T \gtrsim 900$ K) and slightly shorter t_{ign} than the detailed mechanism at low temperatures ($T \lesssim 700$ K). Compared to the detailed mechanism, the negative temperature coefficient (NTC) range is well captured using the reduced mechanism. The 98-species reduced mechanism performs very similar to the 96-species reduced mechanism, with the 96-species reduced mechanism exhibiting slightly shorter t_{ign} at high temperatures. Throughout this paper, the original 96-species reduced mechanism without NO_x will be utilized for CFD simulations.

4.5 Summary

In this chapter, a novel 96-species reduced mechanism for a 4-component gasoline surrogate has been developed from a 305-species skeletal mechanism given in Mehl *et al.* (2011a) using the Computer Assisted Reduction Mechanism (CARM) algorithm (Chen, 2001). In addition,

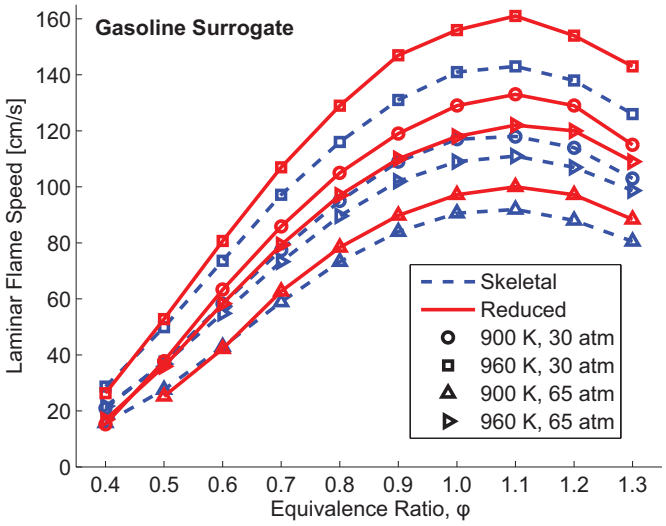

Figure 4.8: Simulated laminar flame speeds of gasoline surrogate/air mixtures at 900/960 K and 30/65 atm for the reduced and skeletal mechanisms. These temperatures and pressures are characteristic of near-TDC conditions for the gasoline surrogate engine simulations presented in this work. The reduced mechanism generally predicts laminar flame speeds within $\sim 10\%$ of the skeletal mechanism, over-predicting for $\phi \gtrsim 0.5$ and under-predicting for $\phi \lesssim 0.5$.

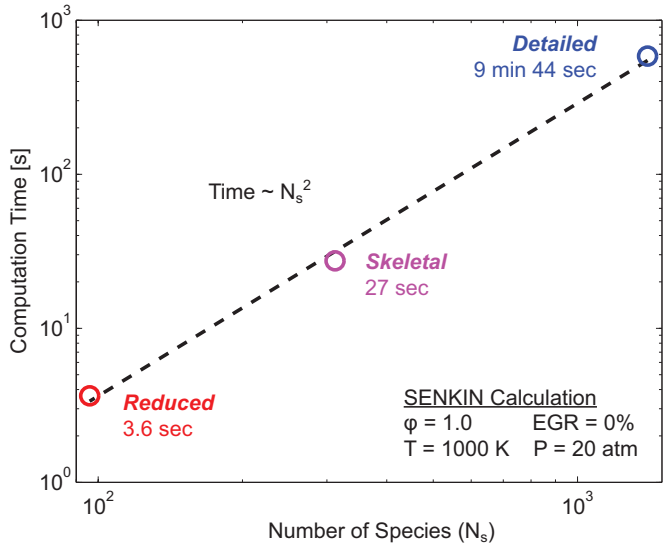

Figure 4.9: Computation time versus number of species (N_s) in the chemical mechanism for an example SENKIN calculation.

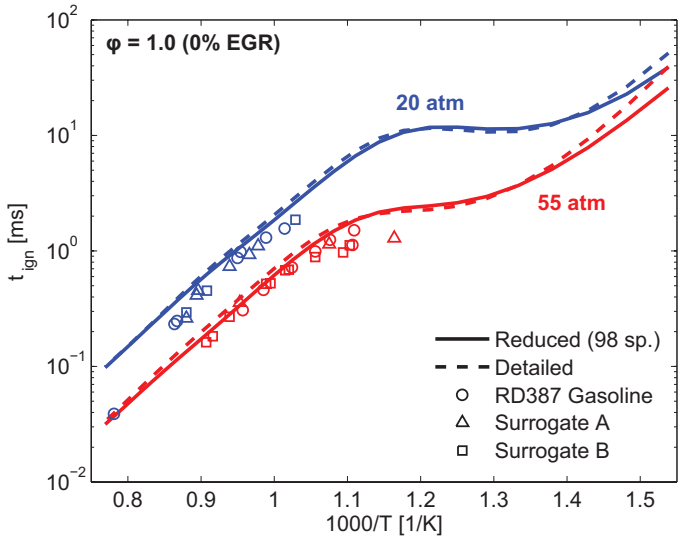

Figure 4.10: Auto-ignition delay times for $\phi = 1.0$, 0% EGR from simulations (lines) and experiments (symbols) at 20 atm and 55 atm. The reduced mechanism shows good agreement with the detailed mechanism and experimental data.

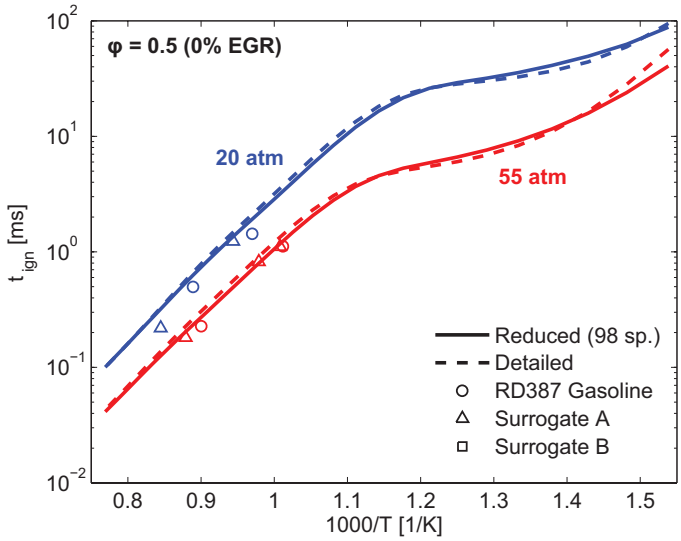

Figure 4.11: Auto-ignition delay times for $\phi = 0.5$, 0% EGR from simulations (lines) and experiments (symbols) at 20 atm and 55 atm. The reduced mechanism shows good agreement with the detailed mechanism and experimental data.

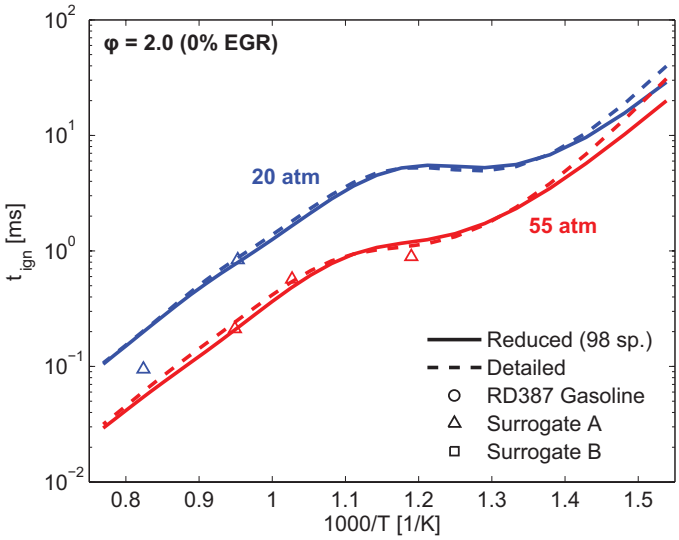

Figure 4.12: Auto-ignition delay times for $\phi = 2.0$, 0% EGR from simulations (lines) and experiments (symbols) at 20 atm and 55 atm. The reduced mechanism shows good agreement with the detailed mechanism and experimental data.

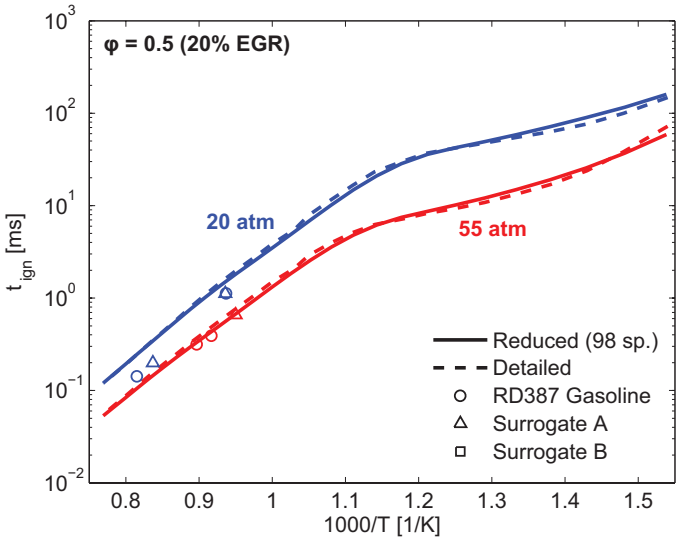

Figure 4.13: Auto-ignition delay times for $\phi = 0.5$, 20% EGR from simulations (lines) and experiments (symbols) at 20 atm and 55 atm. The reduced mechanism shows good agreement with the detailed mechanism and experimental data.

Table 4.4: Additional reactions added for NO_x production

	Reaction	A_0 [cm^3/mol-s]	b	E_a [J/mol]
1f.	$O + N_2 \rightarrow NO + N$	7.600E+13	0.0	75460.4
1r.	$NO + N \rightarrow O + N_2$	1.600E+13	0.0	0.0
2f.	$N + O_2 \rightarrow NO + O$	6.400E+09	1.0	6255.27
2r.	$NO + O \rightarrow N + O_2$	1.500E+09	1.0	38723.1
3f.	$N + OH \rightarrow NO + H$	4.100E+13	0.0	0.0
3r.	$NO + H \rightarrow N + OH$	2.000E+14	0.0	46964.17
4.	$N_2O + O \leftrightarrow N_2 + O_2$	1.400E+12	0.0	10810.00
5.	$N_2O + O \leftrightarrow 2NO$	2.900E+13	0.0	23150.00
6.	$N_2O + H \leftrightarrow N_2 + OH$	3.870E+14	0.0	18880.00
7.	$N_2O + OH \leftrightarrow N_2 + HO_2$	2.000E+12	0.0	21060.00
8.	$N_2O + M \leftrightarrow N_2 + O + M$	7.910E+10	0.0	56020.00
	$\hookrightarrow$ Low temp.	6.370E+14	0.0	56640.00
	$\hookrightarrow$ Collision eff.			
	H_2 - 2.0, H_2O - 6.0, CH_4 - 2.0			
	CO - 1.5, CO_2 - 2.0			
9.	$HO_2 + NO \leftrightarrow NO_2 + OH$	2.110E+12	0.0	-480.00
10.	$NO + O + M \leftrightarrow NO_2 + M$	1.060E+20	-1.410	0.0
	$\hookrightarrow$ Collision eff.			
	H_2 - 2.0, H_2O - 6.0, CH_4 - 2.0			
	CO - 1.5, CO_2 - 2.0			
11.	$NO_2 + O \leftrightarrow NO + O_2$	3.900E+12	0.0	-240.00
12.	$NO_2 + H \leftrightarrow NO + OH$	1.320E+14	0.0	360.00

NO_x reactions were added to the skeletal mechanism and an associated 98-species reduced mechanism was developed. The reduced mechanisms provide useful computational speedup compared to the parent skeletal and detailed mechanisms, allowing more computationally-efficient three-dimensional coupled CFD and chemical kinetics simulations of IC engine combustion.

Chapter 5

CONVERGE

CONVERGE (Richards *et al.*, 2013), by Convergent Science, is a three-dimensional computational fluid dynamics program for transient or steady-state flow with complex geometries. Converge can solve chemically-reacting, compressible/incompressible, laminar/turbulent flows with moving boundaries and liquid sprays. The primary use of Converge is for internal combustion (IC) engine simulations. The governing equations are the conservation of mass, momentum, energy, species, and passive scalars. For compressible flows, either the ideal gas or Redlich-Kwong equation of states can be specified. Either finite volume or a combination of finite volume and finite difference methods can be used. The pressure is solved using the Pressure Implicit with Splitting of Operators (PISO) algorithm with a geometric multigrid method or successive over-relaxation (SOR). All quantities are stored at the cell centers and central/upwind interpolation is used to get values at the cell surfaces. Time advancement is achieved using a θ-method with θ between 0.5 (Crank-Nicolson) and 1.0 (implicit). Turbulence models include both Reynolds-Averaged Navier-Stokes (RANS) (k-epsilon, RNG k-epsilon) and Large-Eddy Simulation (LES) (upwinding, Smagorinski, Dynamic Smagorinski, one-equation viscosity model, dynamic structure model, consistent dynamic structure model). Additional details about CONVERGE and the model developed in this work are presented in this chapter.

5.1 Governing equations

The primary governing equations in CONVERGE are the conservation of mass, momentum, and energy. For reactive flow applications, such as IC engine combustion, additional equations for the transport of species and turbulence are needed. This section follows information presented in the CONVERGE Theory Manual (Richards *et al.*, 2013).

Mass and momentum

The compressible formulation of mass and momentum transport are given by Eq. 5.1 and 5.2. The stress tensor, σ_{ij}, is given by Eq. 5.3. In the current work, the source term in Eq. 5.1 arises from evaporation of the liquid fuel spray. Similarly, the source term in Eq. 5.2 comes from spray coupling.

$$\frac{\partial \rho}{\partial t} + \frac{\partial \rho u_i}{\partial x_i} = S \tag{5.1}$$

$$\frac{\partial \rho u_i}{\partial t} + \frac{\partial \rho u_i u_j}{\partial x_j} = -\frac{\partial P}{\partial x_i} + \frac{\sigma_{ij}}{x_j} + S_i \tag{5.2}$$

$$\sigma_{ij} = \mu \left(\frac{\partial u_i}{\partial x_j} + \frac{\partial u_j}{\partial x_i} \right) + \left(\mu' - \frac{2}{3}\mu \right) \left(\frac{\partial u_k}{\partial x_k} \delta_{ij} \right) \tag{5.3}$$

In the above equations, u is velocity, ρ is density, S is the source term, P is the pressure, μ is the viscosity, μ' is the dilatational viscosity (which is set to zero), and δ_{ij} is the Kronecker delta. Because a turbulence model will be used for the simulations in this work, the viscosity μ is replaced by the turbulent viscosity described by Eq. 5.4. Here, C_u is a turbulence model constant, k is the turbulence kinetic energy, and ϵ is the turbulence dissipation rate.

$$\mu_t = \mu + C_u \rho \frac{k^2}{\epsilon} \tag{5.4}$$

Because the momentum transport is solved using the incompressible formulation, an equation of state is required to calculate pressure. The Redlich-Kwong real gas equation of state is used, as described by Eq. 5.5. The first term in parentheses acts as a compressibility factor modifying the ideal gas equation of state, where $\nu_r = (P_c \nu)/(R_u T_c)$ is the reduced specific volume with P_c being the critical pressure and T_c the critical temperature. Additionally, R_u is the gas constant, MM_{mix} is the mixture-averaged molecular mass, and $T_r = T/T_c$ is the reduced temperature. The equation of state is not directly used to solve for pressure, but is used indirectly within the algorithm that solves for pressure to ensure the equation of state is satisfied.

$$P = \left(\frac{\nu_r}{\nu_r - 0.08664} - \frac{0.42748}{(\nu_r + 0.08664) T_r^{3/2}} \right) \rho \left(\frac{R_u}{MM_{mix}} \right) T \tag{5.5}$$

Energy

The compressible form of the energy equation is given in Eq. 5.6, where ρ is the density, D is the mass diffusion coefficient, S is the source term, P is the pressure, e is the specific internal energy, K is the thermal conductivity, h_m is the species enthalpy, σ_{ij} is the stress tensor, and T is the temperature. Additionally, $Y_m = m_m/m_{tot} = \rho_m/\rho_{tot}$ is the mass fraction of species m, where m_m (ρ_m) is the total mass (density) of species m in the cell and m_{tot} (ρ_{tot})

is the total mass (density) in the cell. Because the current work utilizes a turbulence model, the conductivity is replaced by the turbulent conductivity $K_t = K + c_p(\mu_t/Pr_t)$, where c_p is the constant pressure specific heat, μ_t is the turbulent viscosity, and Pr_t is the turbulent Prandtl number ($Pr_t = 0.9$ in this work). The source term in Eq. 5.6 is not used in the current work.

$$\frac{\partial \rho e}{\partial t} + \frac{\partial u_j \rho e}{\partial x_j} = -P\frac{\partial u_j}{\partial x_j} + \sigma_{ij}\frac{\partial u_i}{\partial x_j} + \frac{\partial}{\partial x_j}\left(K\frac{\partial T}{\partial x_j}\right) + \frac{\partial}{\partial x_j}\left(\rho D \sum_m h_m \frac{\partial Y_m}{\partial x_j}\right) + S \tag{5.6}$$

Species

The compressible species transport equation is given in Eq. 5.7, where u is the velocity, ρ is the density, $\rho_m = Y_m\rho$ is the species density, Y_m is the mass fraction of species m, D is the molecular mass diffusion coefficient, and S is the source term. The molecular mass diffusion coefficient is $D = \nu/Sc$, where Sc is the Schmidt number. Since a turbulence model is used in the current work, D is replaced by $D_t = \nu_t/Sc_t$, where Sc_t is the turbulent Schmidt number ($Sc_t = 0.78$ in this work). The source term in Eq. 5.7 accounts for the production/destruction of species through chemical reactions and evaporation of the liquid fuel spray.

$$\frac{\partial \rho_m}{\partial t} + \frac{\partial \rho_m u_j}{\partial x_j} = \frac{\partial}{\partial x_j}\left(\rho D \frac{\partial Y_m}{\partial x_j}\right) + S_m \tag{5.7}$$

Turbulence (RANS)

Reynolds-Averaged Navier-Stokes (RANS) models decompose the instantaneous flow variables into their steady and fluctuating components. For example, the instantaneous velocity (u) can be decomposed into the steady or ensemble mean quantity ($\bar{u}$) and fluctuations (u'), such that $u = \bar{u} + u'$. The RANS equations are derived by applying this decomposition to the Navier-Stokes equations, however, the Reynolds stress term ($\rho\overline{u_i' u_j'}$) appears, representing the effects of turbulence, and must be modeled. This is traditionally accomplished by lumping the Reynolds stress into the viscosity by using a turbulent, or eddy, viscosity in place of the molecular viscosity. Dimensional arguments suggest that the turbulent viscosity (μ_t) can be modeled as $\mu_t = C_\mu \rho(k^2/\epsilon)$, where C_μ is a model constant, k is the turbulence kinetic energy ($k^2 = u_i'^2$ $[m^2/s^2]$), and ϵ $[m^2/s^3]$ is the turbulence dissipation rate.

Given this model for the turbulent viscosity, one popular approach is to use a two-equation model for k and ϵ. Two of these two-equation models are the k-ϵ model and the Re-Normalization Group (RNG) k-ϵ model, which each use transport equations for k and ϵ. The RNG k-ϵ model is an improvement upon the traditional k-ϵ model that attempts to account for the different scales of motion through changes to the production term (Yakhot *et al.*, 1992). The transport equation for k is given by Eq. 5.8 with the stress tensor given by Eq. 5.9. The transport equation for ϵ is given by Eq. 5.10.

Table 5.1: RNG k-ϵ model constants

C_μ	0.0845
$1/Pr_k$	1.39
$1/Pr_\epsilon$	1.39
$c_{\epsilon 1}$	1.42
$c_{\epsilon 2}$	1.68
$c_{\epsilon 3}$	-1.0
β	0.012
η_0	4.38
c_s	0.0

$$\frac{\partial \rho k}{\partial t} + \frac{\partial \rho u_i k}{\partial x_i} = \sigma_{ij}\frac{\partial u_i}{\partial x_j} + \frac{\partial}{\partial x_j}\frac{\mu}{\mathrm{Pr}_k}\frac{\partial k}{\partial x_j} - \rho\epsilon + S \tag{5.8}$$

$$\sigma_{ij} = 2\mu_t S_{ij} - \frac{2}{3}\delta_{ij}\left(\rho k + \mu_t \frac{\partial u_i}{\partial x_i}\right) \tag{5.9}$$

$$\frac{\partial \rho \epsilon}{\partial t} + \frac{\partial \rho u_i \epsilon}{\partial x_i} = \frac{\partial}{\partial x_j}\left(\frac{\mu}{Pr_\epsilon}\frac{\partial \epsilon}{\partial x_j}\right) - c_{\epsilon 3}\rho\epsilon\frac{\partial u_i}{\partial x_i} + \left(c_{\epsilon 1}\frac{\partial u_i}{\partial x_j}\sigma_{ij} - c_{\epsilon 2}\rho\epsilon + c_s S\right)\frac{\epsilon}{k} - \rho R \tag{5.10}$$

In Eq. 5.10, R is depends on the model, $c_{\epsilon 1}$, $c_{\epsilon 2}$, and $c_{\epsilon 3}$ are model constants, and S is a source term. For the standard k-ϵ model, $R = 0$ and for the RNG k-ϵ, R is described by Eq. 5.11 where $\eta = (k/\epsilon)\,|S_{ij}|$. The source terms in Eqs. 5.8 and 5.10 account for the interactions of turbulence with the liquid phase (fuel droplets). The RNG k-ϵ model constants used in this study are summarized in Table 5.1.

$$R = \frac{C_\mu \eta^3 (1 - \eta/\eta_0)}{(1 + \beta\eta^3)}\frac{\epsilon^2}{k} \tag{5.11}$$

5.2 Model of Sandia HCCI engine

Simulations in this work are performed using CONVERGE (Richards *et al.*, 2013) for the Sandia HCCI engine (Dec *et al.*, 2011). CONVERGE employs a cut-cell Cartesian method for grid generation and generates a grid at each time step given the position of the boundary surfaces. The previous time step solution is mapped onto the new grid before solving for the next time step. This procedure naturally permits the use of moving surfaces, such as the piston and intake/exhaust valves. A uniform grid spacing of 2 mm was used, as this was the finest grid resolution that could be afforded.

A schematic of the computational grid is shown in Fig. 5.1 and engine specifications are listed in Table 5.2 (values in parentheses indicate experimental values that differ from the

Table 5.2: Sandia HCCI engine specifications

Displacement	0.981 L
Bore	102 mm
Stroke	120 mm
Connecting rod	192 mm
Geometric compression ratio	13.65:1 (14:1)
Number of valves	4
IVO	360°BTDC
IVC	158°BTDC
EVO	122°ATDC
EVC	368°ATDC
Engine speed	1200 rpm
Intake pressure	1 bar, 2 bar
Coolant temperature	100°C

associated value used in the simulations). The geometric compression ratio (CR) of the computational mesh is 13.65:1, which is slightly lower than the 14:1 used in the experiment in order to match the motored pressure trace as crevices and blow down are not meshed directly.

The engine has two intake ports, one port with a helical geometry and one port with a tangential geometry. The helical geometry promotes in-cylinder swirl, however, an anti-swirl plate is used in in the experiment to counteract this swirl generation. The anti-swirl plate is not included in the computational mesh. The valve lift profiles are set using experimentally measured valve lift values. The piston has a deep central bowl to prevent piston wetting at late direct-injection timings. The head gasket crevice is included in the computational mesh and a piston ring crevice model is used rather than direct meshing of the piston ring crevices. Dimensional information about the piston rings and piston ring cutouts is used as input to the piston ring crevice model.

Simulations are run from 360°BTDC to 90°ATDC. This encompasses the full intake stroke to part way through the expansion, after combustion has completed but before the exhaust valve opens (at 122°ATDC). The intake stroke is computed to account for realistic thermal stratification and in-cylinder velocity profiles in the premixed intake gas. Chemistry is computed only for cells with temperatures in excess of 600 K and is not computed in the intake or exhaust ports while the respective valves are closed. This helps reduce the computational cost of the simulations, as the time computing chemistry accounts for a large fraction of the total computational effort. Nonetheless, the computational cost is still significant, such that a grid resolution study was not performed with finer grids; however, coarsening the grid resolution to 4 mm tended to advance combustion phasing by ~ 2°CA.

The gasoline used in the experiments by Dec et al. considered in this work is RD387 research grade gasoline, which contains wide range of molecular components. Although the broad molecular composition has been quantified (i.e. amount of alkanes, aromatics, and

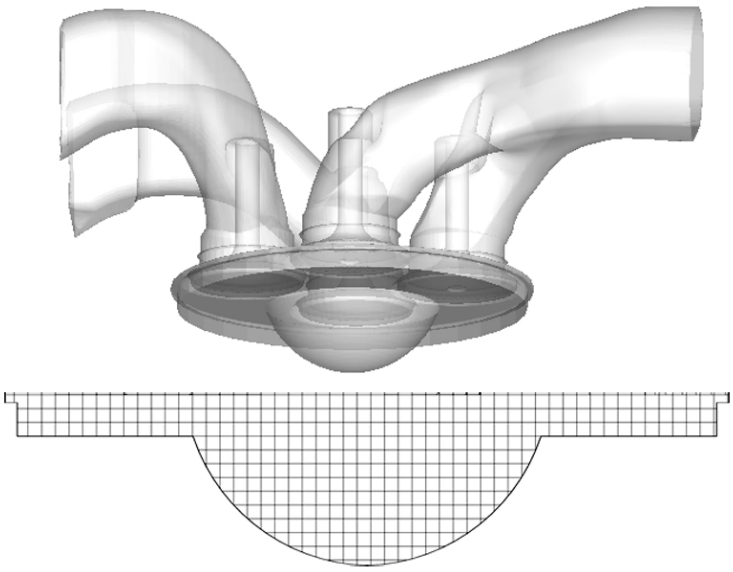

Figure 5.1: Computational surface of Sandia HCCI engine at top dead center. The in-cylinder grid is shown with a grid spacing of 2 mm (the full grid includes the intake and exhaust ports).

olefins), specifying the exact amount of each molecule in RD387 is not feasible. As a result, a surrogate containing a small number of pure components has been formulated by Mehl *et al.* (2011a) to mimic major properties of RD387. The targeted properties are the the broad molecular composition, the H/C ratio, stoichiometric air-fuel ratio, and anti-knock index (AKI). The AKI is the average of the Research Octane Number (RON) and Motor Octane Number (MON). That is, AKI = (RON+MON)/2. The AKI is a metric used to characterize the overall reactivity of a fuel.

In this study, gasoline is modeled by the 4-component surrogate identified by Mehl *et al.* (2011a) comprised of 57% iso-octane (iC_8H_{18}), 16% n-heptane (nC_7H_{16}), 23% toluene ($C_6H_5CH_3$), and 4% 2-pentene (C_5H_{10}–2) by liquid volume. The chemistry is modeled using a 96-species reduced mechanism for the 4-component gasoline surrogate (Wolk and Chen, 2014) and a well-mixed sub-grid chemistry model. A well-mixed sub-grid chemistry model indicates that the reaction rates are evaluated at the mean cell temperature (sub-grid temperature fluctuations are ignored). Because the chemical rates depend on temperature as $e^{1/T}$, sub-grid temperature fluctuations have a non-linear impact on the mean chemical rates (i.e. $\overline{e^{1/T}} \neq e^{1/\bar{T}}$). Despite this shortcoming, a well-mixed sub-grid chemistry is common among RANS engine codes. Turbulence is modeled using the RNG k-ϵ turbulence model (Orszag *et al.*, 1993) discussed in the previous section.

The fuel injector used in the experiment is an 8-hole gasoline direct injection (GDI) injector with a hole size of 125 μm, included angle of 70°, and injection pressure of 120 bar. The injector is centrally mounted in the combustion chamber and oriented vertically

downward. The simulated injection uses a Lagrangian spray model and a stochastic collision model (O'Rourke) with injected droplets following a Rosin-Rammler distribution (Rosin and Rammler, 1933) with a Sauter mean diameter (SMD) of 125 μm, 180 m/s injection velocity, and initial droplet temperature of 300 K. The liquid fuel droplet breakup is modeled using the Kelvin-Helmholtz Rayleigh-Taylor (KHRT) droplet breakup model (Patterson and Reitz, 1998). The KHRT breakup model evaluates the growth rates of the KH and RT instabilities to determine if a droplet breaks up due to one of these mechanisms during a computational time step.

The boundary conditions used for solid surfaces are constant temperature. Surface temperatures are set to the coolant temperature, except for the piston and head, which are set to the experimentally measured head temperature. For the intake ports, the initial and intake inflow compositions are the premixed composition specified. For the in-cylinder region and exhaust ports, the initial composition is the complete combustion products (CO_2, H_2O, O_2, N_2) of the premixed gas (not including additional DI fuel). The initial temperature of the intake region is the intake temperature, and the initial in-cylinder and exhaust temperatures are the experimental exhaust temperature.

5.3 Summary

In this chapter, the governing equations of CONVERGE, the three-dimension CFD and chemical kinetics solver used in this work, are discussed. Additionally, the model developed of the Sandia HCCI/GCI engine is presented.

Chapter 6

Direct-injection fraction span

This chapter discusses simulation results based on experiments from Dec *et al.* (2011) for PFS, a GCI strategy, at a span of direct-injection fractions at constant direct-injection timing at intake pressures of 1 bar and 2 bar. The results of the simulation are analyzed in detail to elucidate the fundamental interactions that are responsible for the experimental observations in Dec *et al.* (2011).

6.1 Intake pressure = 1 bar

Simulations were performed at an intake pressure $P_{in} = 1$ bar for HCCI and PFS engine operation with 18% of the fuel mass direct-injected at 50°BTDC. For the HCCI case, $\phi = 0.458$ and the charge is diluted with 4.0% complete stoichiometric products (CSP), which is simulated exhaust gas recirculation (EGR) of nitrogen (N_2), carbon dioxide (CO_2), and water (H_2O) in proportions that would result from complete stoichiometric combustion of the fuel with air. For PFS, the premixed charge has $\phi = 0.381$ and the average ϕ after fuel injection is $\phi = 0.462$. The PFS charge is diluted with 5.2% CSP. Both cases have a charge mass equivalence ratio (ϕ_m) of $\phi_m = 0.44$, defined as $\phi_m = (F/C)/(F/A)_{stoich}$ where (F/C) is the mass ratio of fuel to total inducted charge gas and $(F/A)_{stoich}$ is the mass ratio of stoichiometric fuel-air mixture for complete combustion (Dec *et al.*, 2011). Adopting ϕ_m simplifies comparison between cases diluted with air versus EGR, as cases with the same ϕ_m have the same fuel energy per unit mass of inducted charge.

The results presented in the rest of this section will be in terms of ϕ including the carbon and hydrogen in CO_2, H_2O, and intermediate species such that ϕ does not decrease as fuel is consumed. The CSP dilution, which has C, H, and O in stoichiometric proportions, increases ϕ for $\phi < 1.0$ and decreases ϕ for $\phi > 1.0$. Using this definition of ϕ is convenient and does not change the interpretation of the results presented in this section as the $\phi = 1.0$ point is preserved. With this definition of ϕ, the HCCI case has $\phi = 0.480$. Similarly, for PFS, the ϕ of the premixed charge is $\phi = 0.413$ and the average ϕ after fuel injection is $\phi = 0.490$. The intake temperature was $T_{in,sim.} = 423$ K for the HCCI simulation and $T_{in,sim.} = 430$ K for

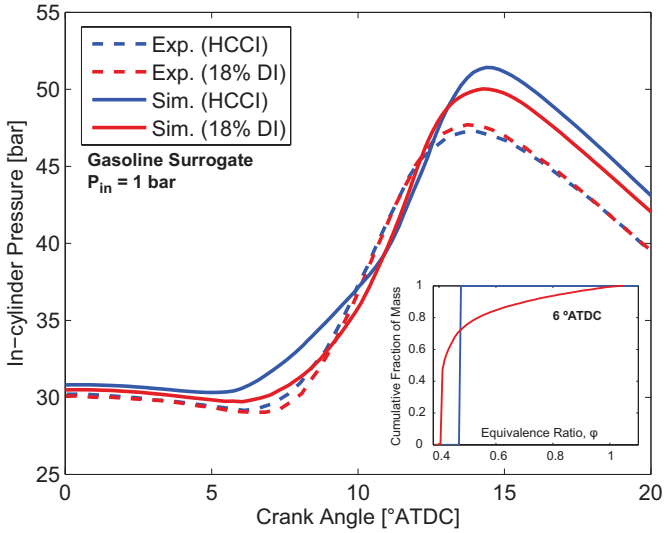

Figure 6.1: In-cylinder pressure as a function of crank angle at $P_{in} = 1$ bar for HCCI, $T_{in,sim.} = 423$ K and PFS with 18% DI, $T_{in,sim.} = 430$ K ($T_{in,exp.} = 416$ K). The cumulative distribution function of in-cylinder mass versus ϕ at 6°ATDC is shown inset.

the PFS simulation, increased from the experimental intake temperature $T_{in,exp.} = 416$ K to match the combustion phasing.

The in-cylinder pressure from the simulation versus crank angle is compared to the experiment in Fig. 6.1. There is reasonable agreement between the simulation and experiment with the simulation slightly over-predicting the peak pressure and pressure during expansion. The cumulative distribution function of in-cylinder mass versus ϕ at 6°ATDC is shown inset in Fig. 6.1 (this crank angle corresponds to in-cylinder contours to be presented later in this section). The HCCI simulation is well-mixed at the ϕ specified. On the other hand, the PFS simulation shows that nearly 50% of the in-cylinder mass is unaffected by the stratification with a smooth distribution of fuel up to about $\phi = 1.0$.

The HRR versus crank angle from the simulation and experiment are compared in Fig. 6.2. There is reasonable agreement between the simulation and experiment with the simulation predicting slightly earlier rise in HRR and a slightly higher peak HRR. The heat released in the simulations is greater than that of the experiment by about 10%, which accounts for the increased peak pressure and the higher in-cylinder pressure during expansion. This may be caused by increased charge mass induction in the simulation compared to the experiment or mis-specification of the O_2 concentration or CSP level. Regardless, the objective of examining the interaction of in-cylinder phenomena is not hindered by this inaccuracy.

Further insight into the sequential auto-ignition process can be gained by evaluating how the temperature and ϕ of each in-cylinder computational cell progress as a function of

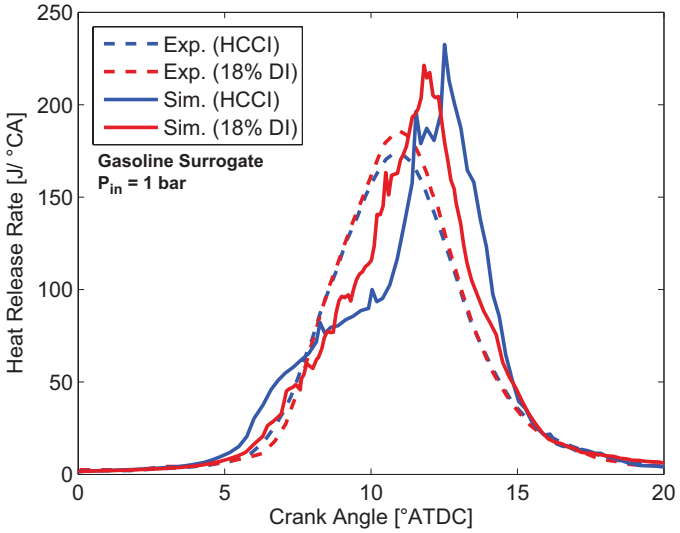

Figure 6.2: HRR as a function of crank angle at $P_{in} = 1$ bar for HCCI, $T_{in,sim.} = 423$ K and PFS with 18% DI, $T_{in,sim.} = 430$ K ($T_{in,exp.} = 416$ K).

crank angle (further analysis is performed only for the PFS case). To accomplish this, the temperature of each in-cylinder computational cell for the PFS case is plotted versus the cell ϕ at selected crank angles in Fig. 6.3. It can be seen in Fig. 6.3 that thermal stratification is evident at about $-10°$ATDC (before any appreciable heat release), with temperature decreasing with increasing ϕ. Temperatures are lower for regions of higher ϕ because an increased amount of energy is required to evaporate and heat the increased fuel mass. At later crank angles, the thermal stratification persists.

The order of ignition depends on both ϕ and temperature, with ϕ closer to $\phi = 1.0$ and higher temperatures generally being more reactive (except for the NTC range for which increasing temperature slows fuel oxidation rates). The tradeoff between increasing ϕ with decreasing temperature results in hot-ignition occurring first in regions with ϕ just above that of the premixed charge.

It can been seen in the last frame (15°CA) of Fig. 6.3 that the peak temperature of the lowest ϕ are near or below 1800 K, which is desired for minimal NO_x production. However, the stratified regions of the charge ($\phi > 0.45$) have burned temperatures above 1800 K, so thermal NO_x production may occur. However, there is relatively little fuel mass at these high flame temperatures. The NO_x production could be estimated using the 98-species version of the reduced chemistry developed in this work.

Although Fig. 6.3 provides a useful visualization of the in-cylinder processes, the process can be more clearly discerned by evaluating the heat release and temperature in the different ϕ regions as a function of crank angle by organizing the in-cylinder grid cells into bins in ϕ space of width 0.10, with the near-premixed ϕ binned in 0.05 increments.

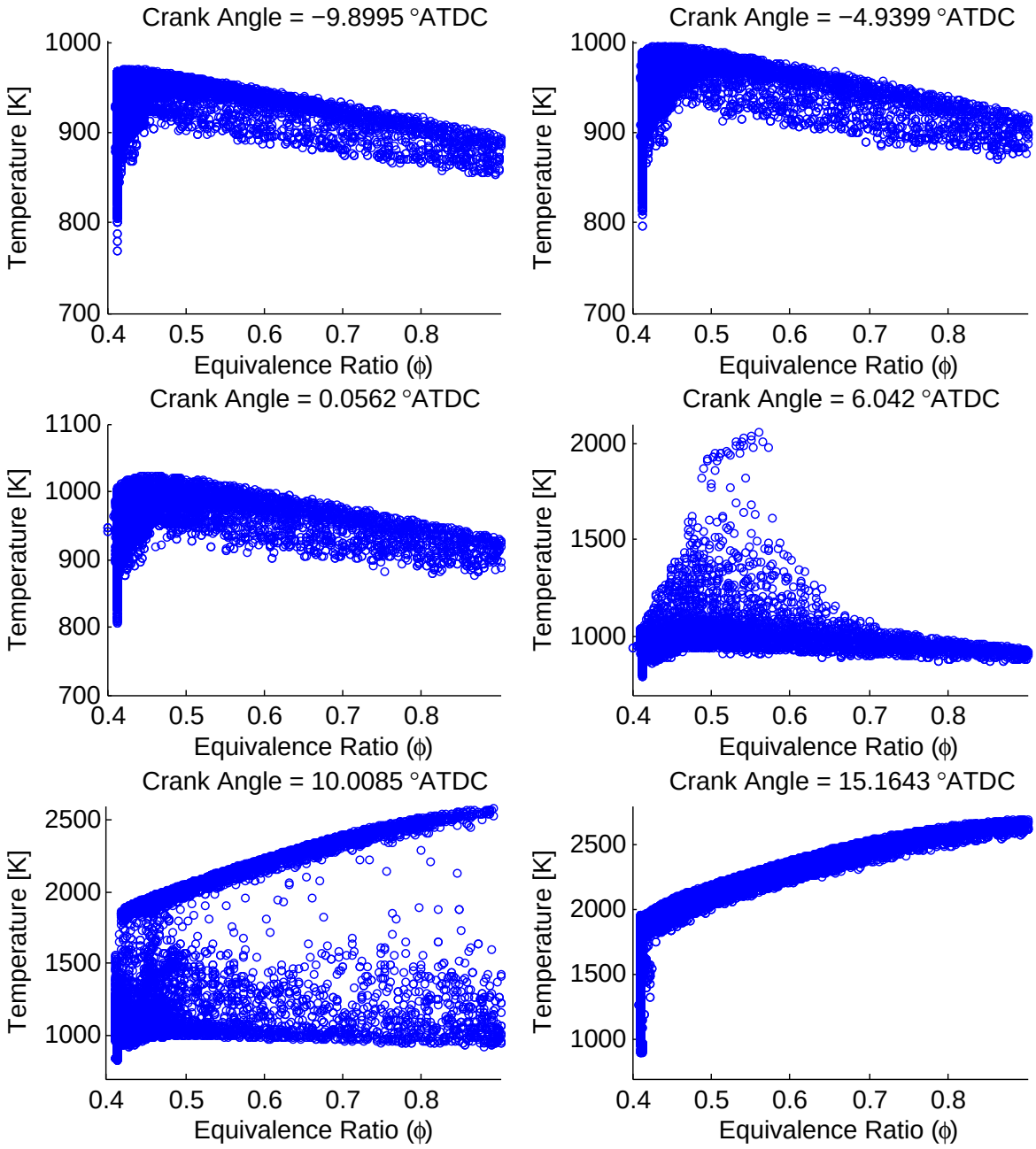

Figure 6.3: Scatter plots of temperature versus ϕ at selected crank angles for PFS with 18% DI, $P_{in} = 1$ bar, $T_{in,sim.} = 430$ K. Thermal stratification is evident at $\sim -10°$ATDC (before any appreciable heat release), with temperature decreasing with increasing ϕ. At later crank angles, this thermal stratification persists. Hot-ignition occurs first in regions with ϕ just above that of the premixed charge.

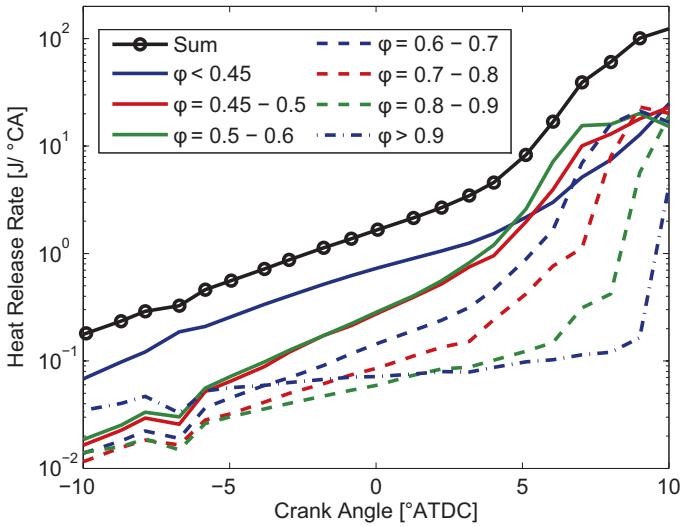

Figure 6.4: Total heat release rate (in J/°CA) for bins of ϕ versus crank angle for PFS with 18% DI, $P_{in} = 1$ bar, $T_{in,sim.} = 430$ K.

The sum of the HRR from each grid cell ($\dot{q}$) (in J/°CA) for each ϕ bin is presented versus crank angle in Fig. 6.4. As seen in Fig. 6.4, the majority of heat release comes from the lean, premixed charge ($\phi < 0.45$) at crank angles before about 5°ATDC with the HRR decreasing for increased ϕ. This is mainly due to decreased mass at higher ϕ. At about 5°ATDC, the regions of the stratified charge with ϕ just above that of the premixed charge auto-ignite ($\phi = 0.45 - 0.5$, $\phi = 0.5 - 0.6$). The stratified regions of the charge then auto-ignite in order of increasing ϕ.

$$HRR_{\phi} = \left. \frac{\sum \dot{q}}{\sum m} \right|_{\phi_{min} < \phi < \phi_{max}} \tag{6.1}$$

In order to evaluate the rate of heat release fairly across ϕ, the HRR for each ϕ bin is divided by the bin mass to obtain the mass specific heat release rate (HRR_{ϕ}) (in J/°CA-g), as defined by Eq. 6.1. The HRR_{ϕ} is presented versus crank angle in Fig. 6.5. At crank angles before about −4°ATDC, HRR_{ϕ} is dominated by mixtures with high ϕ. The HRR_{ϕ} increases more quickly in the lower-ϕ regions compared to higher-ϕ because compression heating increases the temperature of the lower-ϕ regions more quickly due to their higher γ.

Lastly, the mass-weighted temperature for bins of ϕ (T_{ϕ}) is presented versus crank angle in Fig. 6.6. The mass-weighted temperature was determined by dividing the sum of the product of cell mass and temperature by the total bin mass, as described by Eq. 6.2. It can be seen in Fig. 6.6 that the temperature decreases with increased ϕ for the stratified regions of the charge ($\phi > 0.45$) due to evaporative cooling from the liquid fuel spray and decreased compression heating from lower values of γ. The premixed portion of the charge ($\phi < 0.45$)

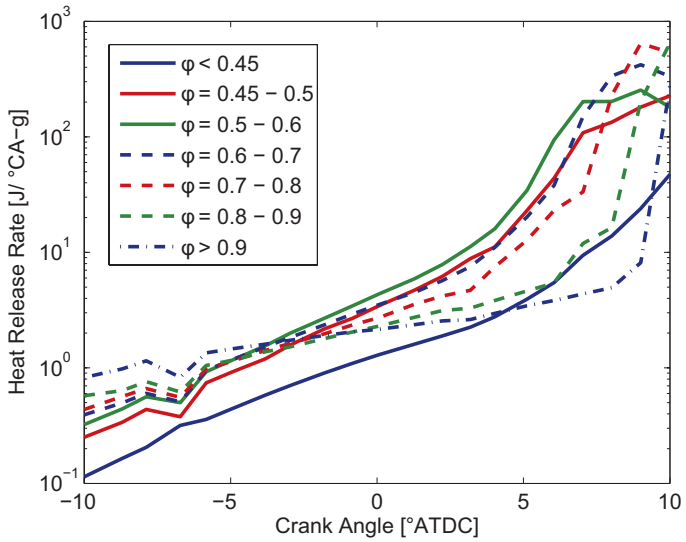

Figure 6.5: Mass-specific HRR (in J/°CA-g) for bins of ϕ versus crank angle for PFS with 18% DI, $P_{in} = 1$ bar, $T_{in,sim.} = 430$ K.

has a lower mass-averaged temperature than $\phi = 0.45 - 0.5$ because it includes cooler near-wall gases. Given this temperature distribution, sequential auto-ignition of the stratified regions of the charge ($\phi > 0.45$) occurs first at low ϕ. It is interesting to note that sequential auto-ignition occurs for $P_{in} = 1$ bar, but that the premixed portion of the charge reaches hot-ignition before the highest-ϕ regions. The difference in hot-ignition timing between first region to reach hot-ignition and the premixed region of the charge ($\phi < 0.5$) is only about 4°CA. As a result, the PRR_{max} is not drastically affected compared to HCCI (Dec *et al.*, 2011).

$$T_\phi = \left.\frac{\sum mT}{\sum m}\right|_{\phi_{min}<\phi<\phi_{max}} \tag{6.2}$$

In-cylinder contours of ϕ and temperature at 6°ATDC are presented in Figs. 6.7 and 6.8, respectively. The simulation time of 6°ATDC was chosen because it is during ITHR, using the HRR derivative criteria of Vuilleumier *et al.* (2014). The circular plane presented in Figs. 6.7 and 6.8 is 4 mm below the cylinder head; the other two views are vertical mid-planes. It can be seen in Fig. 6.7 that the highest ϕ regions are in the piston bowl and that the fuel distribution is asymmetric. A symmetric fuel distribution is not expected here because the full intake stroke was simulated in this work (rather than initializing a swirl profile at intake valve closure), so a non-symmetric velocity field exists in the cylinder at the start-of-injection. Additionally, a stochastic collision model (O'Rourke) was used with the Lagrangian spray model. It can be seen in Fig. 6.8 that the temperature varies significantly and is highest in the moderate-ϕ regions, consistent with Fig. 6.6.

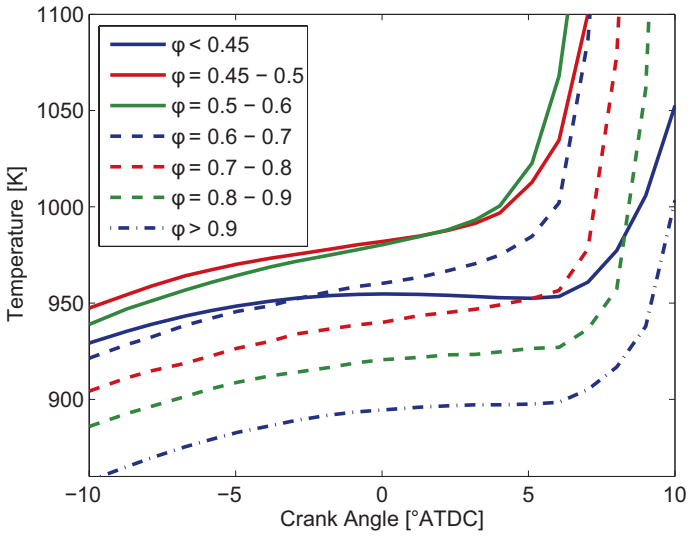

Figure 6.6: Mass-weighted temperature versus crank angle for bins of ϕ versus crank angle for PFS with 18% DI, $P_{in} = 1$ bar, $T_{in,sim.} = 430$ K. Sequential auto-ignition of the stratified regions of the charge occurs first at low ϕ.

6.2 Intake pressure = 2 bar

Simulations were performed for PFS engine operation at $P_{in} = 2$ bar with 3% and 17% of the fuel mass direct-injected at 60°BTDC. For the 3% DI case, the ϕ of the premixed charge is $\phi = 0.570$ and the average ϕ after fuel injection is $\phi = 0.587$. The 3% DI charge is diluted with 24.3% CSP. For the 17% DI case, the ϕ of the premixed charge is $\phi = 0.531$ and the average ϕ after fuel injection is $\phi = 0.642$. The 17% DI charge is diluted with 30% CSP. Both cases have $\phi_m = 0.44$.

As in the previous section, the results will be presented in terms of the ϕ including the carbon and hydrogen in CO_2, H_2O, and intermediate species. Using this definition, for the 3% DI case, the ϕ of the premixed charge is $\phi = 0.673$ and the average ϕ after fuel injection is $\phi = 0.687$. For the 17% DI case, the ϕ of the premixed charge is $\phi = 0.672$ and the average ϕ after fuel injection is $\phi = 0.749$. The intake temperature for both simulations was $T_{in,sim.} = 352$ K, increased from the experimental intake temperature $T_{in,exp.} = 333$ K to match the combustion phasing.

The in-cylinder pressure from the simulation versus crank angle is compared to the experiment in Fig. 6.9. The peak pressure is slightly over predicted in the simulation compared to the experiment and the curvature of the pressure trace is different. The pressure during expansion is better matched for these cases than for the $P_{in} = 1$ bar cases in the previous section. The cumulative distribution function of in-cylinder mass versus ϕ at -5°ATDC is shown inset in Fig. 6.9 (this crank angle corresponds to in-cylinder contours to be presented

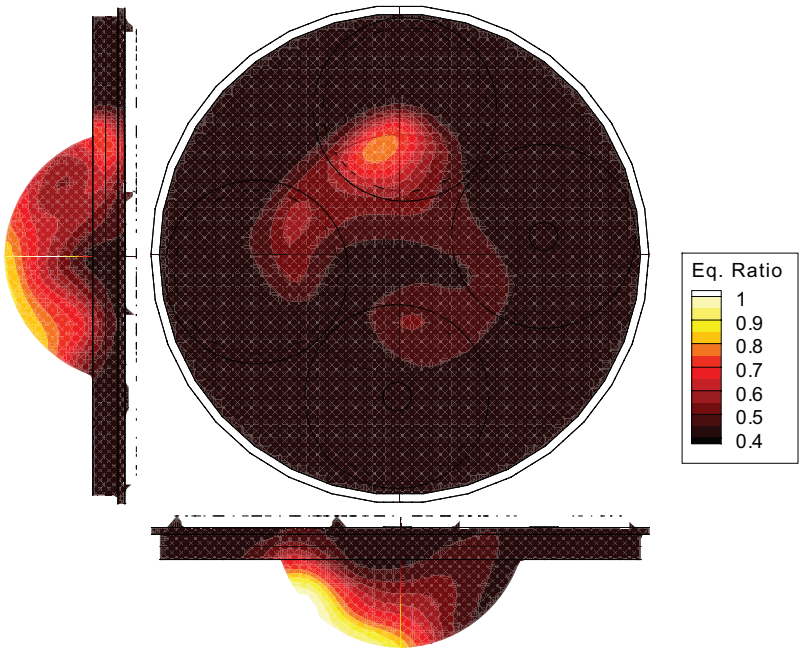

Figure 6.7: Contours of equivalence ratio at 6°ATDC for PFS with 18% DI, $P_{in} = 1$ bar, $T_{in,sim.} = 430$ K. The circular plane is 4 mm below the cylinder head; the other two planes are mid-planes.

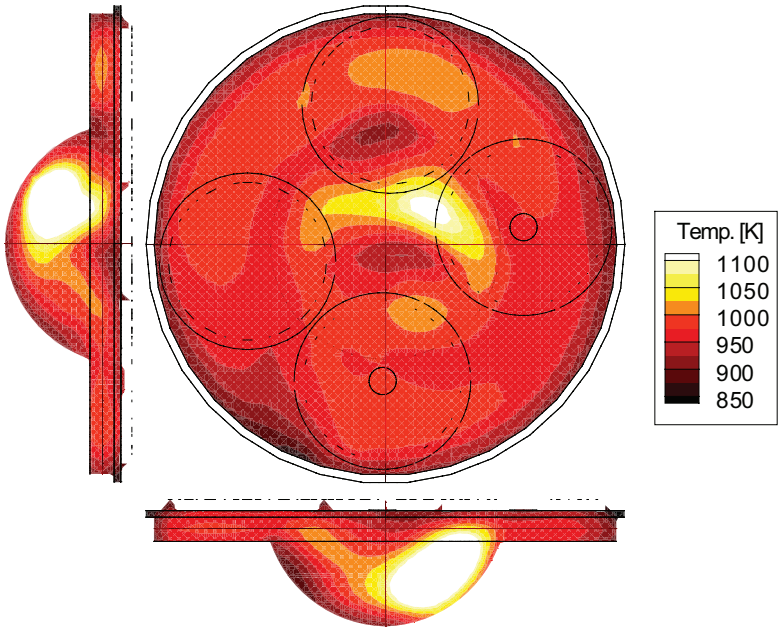

Figure 6.8: Contours of temperature at 6°ATDC for PFS with 18% DI, $P_{in} = 1$ bar, $T_{in,sim.} = 430$ K. The circular plane is 4 mm below the cylinder head; the other two planes are mid-planes.

later in this section). The 17% DI case has a greater extent of stratification, with 15-20% of the in-cylinder above the maximum ϕ in the 3% DI case.

The HRR versus crank angle from the simulation and experiment are compared in Fig. 6.10. The onset of LTHR is predicted well by the simulation, although the magnitude of LTHR is slightly over-predicted. Hot-ignition occurs slightly later in the simulation than experiment and the peak HRR is lower.

Two peaks are observed in Fig. 6.10 because the hot-ignition phasing is sufficiently different between the stratified charge and the lean, premixed charge. If the phasing was slightly closer together, a single peak would be observed. The two-peak structure may be due to limitations of the chemical kinetic model in predicting the auto-ignition of a wide range of ϕ (rich to lean). The two-peak structure is likely not caused by a bi-modal fuel distribution, as smooth fuel distributions are seen in the inset of Fig. 6.9.

The difference between the HRR profiles in Fig. 6.10 could also be due to comparing a single-cycle RANS simulation to ensemble-averaged experimental pressure traces. It was shown for PFS with ethanol in Sjöberg and Dec (2007b) that the ensemble-averaged pressure trace (and the derived HRR and PRR) has a smoother, less bi-modal structure than single-cycle pressure traces. In Sjöberg and Dec (2007b), some single-cycle pressure traces are smooth while others show a two-peak-like structure. A similar observation was made for PRF73 experiments in Yang *et al.* (2011): bi-modal heat release profiles were observed when averaging a selected subset of cycles with combustion phasing within ± 1°CA of the average (> 40% of the total cycles) for sufficiently late injection timing. The ensemble average of all the cycles is smoothed due to cycle-to-cycle variations because the location of each peak changes slightly cycle-to-cycle. The magnitude of cycle-to-cycle variations in Yang *et al.* (2011) are similar to that of Dec *et al.* (2011).

Analysis of 17% DI case

Further insight can be gained by evaluating how the temperature and ϕ of each in-cylinder computational cell progress as a function of crank angle. To accomplish this, the temperature of each in-cylinder computational cell for the PFS case with 17% DI is plotted versus the cell ϕ at selected crank angles in Fig. 6.11. It can be seen in Fig. 6.11 that thermal stratification is present at ~ -10°ATDC (during LTHR), with temperature decreasing with increasing ϕ. At later crank angles, the temperature increases more rapidly at higher ϕ such that all of the stratified regions ($\phi > 0.7$) have approximately the same temperature at TDC. The crank angle range from -10°ATDC to TDC is during LTHR and ITHR, as seen in Fig. 6.10. The temperature of the highest-ϕ regions increases slightly above that of the rest of the charge during ITHR from until about 4°ATDC (see 5°ATDC in Fig. 6.11). Given this ϕ-temperature distribution, hot-ignition occurs first in regions of higher ϕ. Although Fig. 6.11 provides a useful visualization of the in-cylinder processes, the process can be more clearly discerned by evaluating the heat release and temperature in the different ϕ regions as a function of crank angle by organizing the in-cylinder grid cells into bins in ϕ space of width 0.10.

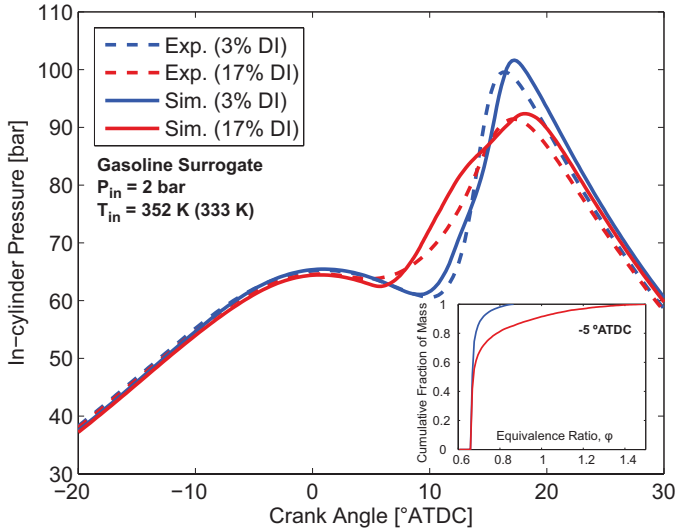

Figure 6.9: In-cylinder pressure as a function of crank angle for PFS at $P_{in} = 2$ bar with 3% and 17% DI, $T_{in,sim.} = 352$ K ($T_{in,exp.} = 333$ K). The cumulative distribution function of in-cylinder mass versus ϕ at $-5°$ATDC is shown inset.

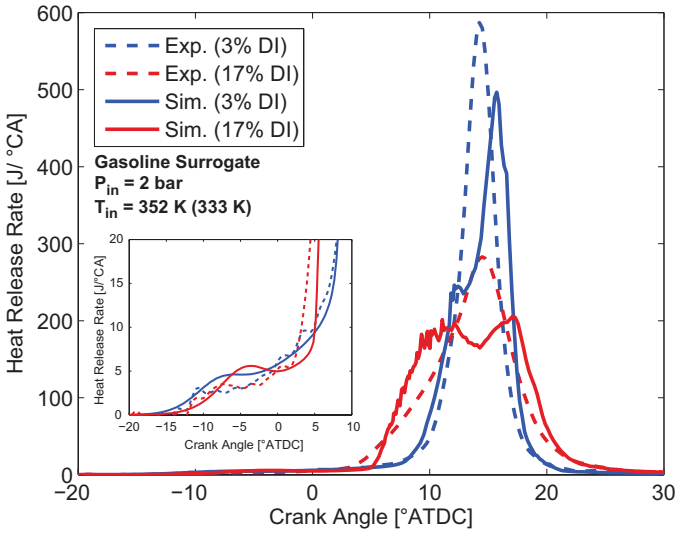

Figure 6.10: HRR as a function of crank angle for PFS at $P_{in} = 2$ bar with 3% and 17% DI, $T_{in,sim.} = 352$ K ($T_{in,exp.} = 333$ K).

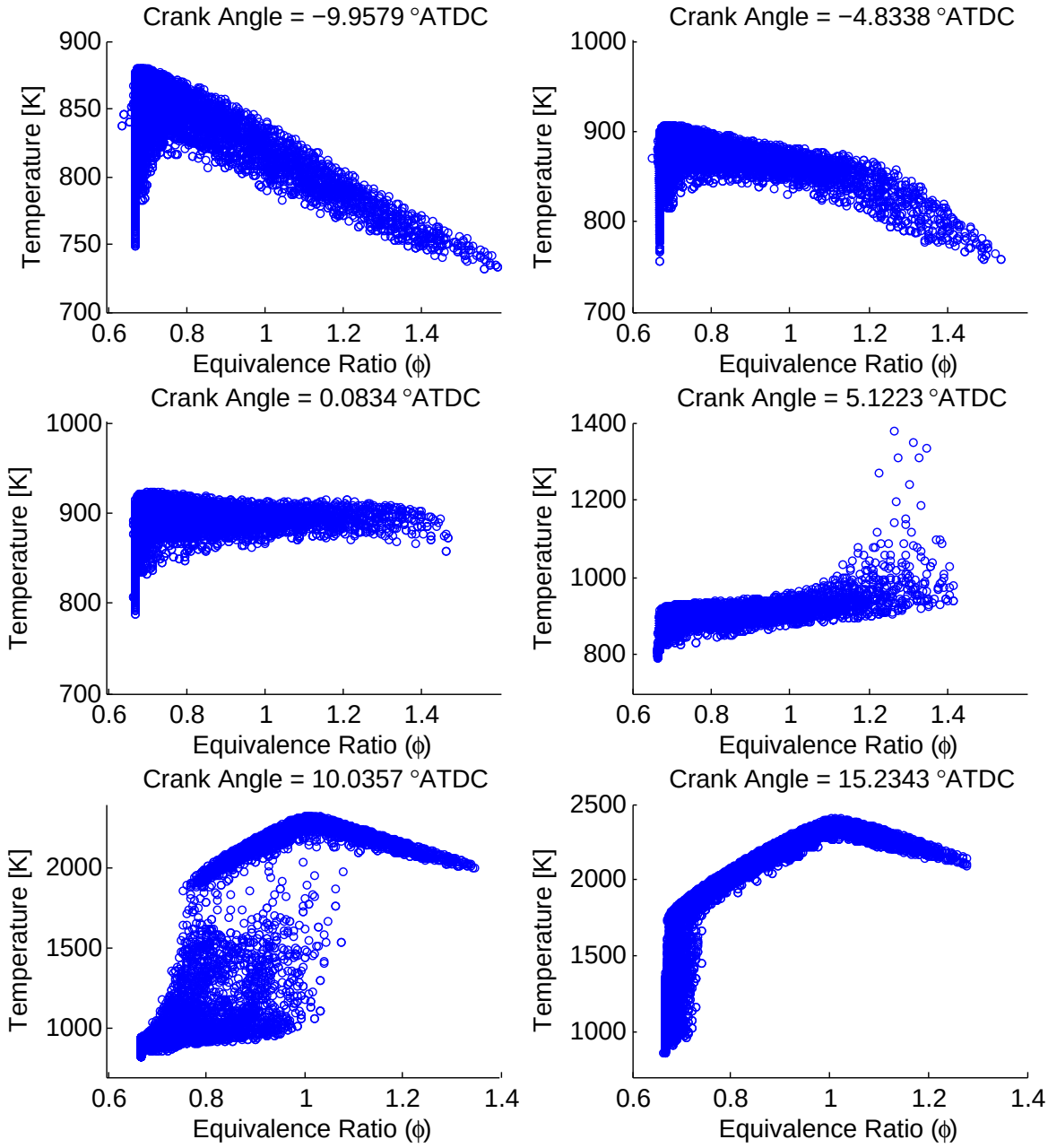

Figure 6.11: Scatter plots of temperature versus ϕ at selected crank angles for PFS with 17% DI, $P_{in} = 2$ bar, $T_{in,sim.} = 352$ K. Thermal stratification is evident at $\sim -10°$ATDC (during LTHR), with temperature decreasing with increasing ϕ. At later crank angles, the temperature increases more rapidly at higher ϕ such that all of the stratified regions ($\phi > 0.7$) have approximately the same temperature at TDC. Hot-ignition occurs first in regions of higher ϕ.

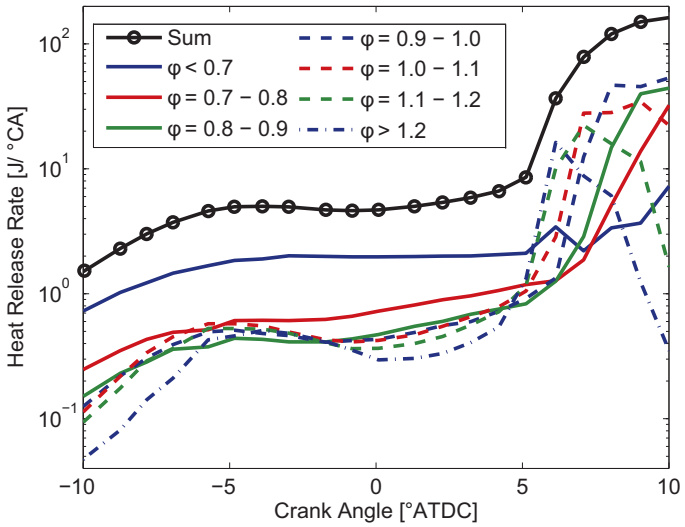

Figure 6.12: Total heat release rate (in J/°CA) for bins of ϕ versus crank angle for PFS with 17% DI, $P_{in} = 2$ bar, $T_{in,sim.} = 352$ K.

The HRR from each ϕ bin of width 0.10 is presented versus crank angle in Fig. 6.12. Before the hot-ignition of the highest ϕ region at about 5°ATDC, the majority of heat release comes from the lean, premixed charge ($\phi < 0.7$). The HRR_ϕ (in J/°CA-g) determined using Eq. 6.1 for each ϕ bin is presented versus crank angle in Fig. 6.13. After about −5°ATDC, HRR_ϕ increases with increasing ϕ and hot-ignition occurs in order of decreasing ϕ. That is, the pre-ignition reactions release heat at a faster rate for higher ϕ and a shorter delay between the pre-ignition reactions and hot-ignition is observed for higher ϕ.

The mass-weighted temperature determined using Eq. 6.2 for bins of ϕ is presented versus crank angle in Fig. 6.14. Before TDC, the temperature decreases with increased ϕ for the stratified regions of the charge ($\phi > 0.7$) due to evaporative cooling from the liquid fuel spray and decreased compression heating from lower values of γ. Again, the premixed portion of the charge ($\phi < 0.7$) has a lower mass-averaged temperature than $\phi = 0.7 - 0.8$ because it includes cooler near-wall gases. The higher rate of heat release from LTHR/ITHR in the higher-ϕ regions increases their temperature more rapidly such that all of the stratified regions ($\phi > 0.7$) have approximately the same temperature at TDC. Given this nearly uniform temperature distribution at TDC, hot-ignition occurs in order of decreasing ϕ. Contrary to $P_{in} = 1$ bar, the premixed charge ($\phi < 0.7$) reaches hot-ignition last, about 9°CA after the first region to auto-ignite ($\phi > 1.3$). This sequential auto-ignition leads to a reduction in PRR_{max} compared to HCCI (Dec *et al.*, 2011).

Increasing pre-ignition heat release with increasing ϕ is the characteristic measured by the ϕ-sensitivity (discussed previously) that correlated with PFS resulting in reductions in PRR_{max}. From these simulations, it is evident that the increased pre-ignition heat release

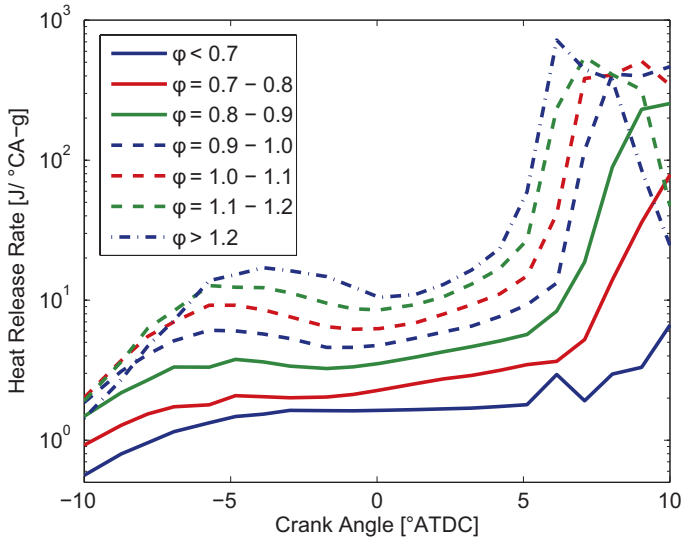

Figure 6.13: Mass-specific HRR (in J/°CA-g) for bins of ϕ versus crank angle for PFS with 17% DI, $P_{in} = 2$ bar, $T_{in,sim.} = 352$ K.

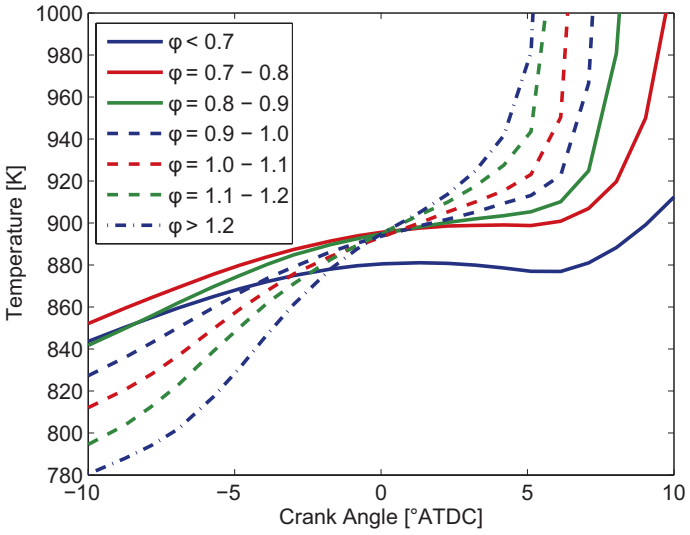

Figure 6.14: Mass-weighted temperature versus crank angle for bins of ϕ for PFS with 17% DI, $P_{in} = 2$ bar, $T_{in,sim.} = 352$ K. The higher HRR in the higher-ϕ regions increases their temperature more rapidly such that all of the stratified regions ($\phi > 0.7$) have approximately the same temperature at TDC. Hot-ignition occurs first in regions of higher ϕ.

with ϕ compensates for the reduced temperature at higher ϕ from evaporative cooling and decreased compression heating, leading to a ϕ-temperature distribution that is favorable for sequential auto-ignition. The increased propensity for LTHR and ITHR for higher ϕ must also be true at lower temperatures, as thermal stratification is evident before any heat release is observed (to be discussed later in this chapter).

In-cylinder contours of ϕ and temperature at 5°BTDC are presented in Figs. 6.15 and 6.16, respectively. The simulation time of 5°BTDC was chosen because it is during ITHR, using the HRR derivative criteria of (Vuilleumier *et al.*, 2014). The circular plane presented in Figs. 6.15 and 6.16 is 4 mm below the cylinder head; the other two views are vertical mid-planes. It can be seen in Fig. 6.15 that the ϕ distribution is axisymmetric and that the highest ϕ regions occur in the piston bowl and at the edge of the piston bowl near the cylinder head. It can be seen in Fig. 6.16 that the temperature is more uniform than for $P_{in} = 1$ bar except for the highest ϕ regions, consistent with Fig. 6.14.

Analysis of 3% DI case

Similar to the previous section, further insight can be gained by evaluating how the temperature and ϕ of each in-cylinder computational cell progress as a function of crank angle. To accomplish this, the temperature of each in-cylinder computational cell for the PFS case with 3% DI is plotted versus the cell ϕ at selected crank angles in Fig. 6.17. It can be seen in Fig. 6.17 that there is thermal stratification at about -10°ATDC, with higher-ϕ regions having lower temperatures due to evaporative cooling from the liquid spray and decreased compression heating from lower values of γ. As TDC is approached, increased LTHR with increasing ϕ lessens the thermal stratification, however, the lower-ϕ regions remain at slightly higher temperatures. This leads to hot-ignition occurring first in the premixed part of the charge and at ϕ just above that of the premixed charge. Hot ignition occurs completely in the higher-ϕ regions of the charge during the extended ignition of the premixed mass. That is, no unburned high-ϕ points remain at 15°ATDC but there is still unburned fuel mass at lower ϕ. The peak ϕ just before hot-ignition is about 0.85. Although Fig. 6.17 provides a useful visualization of the in-cylinder processes, the process can be more clearly discerned by evaluating the heat release and temperature in the different ϕ regions as a function of crank angle by organizing the in-cylinder grid cells into bins in ϕ space of width 0.05.

The HRR from each ϕ bin of width 0.05 is presented versus crank angle in Fig. 6.18. Fig 6.18 shows that the majority of heat release occurs in the premixed regions of the charge ($\phi < 0.70$) at all crank angles, which is expected as only 3% of the fuel mass is direct-injected. Interestingly, hot-ignition occurs in order of increasing ϕ, contrary to observations for the 17% DI case. The peak HRR decreases with increasing ϕ as there is less in-cylinder mass at higher ϕ. Because the total HRR from each bin is influenced by the bin mass, the mass-specific heat release rate, HRR_ϕ, more fairly compares the relative reactivity of each bin.

HRR_ϕ is presented versus crank angle in Fig. 6.19. It can be seen in Fig 6.19 that the LTHR rate is higher for increased ϕ, at crank angles before about -5°ATDC. Fig 6.19 also

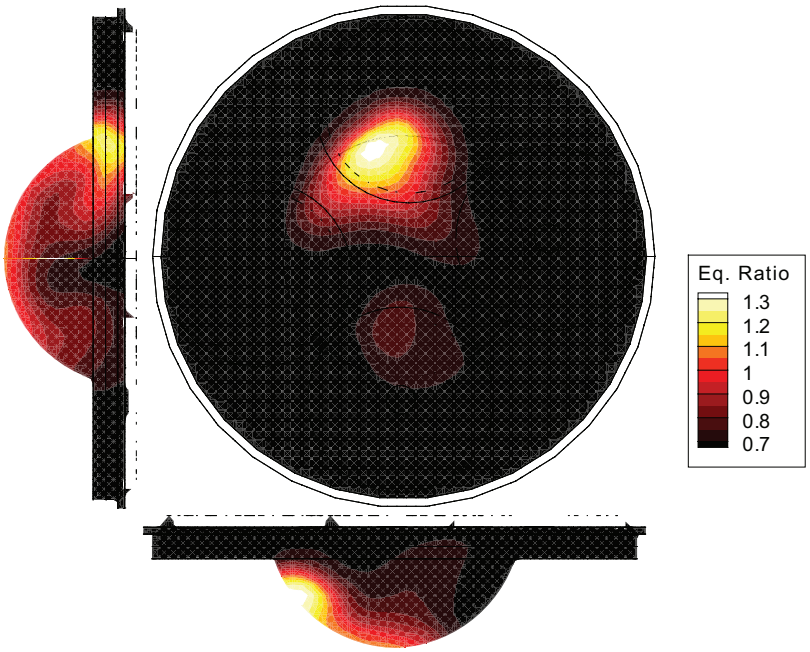

Figure 6.15: Contours of equivalence ratio at 5°BTDC for PFS with 17% DI, P_{in} = 2 bar, $T_{in,sim.}$ = 352 K. The circular plane is 4 mm below the cylinder head; the other two planes are mid-planes.

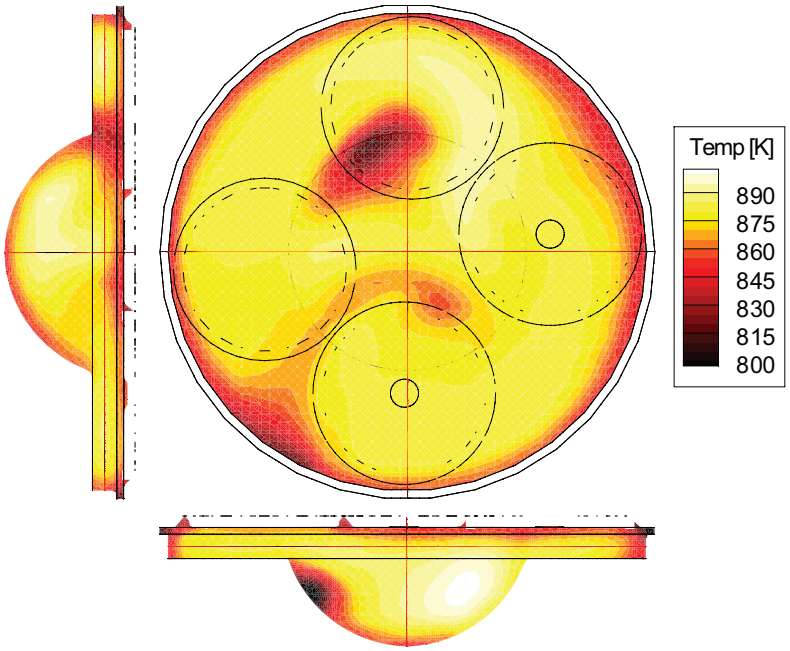

Figure 6.16: Contours of temperature at 5°BTDC for PFS with 17% DI, P_{in} = 2 bar, $T_{in,sim.}$ = 352 K. The circular plane is 4 mm below the cylinder head; the other two planes are mid-planes.

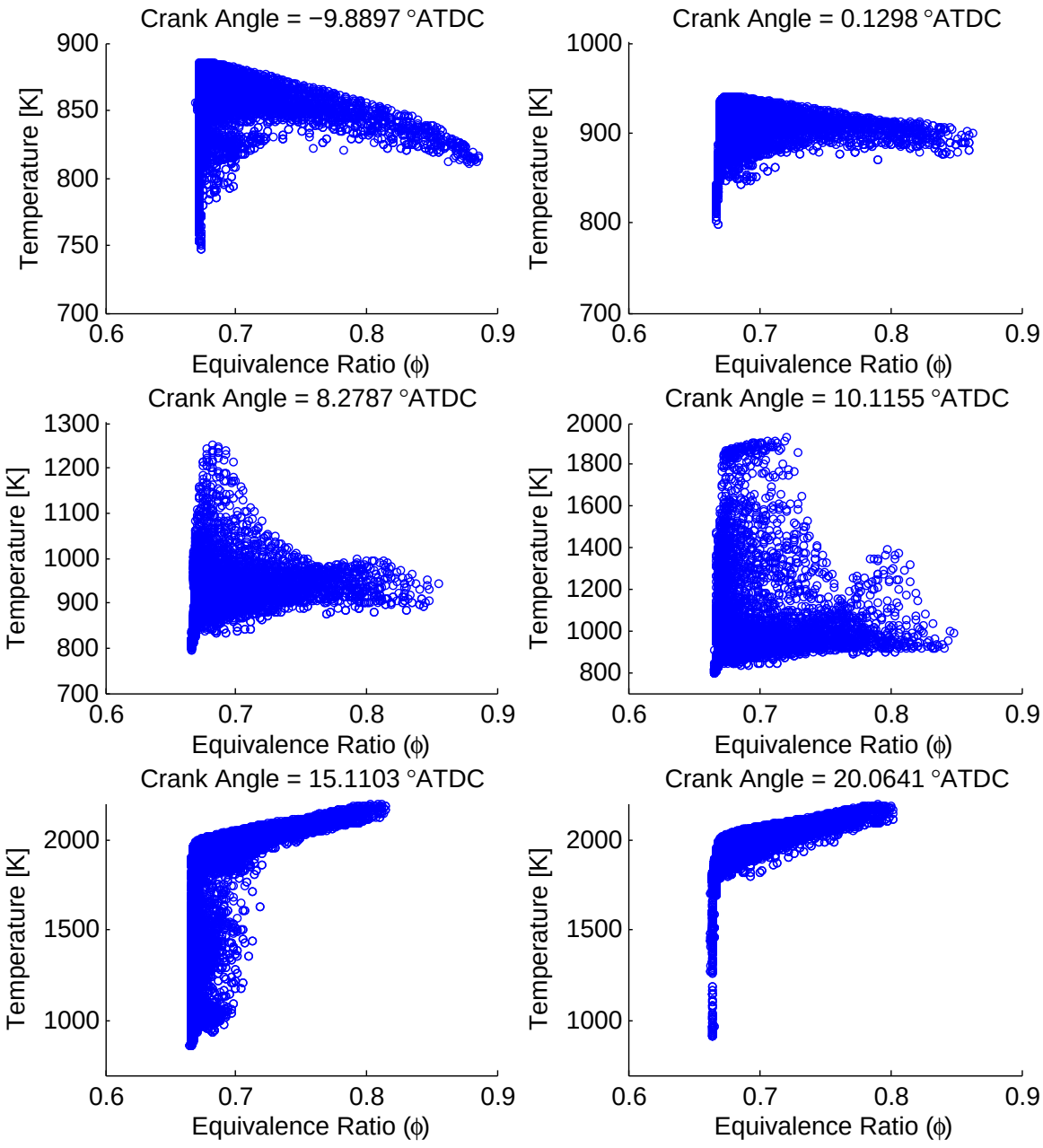

Figure 6.17: Scatter plots of temperature versus ϕ at selected crank angles for PFS with 3% DI, $P_{in} = 2$ bar, $T_{in,sim.} = 352$ K.

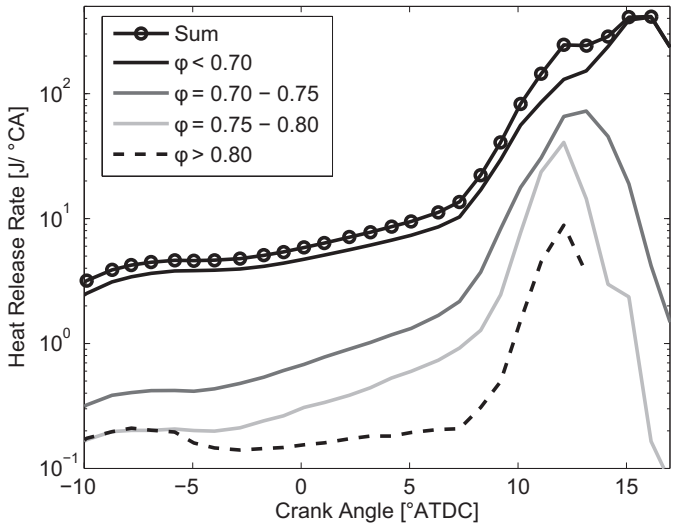

Figure 6.18: Total heat release rate (in J/°CA) for bins of ϕ versus crank angle for PFS with 3% DI, $P_{in} = 2$ bar, $T_{in,sim.} = 352$ K.

suggests that the hot-ignition of the stratified regions of the charge ($\phi > 0.70$) occur at approximately the same time, but still in order of increasing ϕ. The premixed region of the charge ($\phi < 0.70$) appears to ignite later than the stratified region of the charge, but this is convoluted by the extended ignition process from the large amount of in-cylinder mass in this bin that is at different temperatures. In other words, the colder cells in this bin have not reached hot-ignition at the time that the slightly higher temperature regions have. Because the colder regions have much lower HRRs, the bin mass-specific HRR is lowered. This line of reasoning is corroborated by Fig. 6.17.

The mass-weighted temperature (T_ϕ) of each bin versus crank angle is presented in Fig. 6.20. At -10°ATDC, the temperature of the stratified charge decreases with increasing ϕ and the premixed portion of the charge ($\phi < 0.70$) has about the same temperature as the bins of $\phi = 0.70-0.75$ and $\phi = 0.75-0.80$. Approaching TDC, the increased LTHR for higher ϕ leads to greater temperature increases of the higher-ϕ regions compared to the premixed charge ($\phi < 0.70$), with $\phi > 0.80$ remaining at a lower temperature than $\phi = 0.70 - 0.75$ and $\phi = 0.75 - 0.80$. The rapid temperature rise characteristic of hot-ignition occurs at about the same time for the three bins representing the stratified regions of the charge ($\phi > 0.70$), with the mass-weighted temperature of the premixed portion of the charge ($\phi < 0.70$) increasing rapidly a few °CA later. Similar to the explanation for HRR_ϕ, the mass-weighted temperature is held lower by the lower temperature regions of $\phi < 0.70$. Although some of the $\phi < 0.70$ regions are at the flame temperature at 10°ATDC, the unburned cells reduced T_ϕ plotted in Fig. 6.20.

In short, the large amount of fuel mass in the premixed region ($\phi < 0.70$) undergoes

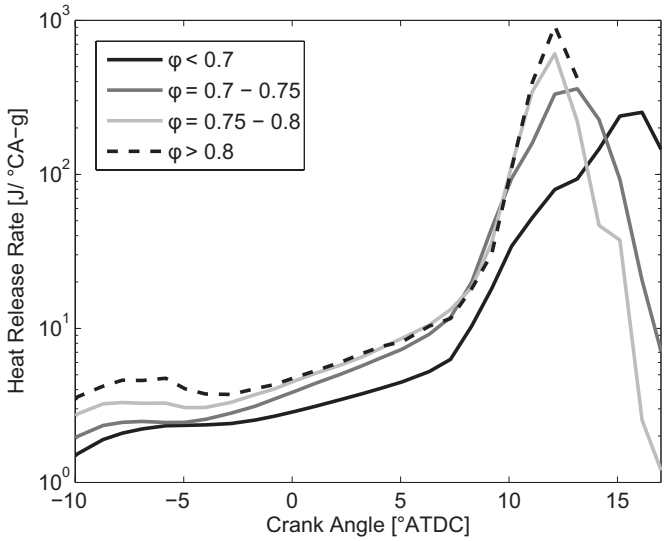

Figure 6.19: Mass-specific HRR (in J/°CA-g) for bins of ϕ versus crank angle for PFS with 3% DI, $P_{in} = 2$ bar, $T_{in,sim.} = 352$ K.

a distributed ignition based on the thermal stratification within that ϕ range. During this process, the stratified regions of the charge ($\phi > 0.70$) completely ignite.

In-cylinder contours of ϕ and temperature at 5°BTDC are presented in Figs. 6.21 and 6.22, respectively. The simulation time of 5°BTDC was chosen because it is during ITHR, using the HRR derivative criteria of Vuilleumier *et al.* (2014). The circular plane presented in Figs. 6.21 and 6.22 is 4 mm below the cylinder head; the other two views are vertical mid-planes. It can be seen in Fig. 6.21 that the ϕ distribution is axisymmetric and that the highest ϕ regions occur in the piston bowl and at the edge of the piston bowl and near the cylinder head. It can be seen in Fig. 6.22 that the temperature is less uniform than the 17% DI case. The highest ϕ regions have corresponding lower temperatures at this crank angle, consistent with Fig. 6.20.

6.3 Temperature dependence of HRR

The temperature dependence of HRR elucidates the difference heat release characteristics between the $P_{in} = 1$ bar and $P_{in} = 2$ bar cases. Fig. 6.23 compares the HRR as a function of in-cylinder temperature for the four cases presented in this section. It can be seen in Fig. 6.23 that hot ignition begins at higher temperatures for $P_{in} = 1$ bar than for $P_{in} = 2$ bar and that higher peak temperatures occur for the $P_{in} = 1$ bar cases. Additionally, hot ignition occurs at about the same temperature for the two cases at each intake pressure.

Because of the importance of LTHR/ITHR in altering the temperature distribution of the mixture stratification prior to hot-ignition, the LTHR/ITHR region is highlighted in

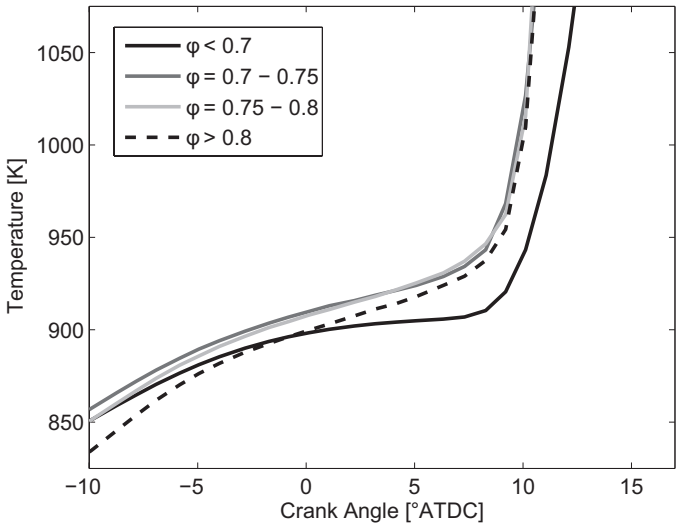

Figure 6.20: Mass-weighted temperature versus crank angle for bins of ϕ for PFS with 3% DI, $P_{in} = 2$ bar, $T_{in,sim.} = 352$ K.

Fig. 6.24. The $P_{in} = 1$ bar cases have very little heat release until the mixture temperature exceeds about 950 K. On the other hand, the $P_{in} = 2$ bar cases show the start of LTHR at about 800 K with a peak LTHR rate occurring at about 870 K. ITHR occurs after LTHR and before hot-ignition, which corresponds to temperatures below about 900 K for these cases.

Although it appears that the increased stratification for the 17% DI case compared to the 3% DI case at $P_{in} = 2$ bar does not change the temperature range during which LTHR occurs, the LTHR in Fig. 6.24 is dominated by the lean, premixed charge which accounts for the majority of the fuel mass and has nearly the same ϕ between the two cases. To illustrate how the temperature range of LTHR varies with ϕ, HRR_ϕ as a function of T_ϕ is presented in Fig 6.25 for the 17% DI case at $P_{in} = 2$ bar. It can be seen in Fig 6.25 that the LTHR range occurs at lower temperatures with increasing ϕ and that peak LTHR rates are higher for larger ϕ. The lower temperature requirement to reach LTHR and the increased amount of heat released during LTHR for increased ϕ lead to the stratified regions of the charge having approximately the same temperature near TDC, as observed in Figs. 6.11 and 6.14. These are two key enabling phenomena for sequential auto-ignition to occur for PFS at $P_{in} = 2$ bar.

6.4 Summary

In this chapter, simulations of Partial Fuel Stratification (PFS), a strategy for reducing the maximum pressure rise rate in compression-ignition engines using fuel stratification, have

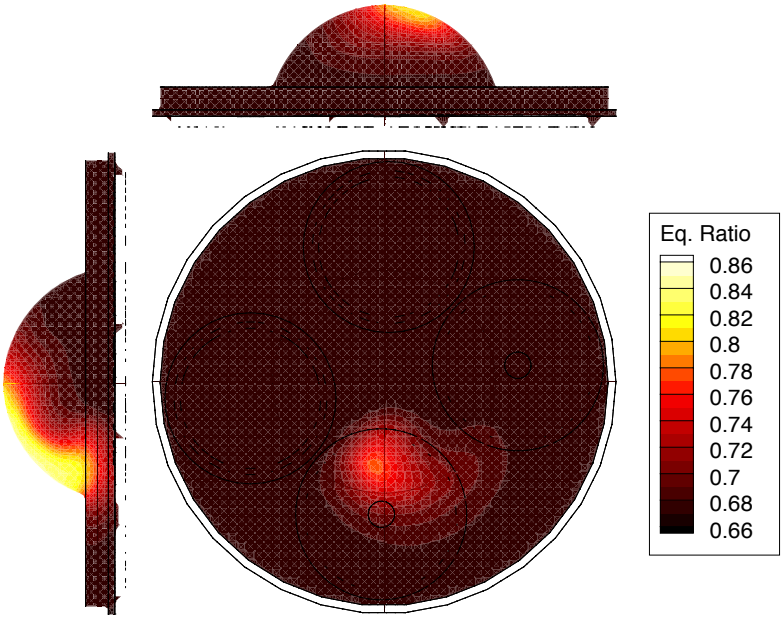

Figure 6.21: Contours of equivalence ratio at 5°BTDC for PFS with 3% DI, P_{in} = 2 bar, $T_{in,sim.}$ = 352 K. The circular plane is 4 mm below the cylinder head; the other two planes are mid-planes.

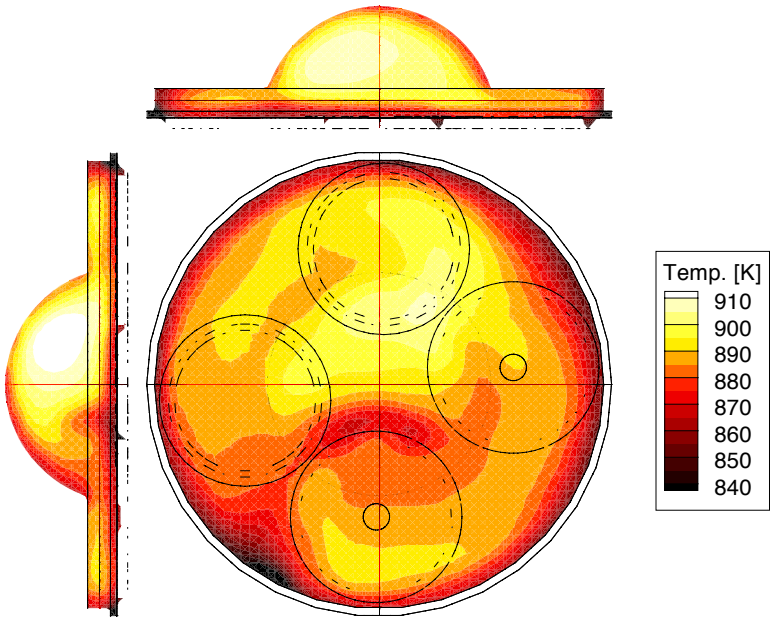

Figure 6.22: Contours of temperature at 5°BTDC for PFS with 3% DI, P_{in} = 2 bar, $T_{in,sim.}$ = 352 K. The circular plane is 4 mm below the cylinder head; the other two planes are mid-planes.

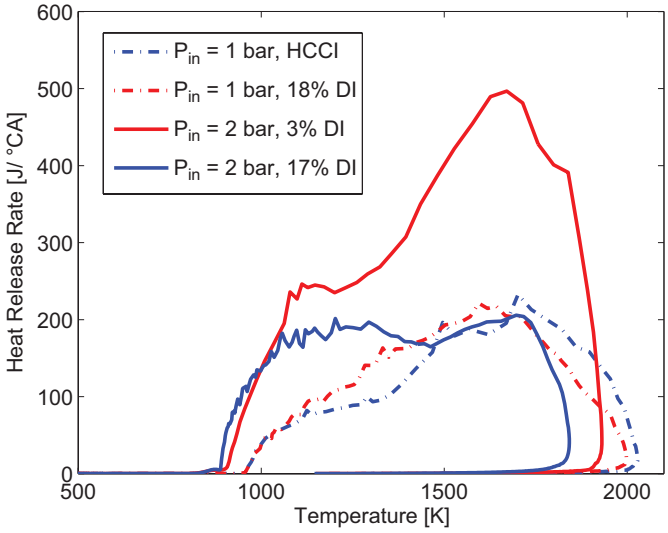

Figure 6.23: HRR as a function of temperature for PFS at $P_{in} = 1$ bar for HCCI, $T_{in,sim.} = 423$ K and PFS with 18% DI, $T_{in,sim.} = 430$ K ($T_{in,exp.} = 416$ K) and $P_{in} = 2$ bar with 3% and 17% DI, $T_{in,sim.} = 352$ K ($T_{in,exp.} = 333$ K).

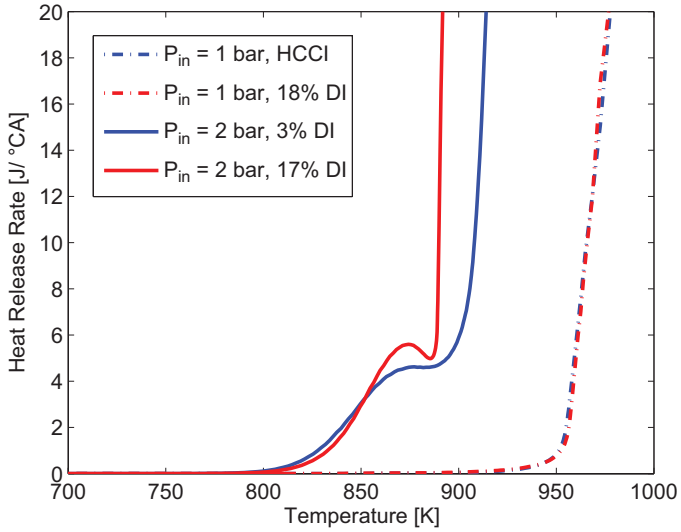

Figure 6.24: HRR as a function of temperature for PFS at $P_{in} = 1$ bar for HCCI, $T_{in,sim.} = 423$ K and PFS with 18% DI, $T_{in,sim.} = 430$ K ($T_{in,exp.} = 416$ K) and $P_{in} = 2$ bar with 3% and 17% DI, $T_{in,sim.} = 352$ K ($T_{in,exp.} = 333$ K). At $P_{in} = 1$ bar, single-stage ignition is clearly evident as is the absence of pre-ignition heat release.

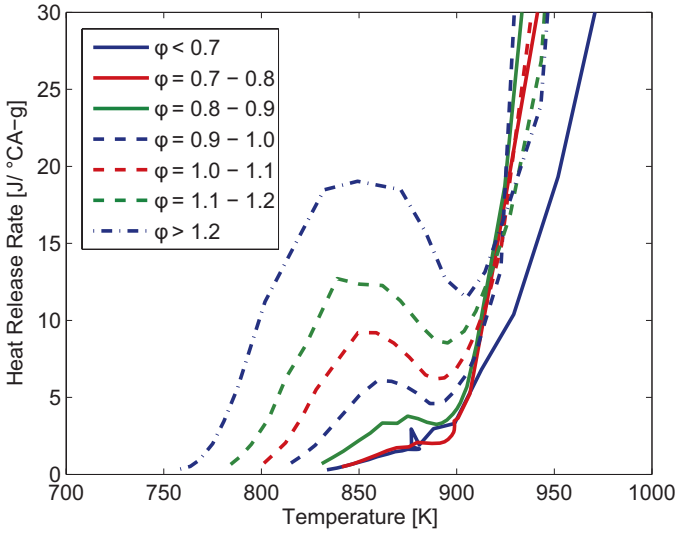

Figure 6.25: HRR as a function of T_ϕ for PFS with 17% DI, $T_{in,sim.} = 352$ K ($T_{in,exp.} = 333$ K), and $P_{in} = 2$ bar. The higher-ϕ regions exhibit LTHR at lower temperatures and higher peak LTHR rates.

been performed using CONVERGE with a 96-species reduced mechanism for a 4-component gasoline surrogate. Comparison is made between simulation results and experiments from the Sandia HCCI/GCI engine at a compression ratio of 14:1. Detailed analysis of the heat release from and temperature of each equivalence ratio region is performed to elucidate the underlying physical processes that contribute to the different behavior of PFS for gasoline at 1 bar and 2 bar intake pressure. The major findings of the section are:

- For 1 bar intake pressure, sequential auto-ignition of the stratified charge (excluding the premixed portion of the charge) occurs in order of increasing ϕ because the temperature is higher for lower ϕ due to lesser influence of evaporative cooling and increased compression heating from the higher ratio of specific heats. The premixed portion of the charge auto-ignites before the highest-ϕ regions. The sequential auto-ignition occurs too fast for useful reduction of the maximum pressure rise rate compared to HCCI.

- For 2 bar intake pressure, sequential auto-ignition of the stratified charge occurs in order of decreasing ϕ because the increased LTHR/ITHR for higher ϕ compensates for evaporative cooling and decreased compression heating from the lower ratio of specific heats such that all stratified regions having approximately the same temperature at TDC. As such, the premixed portion of the charge auto-ignites last, after the higher-ϕ regions. The sequential auto-ignition occurs over a longer time period than at 1

bar intake pressure such that a sizeable reduction in the maximum pressure rise rate compared to HCCI can be achieved.

Chapter 7

Direct-injection timing span

This chapter discusses simulation results based on experiments from Dec *et al.* (2011) for PFS, a GCI strategy, at a span of direct-injection timings at constant direct-injection fraction at an intake pressure 2 bar. The results of the simulation are analyzed in detail to elucidate the fundamental interactions that are responsible for the experimental observations in Dec *et al.* (2011).

7.1 Intake pressure = 2 bar

Simulations were performed for HCCI, or fully-premixed (PM), and PFS engine operation at $P_{in} = 2$ bar with 13% of the fuel mass direct-injected at $-160°$ATDC, $-75°$ATDC, and $-60°$ATDC. All cases have $\phi_m = 0.44$. For the HCCI case, $\phi = 0.591$ and the charge is diluted with 26.6% complete stoichiometric products (CSP), which is simulated exhaust gas recirculation (EGR) of nitrogen (N_2), carbon dioxide (CO_2), and water (H_2O) in proportions that would result from complete stoichiometric combustion of the fuel with air. For the SOI $= -160°$ATDC case, the ϕ of the premixed charge is $\phi = 0.515$ and the average ϕ after fuel injection is $\phi = 0.592$, diluted with 27.0% CSP. For the SOI $= -75°$ATDC case, the ϕ of the premixed charge is $\phi = 0.513$ and the average ϕ after fuel injection is $\phi = 0.589$, diluted with 26.8% CSP. For the SOI $= -60°$ATDC case, the ϕ of the premixed charge is $\phi = 0.535$ and the average ϕ after fuel injection is $\phi = 0.615$, diluted with 29.7% CSP. The SOI $= -60°$ATDC case has a slightly higher CSP level than the other cases to compensate for the increased mixture reactivity from the increased stratification. That is, increased CSP is necessary to delay the combustion phasing to the desired timing. The increased CSP level, while keeping ϕ_m constant, results in a slightly higher air-based ϕ for SOI $= -60°$ATDC than the other cases.

The results presented in the rest of this section will be in terms of ϕ including the carbon and hydrogen in CO_2, H_2O, and intermediate species such that ϕ does not decrease as fuel is consumed. With this definition, the HCCI case has $\phi = 0.703$. Similarly, for PFS with SOI $= -160°$ATDC, the ϕ of the premixed charge is $\phi = 0.649$ and the average ϕ after

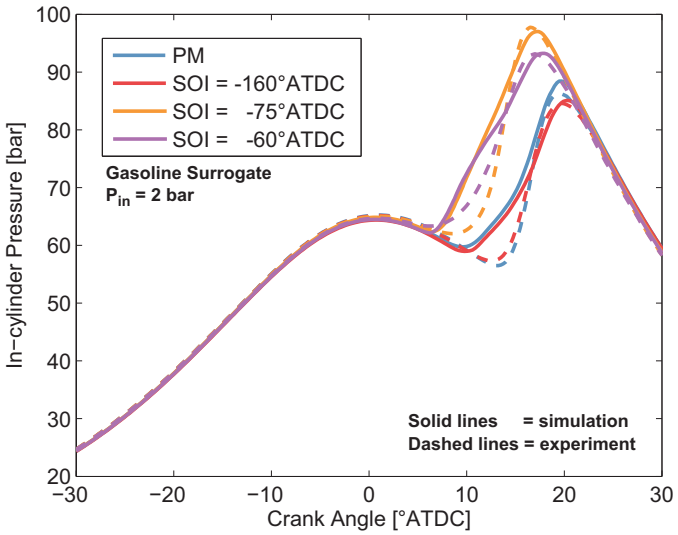

Figure 7.1: In-cylinder pressure as a function of crank angle at $P_{in} = 2$ bar for fully-premixed (PM), and PFS with 13% DI and SOI = -160°ATDC, -75°ATDC, -60°ATDC.

fuel injection is $\phi = 0.705$. For PFS with SOI $= -75°$ATDC, the ϕ of the premixed charge is $\phi = 0.646$ and the average ϕ after fuel injection is $\phi = 0.701$. For PFS with SOI $= -60°$ATDC, the ϕ of the premixed charge is $\phi = 0.675$ and the average ϕ after fuel injection is $\phi = 0.731$.

The intake temperature was $T_{in,sim.} = 377$ K for the HCCI simulation, $T_{in,sim.} = 372$ K for the PFS simulation with SOI $= -160°$ATDC, $T_{in,sim.} = 379$ K for the PFS simulation with SOI $= -75°$ATDC, and $T_{in,sim.} = 374$ K for the PFS simulation with SOI $= -60°$ATDC. These temperatures were increased from the experimental intake temperature $T_{in,exp.} = 333$ K to match the combustion phasing and peak pressure for each case. In the experiment, the combustion phasing is delayed for the HCCI and SOI $= -160°$ATDC cases compared to the SOI $= -75°$ATDC and SOI $= -60°$ATDC cases to keep the ringing intensity below a specific threshold as the combustion is more rapid for the more premixed cases.

The in-cylinder pressure from the simulation versus crank angle is compared to the experiment for all cases in Fig. 7.1. Overall, there is reasonable agreement between the simulations and experiment. The simulations generally predict a slightly too early pressure rise, but reasonably match the peak pressure from the experiment. The pressure during expansion is also matched well.

The HRR from the simulation versus crank angle is compared to the experiment for the HCCI and SOI $= -160°$ATDC cases in Fig. 7.2. The simulation shows a wider HRR profile and lower peak HRR, but captures the LTHR region (inset) well. The simulation shows a rise in HRR at about 10°ATDC, a few °CA before the experiment. This first bump may be caused by thermal stratification in the premixed region of the charge, with the higher

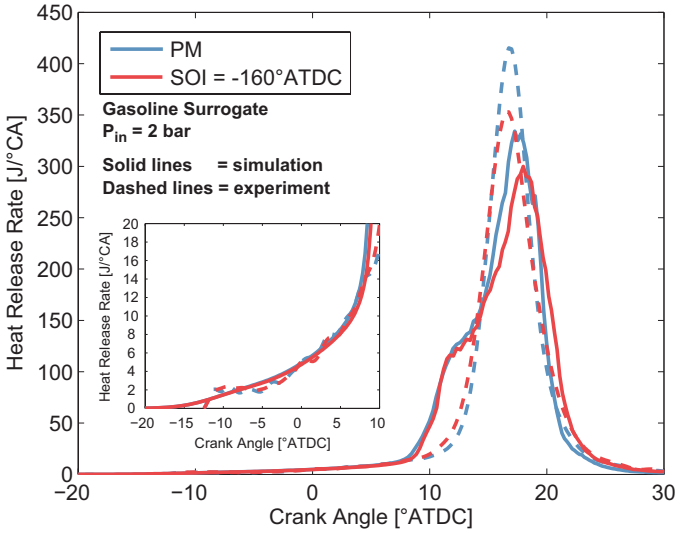

Figure 7.2: HRR as a function of crank angle at $P_{in} = 2$ bar for fully-premixed (PM), and PFS with 13% DI and SOI = -160°ATDC.

temperature zones reaching hot-ignition first.

The HRR from the simulation versus crank angle is compared to the experiment for the SOI = −75°ATDC and SOI = −60°ATDC cases in Fig. 7.3. Again, the simulation shows a wider HRR profile and lower peak HRR, but captures the LTHR region (inset) well. For these more stratified cases, the simulated HRR profile shows a two-peak structure similar to the previous section. The two-peak structure may be due to limitations of the chemical kinetic mechanism in predicting the auto-ignition of a wide range of ϕ (rich to lean).

The cumulative distribution of mass at TDC as a function of ϕ is presented in Fig. 7.4 for the PM case and PFS cases with SOI = -160°ATDC, SOI = -75°ATDC, and -60°ATDC at $P_{in} = 2$ bar. As expected, the PM case is well-mixed at the premixed ϕ specified. The SOI = -160°ATDC case has a smooth ϕ distribution ranging from $\phi \approx 0.66$ to $\phi \approx 0.74$. The SOI = -75°ATDC case has a wider range of ϕ than the earlier SOI case, ranging from $\phi \approx 0.64$ to $\phi \approx 1.0$. Lastly, the SOI = -60°ATDC case has a similar range of ϕ compared to SOI = -75°ATDC, but it is shifted towards $\phi = 1.0$ because of the increased amount of CSP (which has a composition equivalent to $\phi = 1.0$) compared to the other cases. The PFS fuel distributions are smooth, so the bimodal heat release in Fig. 7.3 is not a result of a bimodal fuel distribution. As discussed previously, the appearance of the bimodal heat release may be due to limitations in the chemical kinetic mechanism in predicting the ignition timing of a wide range of ϕ. The next sections analyze the temperature and HRR dependence on ϕ for the PFS cases.

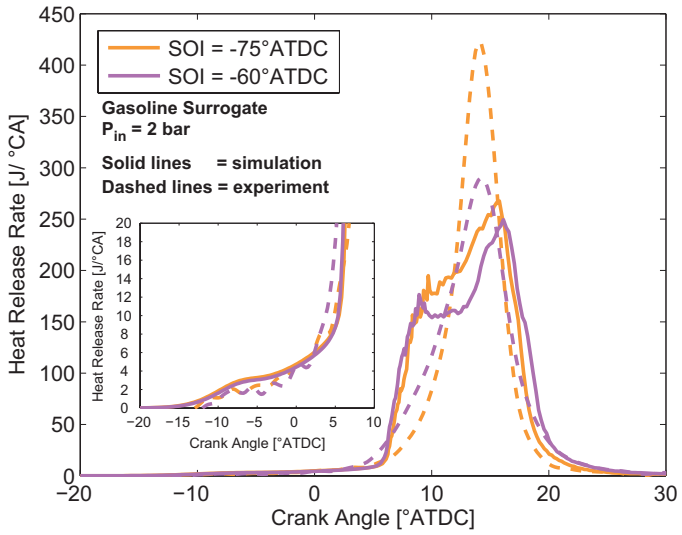

Figure 7.3: HRR as a function of crank angle at $P_{in} = 2$ bar for PFS with 13% DI and SOI = -75°ATDC, -60°ATDC.

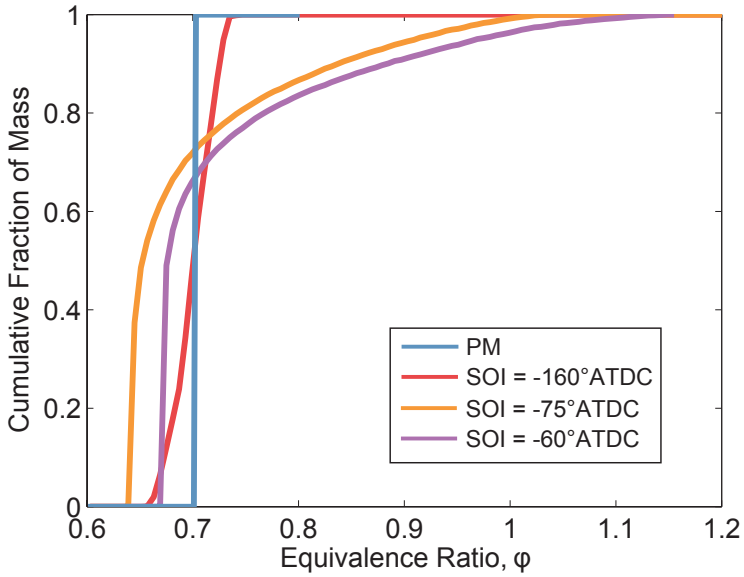

Figure 7.4: Cumulative distribution of mass at TDC for the $P_{in} = 2$ bar cases considered in this chapter: PM, SOI = -160°ATDC, SOI = -75°ATDC, and -60°ATDC.

7.2 SOI = −160°ATDC

Similar to the previous chapter, the temperature of each in-cylinder computational cell for the PFS case with 13% DI and SOI = −160°ATDC is plotted versus the cell ϕ at selected crank angles in Fig. 7.5. It can be seen in Fig. 7.5 that there is no discernible thermal stratification present at $\sim -10°$ATDC. It is worth noting that the temperature-ϕ distribution is nearly the same at −20°ATDC (not shown), suggesting that the small amount of heat release that has occurred by −10°ATDC has not had a significant impact on the thermal stratification. Given this distribution, the intermediate ϕ reach hot-ignition first. The highest-ϕ have a lower temperature at $\sim -10°$ATDC, so these regions do not reach hot-ignition until after the intermediate-ϕ regions. This may be due to the highest-ϕ being near the piston and/or cylinder liner, which is cold relative to the gas temperature. Although Fig. 7.5 provides a useful visualization of the in-cylinder processes, the process can be more clearly discerned by evaluating the heat release and temperature in the different ϕ regions as a function of crank angle by organizing the in-cylinder grid cells into bins in ϕ space of width 0.04.

The HRR from each ϕ bin of width 0.04 is presented in Fig. 7.6. Before hot-ignition at about 8°ATDC, the HRR is dominated by $\phi = 0.68 - 0.72$. Hot-ignition occurs first in the bin of $\phi > 0.72$, followed shortly after by $\phi = 0.68 - 0.72$. The premixed portion of the charge does not contribute much to the HRR until it reaches hot-ignition around 15°ATDC. Because the total HRR from each bin can be influenced by the bin mass, the mass-specific heat release rate, HRR_ϕ, is used to more fairly compare the relative reactivity of each bin.

HRR_ϕ is presented versus crank angle in Fig. 7.7. Fig. 7.7 shows that the different ϕ bins have approximately the same HRR_ϕ before about −5°ATDC. The LTHR/ITHR prior to hot-ignition is more pronounced with increasing ϕ, as evidenced by the more gradual slope of increasing HRR_ϕ leading up to hot-ignition. Again, it is clear that hot-ignition occurs in order of decreasing ϕ.

The mass-weighted temperature (T_ϕ) of each bin versus crank angle is presented in Fig. 7.8. It can be seen in Fig. 7.8 that the bins of $\phi = 0.68 - 0.72$ and $\phi > 0.72$ have about the same temperature at −10°ATDC. The bin of $\phi < 0.68$ has a lower mass-weighted temperature because it includes the cooler near-wall gases. Approaching TDC, the bin of $\phi > 0.72$ increases in temperature more rapidly than the other bins because of the increased LTHR/ITHR (apparent in Fig. 7.6). The LTHR/ITHR from the bin of $\phi = 0.68 - 0.72$ keeps the bin temperature from decreasing after TDC due to piston expansion. Cooling from piston expansion after TDC is evident for $\phi < 0.68$. Because the SOI is sufficiently early in this case, the range of ϕ is quite limited and the thermal stratification evident in the previous section is not present here. However, there is increased overall reactivity with increasing ϕ because the pressure is sufficiently high for the fuel to be ϕ-sensitive.

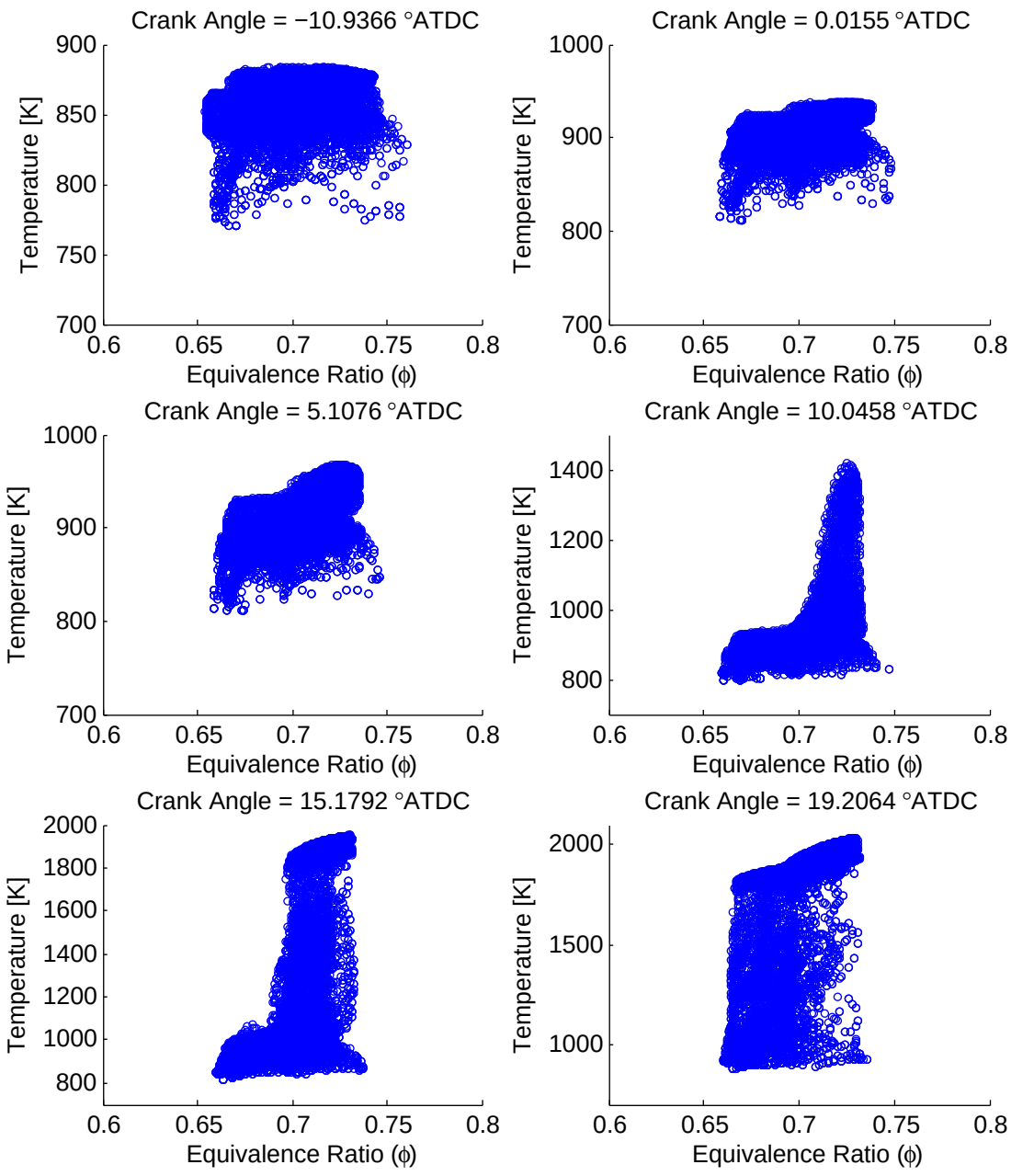

Figure 7.5: Scatter plots of temperature versus ϕ at selected crank angles for PFS with 13% DI, SOI $= -160°$ATDC, $P_{in} = 2$ bar, $T_{in,sim.} = 379$ K.

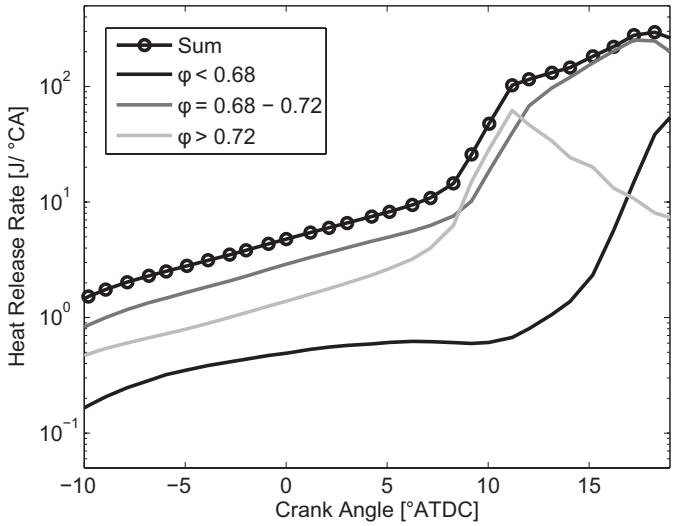

Figure 7.6: Total heat release rate (in J/°CA) for bins of ϕ versus crank angle for PFS with 13% DI, SOI = −160°ATDC, $P_{in} = 2$ bar, $T_{in,sim.} = 379$ K.

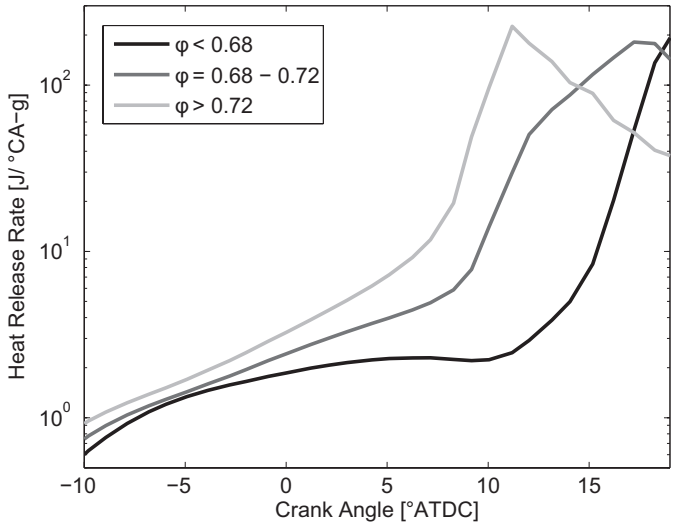

Figure 7.7: Mass-specific HRR (in J/°CA-g) for bins of ϕ versus crank angle for PFS with 13% DI, SOI = −160°ATDC, $P_{in} = 2$ bar, $T_{in,sim.} = 379$ K.

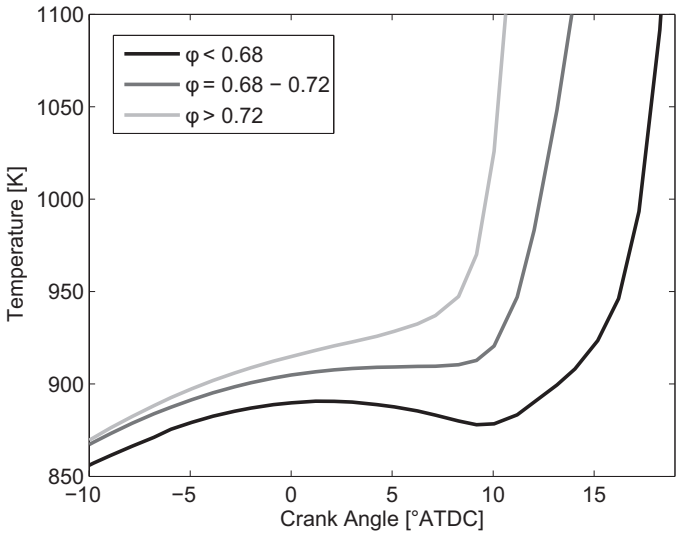

Figure 7.8: Mass-weighted temperature versus crank angle for bins of ϕ for PFS with 13% DI, SOI = $-160°$ATDC, $P_{in} = 2$ bar, $T_{in,sim.} = 379$ K.

7.3 SOI = $-75°$ATDC

Following the same analysis as the previous section, the temperature of each in-cylinder computational cell for the PFS case with 13% DI and SOI = $-75°$ATDC is plotted versus the cell ϕ at selected crank angles in Fig. 7.9. It can be seen in Fig. 7.9 that there is thermal stratification evident at $\sim -10°$ATDC. Moving towards TDC, increasing LTHR/ITHR with increasing ϕ leads to all ϕ having approximately the same temperature near TDC. As hot-ignition begins to occur for the highest ϕ around 5°ATDC, the temperature slightly increases with increasing ϕ. Hot-ignition then occurs from higher-ϕ regions to lower-ϕ regions, with peak ϕ being about stoichiometric. Again, this process can be more clearly discerned by evaluating the heat release and temperature in the different ϕ regions as a function of crank angle by organizing the in-cylinder grid cells into bins in ϕ space of width 0.10.

The HRR from each ϕ bin of width 0.10 versus crank angle is presented in Fig. 7.10. Prior to hot-ignition of the highest-ϕ regions at about 5°ATDC, the majority of heat release occurs in $\phi < 0.65$ and $\phi = 0.65 - 0.75$. Interestingly, the HRR from these two bins is nearly identical from $-10°$ATDC to $-4°$ATDC at which point the bin of $\phi = 0.65 - 0.75$ exhibits a higher HRR before hot-ignition. This is indicative of increased LTHR/ITHR at the slightly higher ϕ and of a similar mass between the two bins. The highest-ϕ regions have lower total HRR due to their lower bin mass. It it evident in Fig. 7.10 that hot-ignition occurs in order of decreasing ϕ. Because the total HRR from each bin can be influenced by the bin mass, the mass-specific heat release rate, HRR_ϕ, is used to more fairly compare the relative reactivity of each bin.

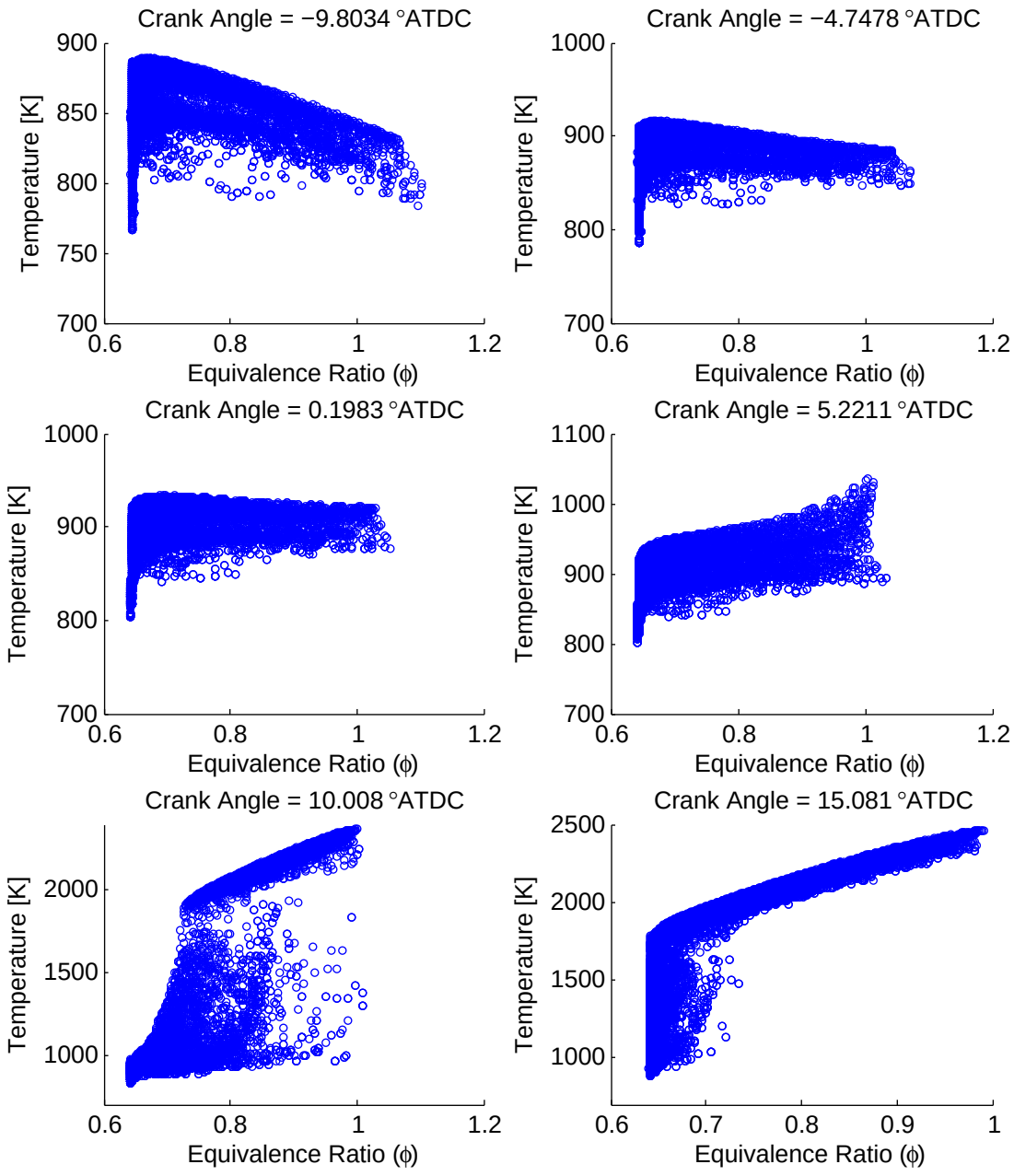

Figure 7.9: Scatter plots of temperature versus ϕ at selected crank angles for PFS with 13% DI, SOI $= -75°$ATDC, $P_{in} = 2$ bar, $T_{in,sim.} = 372$ K.

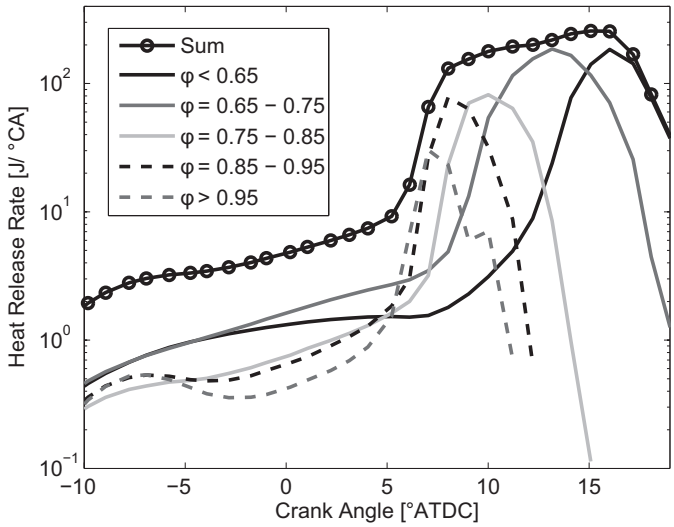

Figure 7.10: Total heat release rate (in J/°CA) for bins of ϕ versus crank angle for PFS with 13% DI, SOI = $-75°$ATDC, $P_{in} = 2$ bar, $T_{in,sim.} = 372$ K.

HRR_ϕ is presented versus crank angle in Fig. 7.11. It is evident in Fig. 7.11 that the HRR_ϕ increases with increasing ϕ during LTHR and ITHR, before about 5°ATDC. A shorter delay between the pre-ignition reactions and hot-ignition is observed for higher ϕ, with hot-ignition occurring in order of decreasing ϕ.

The mass-weighted temperature (T_ϕ) of each bin versus crank angle is presented in Fig. 7.12. Before TDC, the temperature decreases with increased ϕ for the stratified regions of the charge ($\phi > 0.65$) due to evaporative cooling from the liquid fuel spray and decreased compression heating from lower values of γ. Again, the premixed portion of the charge ($\phi < 0.65$) has a lower mass-averaged temperature than $\phi = 0.65 - 0.75$ because it includes cooler near-wall gases. The higher rate of heat release from LTHR/ITHR in the higher-ϕ regions increases their temperature more rapidly such that all of the stratified regions ($\phi > 0.65$) have approximately the same temperature at TDC. Given this nearly uniform temperature distribution at TDC, hot-ignition occurs in order of decreasing ϕ.

7.4 SOI = $-60°$ATDC

Carrying out the same analysis as previous sections, the temperature of each in-cylinder computational cell for the PFS case with 13% DI and SOI = $-60°$ATDC is plotted versus the cell ϕ at selected crank angles in Fig. 7.13. At $\sim -10°$ATDC, thermal stratification is evident with decreasing temperature for increasing ϕ. As crank angle progresses, the pre-ignition heat release that is more prominent for higher-ϕ alters the temperature distribution, such that all ϕ regions have approximately the same temperature at TDC. Similar to the

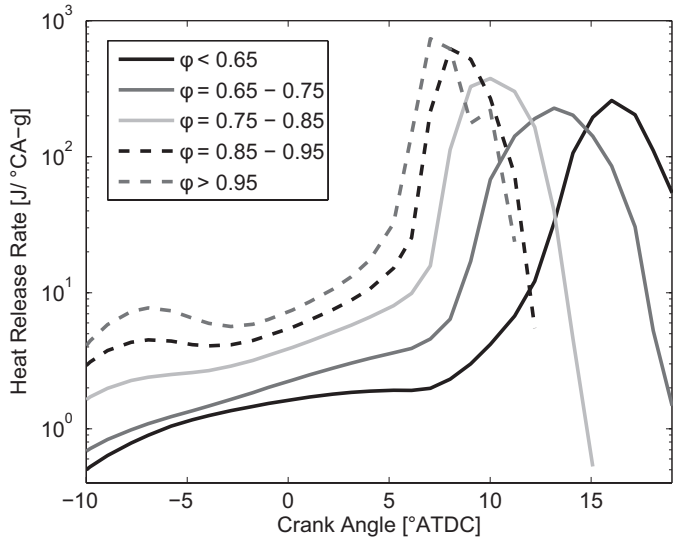

Figure 7.11: Mass-specific HRR (in J/°CA-g) for bins of ϕ versus crank angle for PFS with 13% DI, SOI = −75°ATDC, $P_{in} = 2$ bar, $T_{in,sim.} = 372$ K.

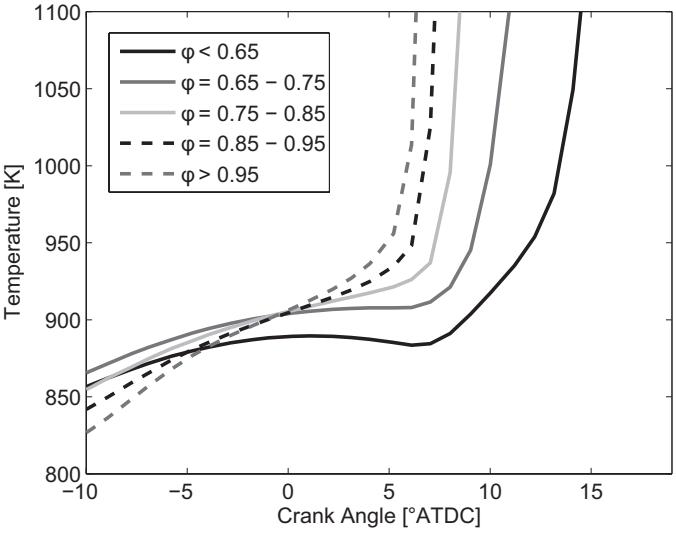

Figure 7.12: Mass-weighted temperature versus crank angle for bins of ϕ for PFS with 13% DI, SOI = −75°ATDC, $P_{in} = 2$ bar, $T_{in,sim.} = 372$ K.

$SOI = -75°$ATDC case, hot-ignition begins to occur for the highest ϕ around 5°ATDC with the temperature slightly increasing with increasing ϕ. Hot-ignition then occurs from higher-ϕ regions to lower-ϕ regions, with peak ϕ being above about $\phi = 1.1$ (compared to peak ϕ of about 1.0 for the $SOI = -75°$ATDC case). This process can be more clearly discerned by evaluating the heat release and temperature in the different ϕ regions as a function of crank angle by organizing the in-cylinder grid cells into bins in ϕ space of width 0.10.

The HRR from each ϕ bin of width 0.10 versus crank angle is presented in Fig. 7.14. Before the hot-ignition of the highest-ϕ bin at about 5°ATDC, the heat release is dominated by $\phi < 0.70$ as the majority of in-cylinder mass is contained in this bin. The higher ϕ regions have lower HRR because of the decreased in-cylinder mass at higher-ϕ. The is a noticeable bump in the total HRR between about $-10°$ATDC and $-5°$ATDC from LTHR, with the $\phi > 1.0$ region exhibiting the strongest LTHR. The mass-specific heat release rate, HRR_ϕ, is again used to more fairly compare the relative reactivity of each bin.

HRR_ϕ is presented versus crank angle in Fig. 7.15. It is evident in Fig. 7.15 that the HRR_ϕ increases with increasing ϕ during LTHR and ITHR, before about 5°ATDC. A shorter delay between the pre-ignition reactions and hot-ignition is observed for higher ϕ, with hot-ignition occurring in order of decreasing ϕ. The behavior of this case is very similar to cases with similar injection timings.

The mass-weighted temperature (T_ϕ) of each bin versus crank angle is presented in Fig. 7.16. Before TDC, the temperature decreases with increased ϕ for the stratified regions of the charge ($\phi > 0.70$) due to evaporative cooling from the liquid fuel spray and decreased compression heating from lower values of γ. Again, the premixed portion of the charge ($\phi < 0.70$) has a lower mass-averaged temperature than $\phi = 0.70 - 0.80$ because it includes cooler near-wall gases. The higher rate of heat release from LTHR/ITHR in the higher-ϕ regions increases their temperature more rapidly such that all of the stratified regions ($\phi > 0.70$) have approximately the same temperature at TDC. Given this nearly uniform temperature distribution at TDC, hot-ignition occurs in order of decreasing ϕ.

7.5 Temperature dependence of HRR

The temperature dependence of HRR elucidates the difference heat release characteristics between the different SOI cases. Fig. 7.17 compares the HRR as a function of in-cylinder temperature for the four cases presented in this section. It can be seen in Fig. 7.17 that hot ignition begins at slightly higher temperatures for the PM and $SOI = -160°$ATDC cases and that the peak temperatures are about the same for all cases.

Because of the importance of LTHR/ITHR in altering the temperature distribution of the mixture stratification prior to hot-ignition, the LTHR/ITHR region is highlighted in Fig. 7.18. The PM and $SOI = -160°$ATDC show nearly identical LTHR/ITHR behavior with temperature, as do the $SOI = -75°$ATDC and $SOI = -60°$ATDC cases. All cases begin to exhibit LTHR at about 830 K with a peak in LTHR occurring for the later SOI timings at around 870 K. The PM and $SOI = -160°$ATDC cases do not exhibit an LTHR

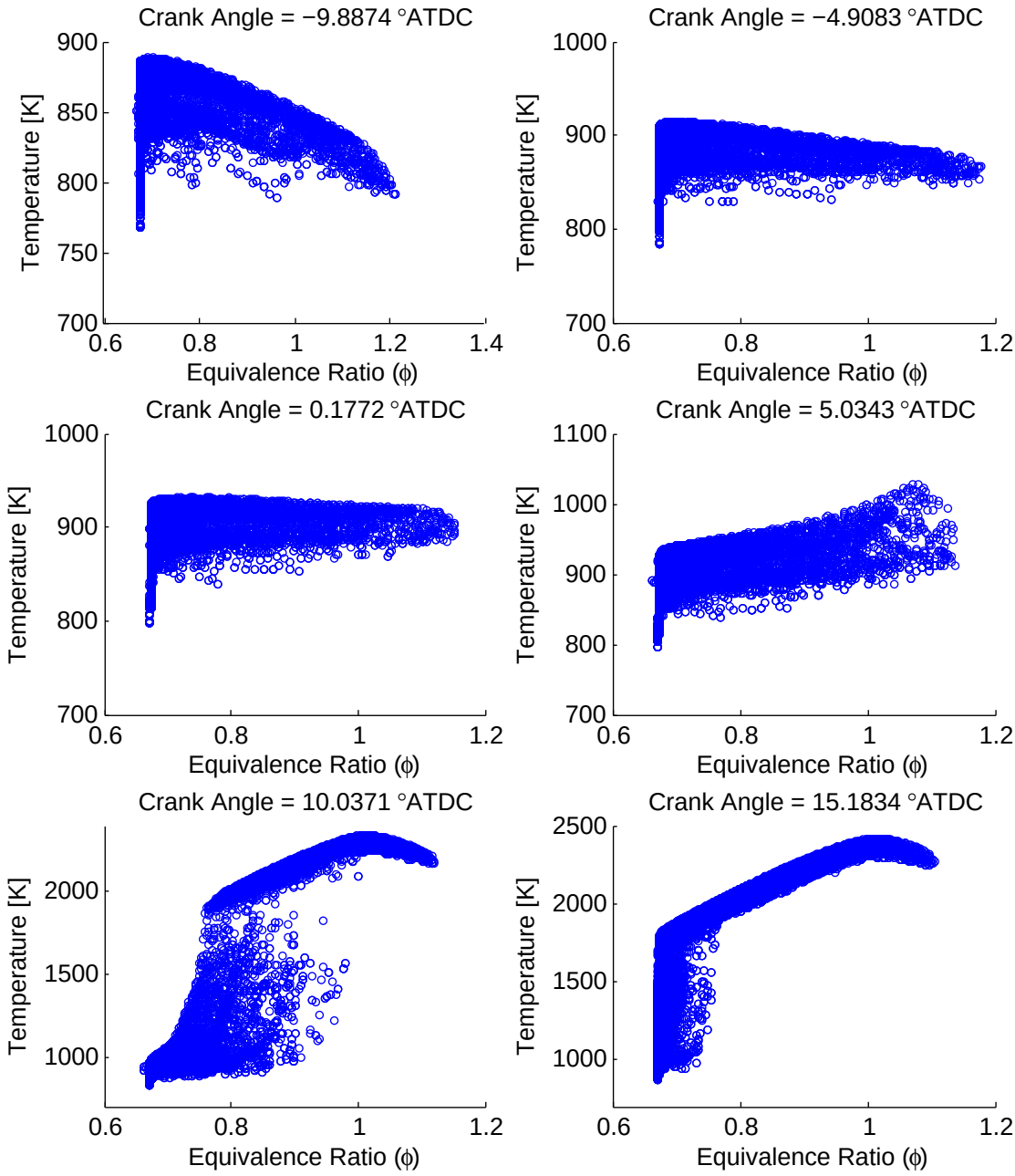

Figure 7.13: Scatter plots of temperature versus ϕ at selected crank angles for PFS with 13% DI, SOI $= -60°$ATDC, $P_{in} = 2$ bar, $T_{in,sim.} = 374$ K.

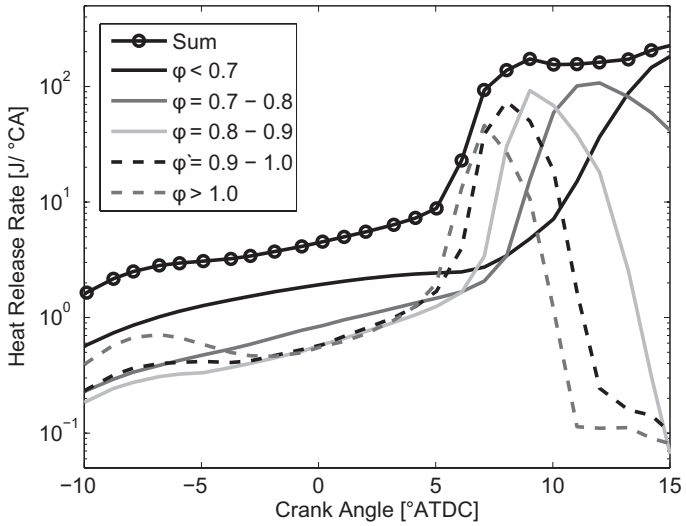

Figure 7.14: Total heat release rate (in J/°CA) for bins of ϕ versus crank angle for PFS with 13% DI, SOI = −60°ATDC, $P_{in} = 2$ bar, $T_{in,sim.} = 374$ K.

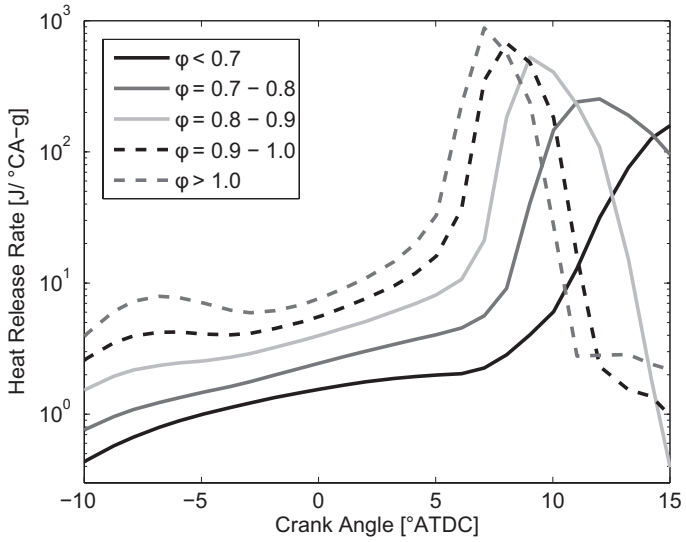

Figure 7.15: Mass-specific HRR (in J/°CA-g) for bins of ϕ versus crank angle for PFS with 13% DI, SOI = −60°ATDC, $P_{in} = 2$ bar, $T_{in,sim.} = 374$ K.

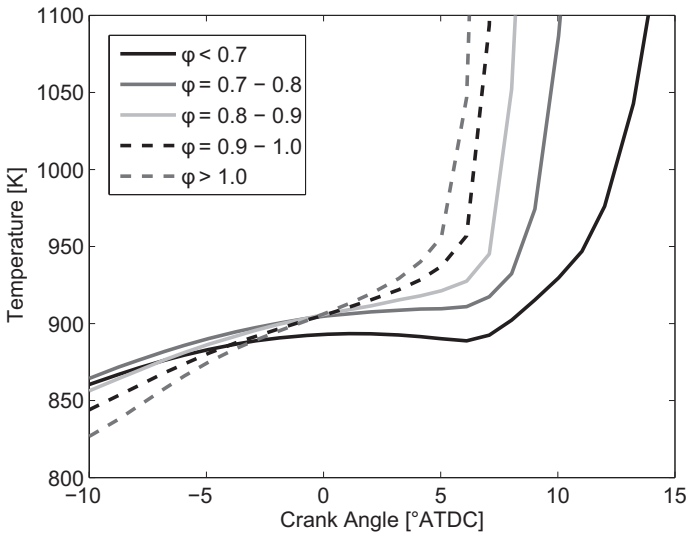

Figure 7.16: Mass-weighted temperature versus crank angle for bins of ϕ for PFS with 13% DI, SOI = $-60°$ATDC, $P_{in} = 2$ bar, $T_{in,sim.} = 374$ K.

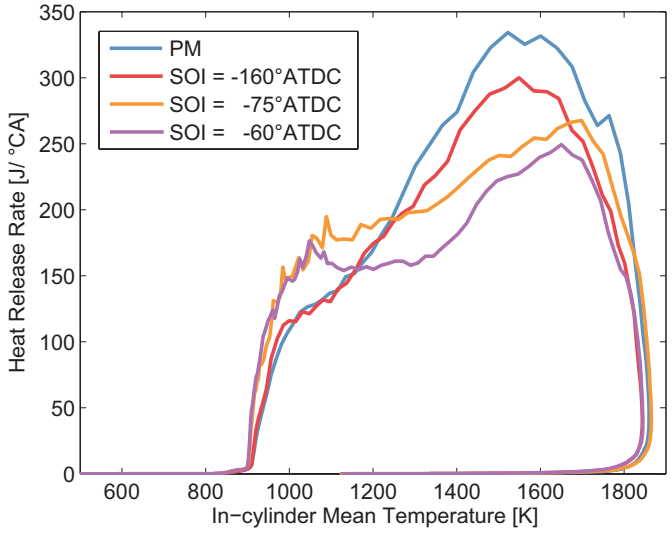

Figure 7.17: HRR as a function of temperature at $P_{in} = 2$ bar for fully-premixed (PM), and PFS with 13% DI and SOI = -160°ATDC, -75°ATDC, -60°ATDC.

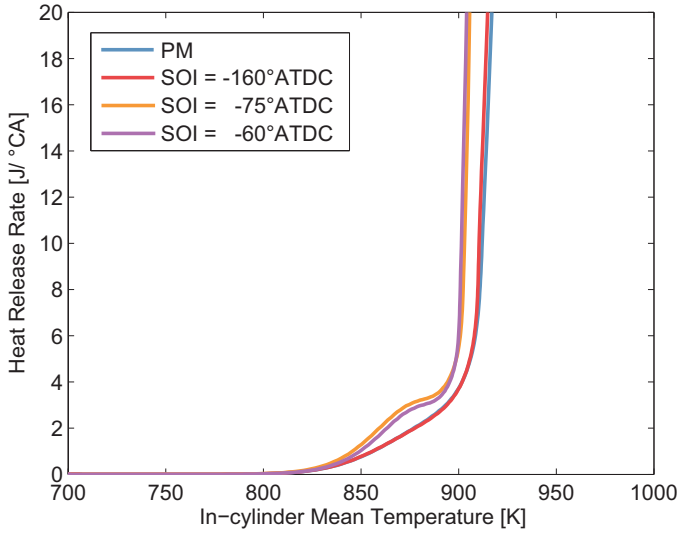

Figure 7.18: HRR as a function of temperature at P_{in} = 2 bar for fully-premixed (PM), and PFS with 13% DI and SOI = -160°ATDC, -75°ATDC, -60°ATDC.

peak, but transition rather smoothly between the different heat release regimes. The later SOI timing cases reach hot-ignition at a slightly lower temperature than the PM and $SOI = -160°$ATDC cases.

7.6 Summary

In this chapter, simulations of Partial Fuel Stratification (PFS), a strategy for reducing the maximum pressure rise rate in compression-ignition engines using fuel stratification, have been performed using CONVERGE with a 96-species reduced mechanism for a 4-component gasoline surrogate. Comparison is made between simulation results and experiments from the Sandia HCCI/GCI engine at a compression ratio of 14:1. Detailed analysis of the heat release from and temperature of each equivalence ratio region is performed to elucidate the underlying physical processes that contribute to the different behavior of PFS for gasoline at various direct-injection timings. The major findings of the section are:

- For an early injection timing of $SOI = -160°$ATDC, sequential auto-ignition occurs in order of decreasing ϕ. There is increased LTHR/ITHR with increasing ϕ, which leads to increased temperature of the higher-ϕ near TDC. The sequential auto-ignition occurs over a narrow range of ϕ such that significant difference is not observed compared to HCCI.
- For later injection timings, $SOI = -75°$ATDC and $SOI = -60°$ATDC, sequential auto-ignition of the charge occurs in order of decreasing ϕ because the increased

LTHR/ITHR for higher ϕ compensates for evaporative cooling and decreased compression heating from the lower ratio of specific heats such that all stratified regions having approximately the same temperature at TDC. As such, the premixed portion of the charge auto-ignites last, after the higher-ϕ regions. Behavior of these cases is similar to the 17% DI fraction, $SOI = -60°$ATDC case of the previous chapter.

Chapter 8

Concluding remarks

This dissertation computationally investigates the interactions between the fundamental in-cylinder processes in gasoline compression ignition (GCI) engines with the aim of better understanding the governing processes and how they influence engine operation. The work is comprised of two main components: (1) the development of a novel reduced chemical kinetic mechanism for a four-component gasoline surrogate that is suitable for computational fluid dynamics (CFD) simulations of GCI, and (2) development, execution, and analysis of CFD simulations of GCI based on engine experiments from Sandia National Laboratories Combustion Research Facility.

8.1 Conclusions on reduced mechanism development

A reduced mechanism has been developed for an RD387 gasoline surrogate comprised iso-octane, n-heptane, toluene, and 2-pentene previously proposed by Mehl *et al.* (2011a). The reduced mechanism has been validated against the detailed mechanism and experimental data for auto-ignition delay time and flame speed for the four-component RD387 gasoline surrogate. The reduced mechanism performs well for ignition delay time across a wide range of equivalence ratios, pressures, and temperature relevant to GCI engines. Although flame propagation is generally too slow compared to sequential auto-ignition to be important in GCI, the reduced mechanism performs well with respect to laminar flame speed at near-TDC temperatures and pressures.

The reduced mechanism is packaged as a FORTRAN or C subroutine that returns chemical production rates given the temperature, pressure and species mass fractions. In most codes, the reduced mechanism subroutine replaces the existing subroutine that returns chemical production rates given the CHEMKIN-formatted reaction mechanism. As such, if the user does not have access to modify the source code or to user-defined functions to bypass the specified subroutines for a given code, the reduced mechanism can not be used with that code. Another drawback of the reduced mechanism is that some advanced numerical techniques for computational speedup developed for CHEMKIN-formatted mechanisms, such as

adaptive preconditioning (McNenly *et al.*, 2013) and analytic Jacobian (Perini *et al.*, 2012), cannot be used with the reduced mechanism.

The reduced mechanism developed in this work is ideally suited for CFD simulations of GCI with fuels or fuel surrogates containing iso-octane, n-heptane, toluene, and 2-pentene, specifically the RD387 surrogate proposed by Mehl *et al.* (2011a). The mechanism should also perform well for Primary Reference Fuels (blends of iso-octane and n-heptane) and simpler surrogates containing the three components iso-octane, n-heptane, and toluene.

8.2 Conclusions on CONVERGE simulations of PFS/GCI

In this dissertation, simulations of Partial Fuel Stratification (PFS), a strategy for reducing the maximum pressure rise rate in compression-ignition engines using fuel stratification, have been performed using CONVERGE with the 96-species reduced mechanism for a 4-component gasoline surrogate also developed in this work. Simulations are modeled after experiments performed in the Sandia National Laboratories HCCI/GCI engine at a compression ratio of 14:1 for a span of direct-injection fractions at intake pressures of 1 bar and 2 bar and a span of direct-injection timings at an intake pressure of 2 bar. Comparison is made between pressure and heat release profiles obtained in the experiment to those from the simulation. Detailed analysis of the heat release from and temperature of each equivalence ratio region is performed to elucidate the underlying physical processes that contribute to the different behavior of the various ϕ regions introduced by the late direct-injection and of PFS as a whole for gasoline at 1 bar and 2 bar intake pressure.

The major findings of this dissertation with respect to intake pressure are:

- For 1 bar intake pressure, sequential auto-ignition of the stratified charge (excluding the premixed portion of the charge) occurs in order of increasing ϕ because the temperature is higher for lower ϕ due to lesser influence of evaporative cooling and increased compression heating from the higher ratio of specific heats. The premixed portion of the charge auto-ignites before the highest-ϕ regions. The sequential auto-ignition occurs too fast for useful reduction of the maximum pressure rise rate compared to HCCI.

- For 2 bar intake pressure, sequential auto-ignition of the stratified charge occurs in order of decreasing ϕ because the increased LTHR/ITHR for higher ϕ compensates for evaporative cooling and decreased compression heating from the lower ratio of specific heats such that all stratified regions having approximately the same temperature at TDC. As such, the premixed portion of the charge auto-ignites last, after the higher-ϕ regions. The sequential auto-ignition occurs over a longer time period than at 1 bar intake pressure such that a sizeable reduction in the maximum pressure rise rate compared to HCCI can be achieved.

The major findings of this dissertation with respect to direct-injection timing at 2 bar intake pressure are:

- For an early injection timing of $SOI = -160°$ATDC, sequential auto-ignition occurs in order of decreasing ϕ. There is increased LTHR/ITHR with increasing ϕ, which leads to increased temperature of the higher-ϕ near TDC. The sequential auto-ignition occurs over a narrow range of ϕ such that not much difference is observed compared to HCCI.
- For later injection timings, $SOI = -75°$ATDC and $SOI = -60°$ATDC, sequential auto-ignition of the charge occurs in order of decreasing ϕ because the increased LTHR/ITHR for higher ϕ compensates for evaporative cooling and decreased compression heating from the lower ratio of specific heats such that all stratified regions having approximately the same temperature at TDC. As such, the premixed portion of the charge auto-ignites last, after the higher-ϕ regions.

8.3 Outlook

This dissertation has illustrated a process of optimizing a large, detailed chemical kinetic mechanism for use with computational tools to better understand experimentally observed trends. Computational tools are an efficient means to improve understanding of interactions that are not directly measured in an experiment. Continued improvement of computational tools is required as they become more important in the development of new internal combustion engine technologies. One area of improvement to be targeted is the chemical kinetic mechanism as the heat release behavior of complex fuels in advanced engine operating strategies, specifically at low- and intermediate-temperatures, can be critically important to engine operation.

Although large, detailed mechanisms represent a complex description of a chemically reacting system, the chemical heat release observed in the experiments is not always well-captured by these mechanisms. For instance, the pressure onset of low- and intermediate-temperature heat release for gasoline, which has been shown to be important for gasoline compression ignition engine operation, is not well captured by currently available detailed chemical mechanisms. The reasons for this are under investigation by numerous researchers. Once the predictions of the detailed mechanism are improved, however, the reduction schemes may need to be modified to target (that is, maintain accuracy of) the predictions of the pressure sensitivity of low- and intermediate-temperature heat release. This may necessitate including additional target metrics, such as first- and second-stage ignition delay times or validating the mechanism reduction choices using a simplified engine model for which the magnitude of low- and intermediate-temperature heat release could be quantified. The improvement of all levels of chemical kinetic mechanisms is necessary to continue to develop the predictive capability of computational tools in combustion with the goal of designing more efficient and cleaner-burning internal combustion engines.

Appendix A

96-species reduced mechanism

Table A.1: Reduced mechanism effective reactions

Number	Reaction
1	2O2 + HOC6H4CH3 = H + OH + 3CO + CH3CHO + C2H2
2	O2 + O2C6H4CH3 = H + 3CO + CH3CHO + C2H2
3	H + O2 = O + OH
4	H2 + O = H + OH
5	H2 + OH = H + H2O
6	H2 = 2H
7	H + O2 = HO2
8	O2 + H2O2 = 2HO2
9	O + CO = CO2
10	H + CH3 = CH4
11	H + HO2 + CO = O2 + CH2O
12	2CH2O = CO + CH3OH
13	CH3OH = OH + CH3
14	O2 + CH3 = CH3O2
15	CH2O + CH3O2 = H + CO + CH3O2H
16	2CH3 = C2H6
17	H + C2H5 = C2H6
18	H + C2H4 = C2H5
19	H2 + C2H5 + C2H2 = H + 2C2H4
20	O + C2H5 = H + CH3CHO
21	H + CO + CH3 = H2 + CH2CO
22	CH3COCH3 = CO + 2CH3
23	H + CO + CH3COCH2O2H = O2 + CH2O + CH3 + CH2CO
24	C2H3CHO = H2 + CO + C2H2
25	C2H5CHO = H + CO + C2H5
26	H + H2O + C3H6 = OH + CH3 + C2H5

27 O + C3H6 = 2H + CH3CHCO
28 C3KET13 = O2 + CH2O + C2H4
29 OH + CO + C2H5 + C2H4 = H2O + CH2O + C4H6
30 H + 2OH + BC5H10 = H2O + 3CH3 + CH2CO
31 PC4H9O2 = O2 + C2H5 + C2H4
32 C4H8OOH1-3O2 = O2 + OH + CH2O + C3H6
33 C4H8OOH1-3O2 = OH + NC4KET13
34 CO + CH3 + C2H4 = C2H5COCH2
35 O2 + NC3H7CHO = H + HO2 + CO + C3H6
36 HO2 + TC4H9 = OH + CH3 + CH3COCH3
37 CH3 + C3H6 = H + IC4H8
38 TC4H9O2 = O2 + TC4H9
39 CH2O + TC4H9O2 = H + CO + TC4H9O2H
40 O + IC4H8 + TC4H9O2 = H + TC4H9O2H + IC3H5CHO
41 O2 + CH3 + CH3COCH3 = HO2 + IC3H7CHO
42 O + IC4H8 = 2H + IC3H6CO
43 O2 + IC4H7OOH = O + OH + CH2O + CH3 + CH2CO
44 CH3CHCHO = H + C2H3CHO
45 OH + C5H10-2 = C2H5 + C2H5CHO
46 H2O + C3H6 + IC4H8 = H + OH + YC7H14
47 H + YC7H14 = H2 + CH3 + ACC6H10
48 NEOC5H11O2 = O2 + CH3 + IC4H8
49 NEOC5H10OOH-O2 = O2 + CH3 + IC4H7OOH
50 OH + C4H7CHO2-2 = CH3CHO + CH3CHCHO
51 IC8H18 = H + CH3 + C3H6 + IC4H8
52 IC8H18 = 2H + IC8H16
53 TC4H9 + IC4H8 = H + JC8H16
54 AC8H17O2 = O2 + CH3 + C3H6 + IC4H8
55 H + BC8H17O2 = O2 + IC8H18
56 CC8H17O2 = O2 + TC4H9 + IC4H8
57 DC8H17O2 = O2 + CH3 + C3H6 + IC4H8
58 AC8H17O2 = OH + IC8ETERAB
59 AC8H17O2 = OH + IC8ETERAC
60 BC8H17O2 = OH + IC8ETERBD
61 AC8H16OOH-BO2 = O2 + OH + IC8ETERAB
62 BC8H16OOH-CO2 = O2 + HO2 + IC8H16
63 OH + CH2O + IC3H7COC3H6-T = O2 + IC8ETERAB
64 OH + CH2O + TC4H9COC2H4S = O2 + IC8ETERBD
65 DC8H16OOH-BO2 = O2 + OH + IC8ETERBD
66 OH + C5H81-3 = C2H5 + C2H3CHO
67 O2 + OH + C5H10-2 = O2C5H10OH-2
68 NC7H16 = 2H + 2C2H4 + C3H6

69	H2O + CH2O + C3H6 + C4H6 = H + OH + CO + C7H14-3
70	C7H15O2-1 = H + O2 + 2C2H4 + C3H6
71	C7H15O2-2 = O2 + C2H5 + C2H4 + C3H6
72	OH + CO + C7H15O2-3 = O2 + H2O + CH2O + C3H6 + C4H6
73	H + OH + C7H15O2-4 = H2 + O2 + H2O + C2H5 + C3H6 + C2H2
74	C7H14OOH1-3O2 = O2 + H2O + CO + C2H5 + 2C2H4
75	H + OH + C7H14OOH2-4O2 = H2 + O2 + 2H2O + CO + CH3 + C3H6 + C2H2
76	OH + C7H14OOH3-2O2 = H + O2 + H2O + HO2 + C3H6 + C4H6
77	C7H14OOH3-4O2 = O2 + HO2 + C7H14-3
78	H + OH + C7H14OOH3-5O2 = O2 + 2H2O + CH2O + C2H5 + C4H6
79	H + OH + C7H14OOH4-2O2 = H2 + O2 + 2H2O + CO + CH3 + C3H6 + C2H2
80	C7H14OOH2-4O2 = OH + NC7KET24
81	C7H14OOH3-5O2 = OH + NC7KET35
82	C7H14OOH4-2O2 = OH + NC7KET42
83	2OH + CYPDONE = H + 2CO + CH3 + CH2CO
84	O2 + 2CH3 + 2CH2CO = 2H + O + 2OH + C6H5OH
85	H + C6H5CH2J = C6H5CH3
86	H + O2 + C6H5CH3 = O + CH3 + C6H5OH
87	H + C6H5CH3 + C6H5CHO = C6H5CH2J + C6H5CH2OH
88	OH + C6H5CH2J = C6H5CH2OH
89	CH4 + CH2 = 2CH3
90	O2 + CH3 + C4H6 = C5H91O2-3
91	O2 + C5H10-2 = H + C5H92O2-4
92	C5H91O2-3 = OH + CY3C5H8O

Appendix B

From reduced chemistry to UDF in CONVERGE

Follow these steps to incorporate the reduced chemistry as a user-defined function (UDF) in CONVERGE (version 2.1.0).

1. Download the latest Converge UDF executable (e.g. *converge-udf-2.1.0-openmpi-linux-64-071513*) and place in the run directory. If the executable is located somewhere else, it should be okay to call the executable from within the run directory.

2. Make a folder named *udf* in the run directory.

3. Download the UDF header files from the Converge website and place them in the *udf* directory. Alternatively, place symbolic links to the header files in the *udf* directory.

   common_shared.h mpi_replacement_functions.h prototype_shared.h safe_prototypes.h table.h const_shared.h parsing.h structures_shared.h tools_shared.h

4. Make an empty file called *user_header.h* in the *udf* directory. The compiler needs this file, but it is used for variables that are added for user created input files which is not needed for the reduced chemistry.

5. Place the c-version of the reduced chemistry (*ckwyp.c*) and header file (*reduced.h*) in the *udf* directory. Also make sure the *mech.dat* file has the species in the correct order dictated by the *ckwyp.c* file.

6. Converge passes concentrations (moles/cc) to the ckwyp subroutine and not mass fractions, so there is no need to convert from mass fractions to concentrations. Make the following change to the *ckwyp.c* file: comment out the section of code that converts mass fractions to concentrations and replace with loop to assign "mass fraction vector" y[k] to "concentration vector" xcon[k].

```
 /* compute concentrations from mass fractions
section for routine compatible with CKWYP */
/* converge supplies concentrations
sumyow = 0.0e0;
for (k = 0; k < NS; ++k) {
sumyow += y[k] / wt[k];
}
sumyow = sumyow * (*t) * ru;
for (k = 0; k < NS; ++k) {
xcon[k] = *p * y[k] / (sumyow * wt[k]);
}
*/// /* Added by Ben Wolk 07/30/2013
* Converge supplies concentrations */
for (k = 0; k < NS; ++k) {
xcon[k] = y[k];
}
```

7. There is an error as of August 2013 in *ckwyp.c* when calling `CalcFallOffRate`. The "E+30" should be "1.E+30".

```
 CalcFallOffRate(t, 5.E-01, 1.E-30, E+30, 1.E+10, rl[0], xm[11], &rf[11],
&rb[11]);
```

```
 CalcFallOffRate(t, 5.E-01, 1.E-30, 1.E+30, 1.E+10, rl[0], xm[11], &rf[11],
&rb[11]);
```

8. Place or create *user_reac_rate.c* in the *udf* directory. The file contains the following lines:

```
#include <stdlib.h>
#include <stdio.h>

int ckwyp_(double *pres, double *temp, double *sage_molefrac, int *ICKWRK,
double *RCKWRK, double *sage_molefrac_dot);


int user_reac_rate(double pres,double temp,
double *sage_molefrac,double *sage_molefrac_dot)
{
int ICKWRK[2];
double RCKWRK[2];
double pres1;
double temp1;
pres1 = pres/10.0; // convert N/m2 to dyne/cm2
```

```
temp1 = temp;

ckwyp_(&pres1, &temp1, sage_molefrac, ICKWRK, RCKWRK, sage_molefrac_dot);

return 0;

 }
```

9. Create *makefile* with the following lines:

```
# Wrapper makefile for libconverge_udf
# this makefile will attempt to autodetect the architecture
# and call the appropriate makefile

UNAME := $(shell uname)
UNAME_M := $(shell uname -m)

ifeq ($(UNAME),AIX)
FILENAME=makefile-ibm_64_xlc
endif

ifeq ($(UNAME),Linux)
ifeq ($(UNAME_M),x86_64)
FILENAME=makefile-l_x86_64_gcc
else
FILENAME=makefile-l_x86_32_icc
endif
endif

all:  udf

udf:
@make -f $(FILENAME);

clean:
@rm -f *.o libconverge_udf.so libfortran_udf.so\
static/libconverge_udf.a static/libfortran_udf.a
```

10. Create *makefile-l_x86_64_gcc* with the following lines:

```
# makefile for converge_udf
##### choose to compile with or without FORTRAN #####
#WITH_FORTRAN = YES
WITH_FORTRAN = NO
##### end of choices #####

CC = gcc
CFLAGS = -O3 -fPIC -DNO_MPI -Werror-implicit-function-declaration -Werror
CCFLAGS_1 = -shared
LIB_FLAGS =
LIBNAME = converge_udf

F77 = gfortran
#F77 = /usr/local/gcc-4.4.2/bin/gfortran
FLAGS = -fdefault-real-8 -O3 -fPIC
FFLAGS = -shared
LIB_FLAGS =
FORTRAN_LIBNAME = fortran_udf

ifeq ($(WITH_FORTRAN),YES)
CCFLAGS = $(CCFLAGS_1) -L. -l$(FORTRAN_LIBNAME)
endif

ifeq ($(WITH_FORTRAN),NO)
CCFLAGS = $(CCFLAGS_1)
endif

OBJS = user_reac_rate.o ckwyp.o

OBJS_F = ckwyp.o

ifeq ($(WITH_FORTRAN),YES)
all:  fortran_udfs udfs
endif

ifeq ($(WITH_FORTRAN),NO)
all:  udfs
endif
```

```
fortran_udfs:  $(OBJS_F)
$(F77) $(FFLAGS) -o lib$(FORTRAN_LIBNAME).so $(OBJS_F)
ar $(LIB_FLAGS) rc lib$(FORTRAN_LIBNAME).a $(OBJS_F)
mv lib$(FORTRAN_LIBNAME).a static

udfs:  $(OBJS)
$(CC) $(CCFLAGS) -o lib$(LIBNAME).so $(OBJS)
ar $(LIB_FLAGS) rc lib$(LIBNAME).a $(OBJS)
mv lib$(LIBNAME).a static

$(OBJS): common_shared.h const_shared.h mpi_replacement_functions.h \
parsing.h prototype_shared.h safe_prototypes.h structures_shared.h \
tools_shared.h table.h user_header.h

$(OBJS_F):

.c.o:
$(CC) $(CFLAGS) -I$(CONVERGE_ROOT)/udf_include -c $<

.f.o:
$(F77) $(FLAGS) -c $<

clean:
rm -f *.o libconverge_udf.so libfortran_udf.so \
static/libconverge_udf.a static/libfortran_udf.a
```

11. Type *make*.
12. In *inputs.in*, set "udf_flag" to 1.
13. In *udf.in*, set "user_react_rate_flag" to 1. An example *udf.in* is below.

```
#!csi_version=2.1.0
#======================
0 user_spray_main_flag
0 user_nozzle_flag
0 user_inject_flag
0 user_rateshape_flag
0 user_break_flag
0 user_parcel_flag
```

```
0 user_distort_flag
0 user_evap_flag
0 user_coalesce_flag
0 user_colide_flag
0 user_gas_couple_flag
0 user_combust_main_flag
0 user_combust_flag
0 user_combust_ctc_flag
0 user_combust_shell_flag
0 user_combust_multizone_flag
1 user_reac_rate_flag
0 user_reac_mult_flag
0 user_nox_flag User specified subroutine for NOX emissions.
0 user_soot_flag User specified subroutine for soot emissions.
0 user_passive_sor_flag
0 user_g_eqn_flag
0 user_equiv_ratio_flag
0 user_rebound_flag
0 user_film_jet_flag
0 user_film_strip_flag
0 user_film_sources_flag
0 user_film_gradp_flag
0 user_film_splash_flag
0 user_splash_crit_flag
0 user_splash_mass_flag
0 user_splash_radius_flag
0 user_splash_vel_flag
0 user_film_prop_flag
0 user_film_evap_flag
0 user_dt_flag
0 user_source_flag
0 user_source_transport_flag
0 user_event_flag
0 user_ga_merit_flag
0 user_piston_position_flag
0 user_wallvalue_flag
0 user_input_flag
0 user_post_flag
0 user_out_flag
0 user_transfer_flag
0 user_heat_transfer_flag
0 user_set_properties_flag
```

```
0 user_regions_flow_flag
0 user_point_flag
# User defined monitor points table begin:
# <x_coord> <y_coord> <z_coord> <radius>
0 num_points
```

14. Add "export LD_LIBRARY_PATH=./udf/" to the run.sh script (before the executable is called) or type at the command line before running the executable.

Bibliography

J Abraham. Computational study of charge stratification in early-injection SCCI engines under light-load conditions. *International Journal of Automotive Technology*, 12(5):721–732, 2011.

S.M. Aceves, D.L. Flowers, R.W. Dibble, and A. Babajimopoulos. *HCCI and CAI Engines for the Automotive Industry*. Elsevier, 2007.

F. Buda, R. Bounaceur, V. Warth, P.A. Glaude, R. Fournet, and F. Battin-Leclerc. Progress toward a unified detailed kinetic model for the autoignition of alkanes from C4 to C10 between 600 and 1200 K. *Combustion and Flame*, 142(1-2):170–186, July 2005.

W.C. Chang. *Modeling of NOx formation in turbulent flames - development of reduced mechanisms and mixing models*. PhD thesis, 1995.

Lee Chapman. Transport and climate change: a review. *Journal of Transport Geography*, 15(5):354–367, September 2007.

J.-Y. Chen. A General Procedure for Constructing Reduced Reaction Mechanisms with Given Independent Relations. *Combustion Science and Technology*, 57(1-3):89–94, January 1988.

J.-Y. Chen. Automatic generation of reduced mechanisms and their applications to combustion modeling. *Transactions of the Aeronautical and Astronautical Society of the Republic of China*, 33(2):59–67, 2001.

L.C. Chien. *Assessment of reduced mechanisms using one-dimensional stochastic turbulence model*. PhD thesis, 2010.

H Curran. A comprehensive modeling study of iso-octane oxidation. *Combustion and Flame*, 129(3):253–280, May 2002.

D Dahl and I Denbratt. HCCI/SCCI load limits and stoichiometric operation in a multicylinder naturally aspirated spark ignition engine operated on gasoline and E85. *International Journal of Engine Research*, 12:58–68, 2011.

John E Dec and Wontae Hwang. Characterizing the Development of Thermal Stratification in an HCCI Engine Using Planar-Imaging Thermometry. *SAE International Journal of Engines*, 2(1):421–438, 2009.

J Dec, W Hwang, and M Sjöberg. An Investigation of Thermal Stratification in HCCI Engines Using Chemiluminescence Imaging. *SAE Technical Paper*, (2006-01-1518), 2006.

JE Dec, Yi Yang, and Nicolas Dronniou. Boosted HCCI-controlling pressure-rise rates for performance improvements using partial fuel stratification with conventional gasoline. *SAE International Journal of Engines*, 4:1169–1189, 2011.

JE Dec. Advanced compression-ignition engines: understanding the in-cylinder processes. *Proceedings of the Combustion Institute*, 32(2):2727–2742, 2009.

EPA and NHTSA. EPA and NHTSA Set Standards to Reduce Greenhouse Gases and Improve Fuel Economy for Model Years 2017-2025 Cars and Light Trucks, 2012.

Jeffrey S. Gaffney and Nancy A. Marley. The impacts of combustion emissions on air quality and climate From coal to biofuels and beyond. *Atmospheric Environment*, 43(1):23–36, January 2009.

Charles W. Garrett. On global climate change, carbon dioxide, and fossil fuel combustion, 1992.

BM Gauthier, DF Davidson, and RK Hanson. Shock tube determination of ignition delay times in full-blend and surrogate fuel mixtures. *Combustion and Flame*, 139(4):300–311, December 2004.

Kevin R Gurney, Daniel L Mendoza, Yuyu Zhou, Marc L Fischer, Chris C Miller, Sarath Geethakumar, and Stephane de la Rue du Can. High Resolution Fossil Fuel Combustion CO 2 Emission Fluxes for the United States. *Environmental Science & Technology*, 43(14):5535–5541, July 2009.

John Houghton. Global warming, 2005.

Wontae Hwang, John Dec, and Magnus Sjöberg. Spectroscopic and chemical-kinetic analysis of the phases of HCCI autoignition and combustion for single-and two-stage ignition fuels. *Combustion and Flame*, 154(3):387–409, August 2008.

IEA. CO2 Emissions from Fuel Combustion. Technical report, 2013.

IEA. World Energy Outlook. Technical report, 2013.

S. Jerzembeck and N. Peters. Laminar burning velocities at high pressure for primary reference fuels and gasoline: Experimental and numerical investigation. *Combustion and Flame*, 156(2):292–301, February 2009.

Robert J Kee, Fran M Rupley, Ellen Meeks, and James A Miller. CHEMKIN-III: A FORTRAN CHEMICAL KINETICS PACKAGE FOR THE ANALYSIS OF GAS-PHASE CHEMICAL AND PLASMA KINETICS. Technical report, Sandia National Laboratories, May 1996.

S L Kokjohn, R M Hanson, D A Splitter, and R D Reitz. Fuel reactivity controlled compression ignition (RCCI): a pathway to controlled high-efficiency clean combustion. *International Journal of Engine Research*, 12(3):209–226, 2011.

S. H. Lam and D. A. Goussis. The CSP method for simplifying kinetics. *International Journal of Chemical Kinetics*, 26(4):461–486, April 1994.

Chung K. Law. *Combustion Physics*. 2006.

Tianfeng Lu and Chung K. Law. A directed relation graph method for mechanism reduction. *Proceedings of the Combustion Institute*, 30(1):1333–1341, January 2005.

Xingcai Lu, Dong Han, and Zhen Huang. Fuel design and management for the control of advanced compression-ignition combustion modes. *Progress in Energy and Combustion Science*, 37(6):741–783, December 2011.

Junjun Ma, Xingcai Lü, Libin Ji, and Zhen Huang. Evaluation of SCCI potentials in comparison to HCCI and conventional DICI combustion using n-heptane. *Energy & Fuels*, 22(2):954–960, 2008.

N. M Marinov. A Detailed Chemical Kinetic Model for High Temperature Ethanol Oxidation. *International Journal of Chemical Kinetics*, (31):183–220, 1999.

Matthew J McNenly, Russell A Whitesides, and Daniel L Flowers. Adaptive Preconditioning Strategies for Integrating Large Kinetic Mechanisms. *8th US Nat Combust Meet*, (070RK-377), 2013.

M. Mehl, H.J. Curran, W.J. Pitz, and C.K. Westbrook. Chemical kinetic modeling of component mixtures relevant to gasoline. In *European Combustion Meeting*, 2009.

M. Mehl, JY Chen, and WJ Pitz. An approach for formulating surrogates for gasoline with application toward a reduced surrogate mechanism for CFD engine modeling. *Energy & Fuels*, 25(11):5215–5223, 2011.

Marco Mehl, William J Pitz, Charles K Westbrook, and Henry J Curran. Kinetic modeling of gasoline surrogate components and mixtures under engine conditions. *Proceedings of the Combustion Institute*, 33(1):193–200, 2011.

M. O'Connaire, H.J. Curran, J. M. Simmie, W.J. Pitz, and C.K. Westbrook. A Comprehensive Modeling Study of Hydrogen Oxidation. *International Journal of Chemical Kinetics*, 36:603–622, 2004.

S. A. Orszag, V. Yakhot, W.S. Flannery, F. Boysan, D. Choudhury, J. Maruzewski, and B. Patel. Near-wall turbulent flows, 1993.

Mark A Patterson and Rolf D Reitz. Modeling the Effects of Fuel Spray Characteristics on Diesel Engine Combustion and Emission, 1998.

P Pepiotdesjardins and H Pitsch. An efficient error-propagation-based reduction method for large chemical kinetic mechanisms. *Combustion and Flame*, 154(1-2):67–81, July 2008.

Federico Perini, Emanuele Galligani, Giuseppe Cantore, and Rolf D Reitz. Validation of a Sparse Analytical Jacobian Chemistry Solver for Heavy-Duty Diesel Engine Simulations with Comprehensive Reaction Mechanisms. 2012.

R.T. Pollard. *Gas-Phase Combustion*, volume 17 of *Comprehensive Chemical Kinetics*. Elsevier, 1977.

Roberta Quadrelli and Sierra Peterson. The energyclimate challenge: Recent trends in CO2 emissions from fuel combustion. *Energy Policy*, 35(11):5938–5952, November 2007.

K.J. Richards, P.K. Senecal, and E. Pomraning. CONVERGE 2.1.0, 2013.

P. Rosin and E. Rammler. The Laws Governing the Fineness of Powdered Coal. *Journal of the Institute of Fuel*, 7:29–36, 1933.

S. Mani Sarathy, Stijn Vranckx, Kenji Yasunaga, Marco Mehl, Patrick Oß wald, Wayne K. Metcalfe, Charles K. Westbrook, William J. Pitz, Katharina Kohse-Höinghaus, Ravi X. Fernandes, and Henry J. Curran. A comprehensive chemical kinetic combustion model for the four butanol isomers. *Combustion and Flame*, 159(6):2028–2055, June 2012.

Samveg Saxena and Iván D. Bedoya. Fundamental phenomena affecting low temperature combustion and HCCI engines, high load limits and strategies for extending these limits. *Progress in Energy and Combustion Science*, 39(5):457–488, October 2013.

Magnus Sjöberg and JE Dec. Comparing late-cycle autoignition stability for single-and two-stage ignition fuels in HCCI engines. *Proceedings of the Combustion Institute*, 31 II(2):2895–2902, January 2007.

Magnus Sjöberg and JE Dec. EGR and Intake Boost for Managing HCCI Low-Temperature Heat Release over Wide Ranges of Engine Speed. (724):776–790, 2007.

YF Tham, F. Bisetti, and J.-Y. Chen. Development of a highly reduced mechanism for iso-octane HCCI combustion with targeted search algorithm. *Journal of Engineering for Gas Turbines and Power*, 130(4):042804, 2008.

Guohong Tian, Ritchie Daniel, Haiying Li, and Hongming Xu. Laminar burning velocities of 2, 5-dimethylfuran compared with ethanol and gasoline. *Energy & Fuels*, 24(7):3898–3905, July 2010.

Alison S. Tomlin, Genyuan Li, Herschel Rabitz, and Janos Toth. A general analysis of approximate nonlinear lumping in chemical kinetics. II. Constrained lumping. *The Journal of Chemical Physics*, 101(2):1188, July 1994.

David Vuilleumier, Darko Kozarac, Marco Mehl, Samveg Saxena, William J. Pitz, Robert W. Dibble, Jyh-Yuan Chen, and S. Mani Sarathy. Intermediate temperature heat release in an HCCI engine fueled by ethanol/n-heptane mixtures: An experimental and modeling study. *Combustion and Flame*, 161(3):680–695, March 2014.

Charles K. Westbrook and Frederick L. Dryer. Chemical kinetic modeling of hydrocarbon combustion. *Progress in Energy and Combustion Science*, 10(1):1–57, January 1984.

C.K. Westbrook, W.J. Pitz, and H.J. Curran. *HCCI and CAI Engines for the Automotive Industry*. Elsevier, 2007.

Charles K. Westbrook. Chemical kinetics of hydrocarbon ignition in practical combustion systems. *Proceedings of the Combustion Institute*, 28(2):1563–1577, January 2000.

Benjamin Wolk and Jyh-Yuan Chen. Computational Study of Partial Fuel Stratification for Hcci Engines Using Gasoline Surrogate Reduced Mechanism. *Combustion Science and Technology*, 186(3):332–354, 2014.

V. Yakhot, S. A. Orszag, S. Thangam, T. B. Gatski, and C. G. Speziale. Development of turbulence models for shear flows by a double expansion technique. *Physics of Fluids A: Fluid Dynamics*, 4(7):1510, 1992.

Yi Yang, JE Dec, Nicolas Dronniou, and Magnus Sjöberg. Tailoring HCCI heat-release rates with partial fuel stratification: Comparison of two-stage and single-stage-ignition fuels. *Proceedings of the Combustion Institute*, 33(2):3047–3055, January 2011.

Yi Yang, John Dec, Nicolas Dronniou, and William Cannella. Boosted HCCI combustion using low-octane gasoline with fully premixed and partially stratified charges. *SAE International Journal of Engines*, 5:1075–1088, April 2012.

F. Zhao, MC Lai, and DL Harrington. Automotive spark-ignited direct-injection gasoline engines. *Progress in Energy and Combustion Science*, 25(5):437–562, 1999.

Zhaolei Zheng and Mingfa Yao. Charge stratification to control HCCI: Experiments and CFD modeling with n-heptane as fuel. *Fuel*, 88(2):354–365, 2009.

Zhaolei Zheng, Mingfa Yao, and Weilong Wu. Numerical simulation on combustion and emission processes of premixed/direct-injected fuel stratification combustion. *International Journal of Green Energy*, 7(5):498–515, October 2010.